

EFFECT OF PORE GEOMETRY ON WATER  
AND SURFACTANT FLOODING BY PDMS  
MICROFLUIDIC MICROMODELS

by

Wei Xu



© Copyright by Wei Xu, 2012

All Rights Reserved



A thesis submitted to the Faculty and the Board of Trustees of the Colorado School of Mines in partial fulfillment of the requirements for the degree of Master of Science (Petroleum Engineering).

Golden, Colorado

Date \_\_\_\_\_

Signed: \_\_\_\_\_  
Wei Xu

Signed: \_\_\_\_\_  
Dr. Xiaolong Yin  
Thesis Advisor

Signed: \_\_\_\_\_  
Dr. Keith Neeves  
Thesis Advisor

Golden, Colorado

Date \_\_\_\_\_

Signed: \_\_\_\_\_  
Dr. Ramona Graves  
Professor and Head  
Department of Petroleum Engineering



## ABSTRACT

Core flooding and micromodels are two common laboratory methods to study improved and enhanced oil recovery (IOR/EOR) processes. Micromodel is a better option to visualize the microscopic displacement and flow within porous media. Using micro-fabrication technology, we developed Polydimethylsiloxane (PDMS) microfluidic porous media analogs. The porosity and permeability of these analogs are 19% and about 200md, respectively; they are close to the values in typical Berea sandstones.

Seven different types of analogs were made to study the effect of pore geometry: four with periodic square and hexagonal patterns and three with random patterns constructed from Voronoi diagram that were designed to mimic homogeneous and heterogeneous rock textures. Single-phase flow experiments were conducted to measure the permeability of seven analogs and results were compared with lattice-Boltzmann(LB) Simulations. The measured and simulated permeability are close to each other, and both are close to the design value.

Water flooding experiments were first conducted with hydrophobic walls to study the influence of geometry and coordinate number (CN). Brine (1.5 wt% NaCl) saturation was measured at water breakthrough and at interval of 0.5 pore volume (PV) injected. The recovery factor (RF) ranged from 74% to 90%. The geometry plays a significant role in the recovery factor. Then, surfactants (0.5 wt%, Shell NEODOL 91-8 nonionic Ethoxylated Alcohol) were added to study the influence of interfacial tension. When the interfacial tension was reduced from  $28.37\text{ dyne/cm}$  to  $3.57\text{ dyne/cm}$ , oil recovery was enhanced by 10–20%. In homogenous geometry, the surfactant works better than in the heterogeneous geometry.



## TABLE OF CONTENTS

ABSTRACT . . . . .	iii
LIST OF FIGURES . . . . .	vii
LIST OF TABLES . . . . .	xi
LIST OF SYMBOLS . . . . .	xii
LIST OF ABBREVIATIONS . . . . .	xiv
ACKNOWLEDGMENTS . . . . .	xvi
DEDICATION . . . . .	xvii
CHAPTER 1 INTRODUCTION . . . . .	1
1.1 Objective . . . . .	1
1.2 Literature Review . . . . .	2
1.2.1 Review of traditional core flooding . . . . .	2
1.2.2 Review of micromodel technology . . . . .	4
1.2.3 Mechanism of surfactant flooding . . . . .	8
1.2.4 Previous work (Wu et al., 2012) . . . . .	11
1.3 Methodology . . . . .	12
1.4 Thesis Content . . . . .	13
CHAPTER 2 EXPERIMENTAL PROCEDURE . . . . .	15
2.1 Design of porous media geometry . . . . .	15
2.2 Fabrication of PDMS Micromodel . . . . .	18
2.3 Wettability Control of Micromodel . . . . .	20



2.3.1	Contact angle measurement . . . . .	20
2.3.2	Effectiveness of silane coating . . . . .	23
2.3.3	Wettability characterized by laser-induced fluorescence under the confocal microscope . . . . .	25
2.4	Fluid Properties (Density, Viscosity and the IFT measurements) . . .	26
2.4.1	Properties of Ethoxylated Alcohol (EA) . . . . .	26
2.4.2	Viscosity measurements . . . . .	27
2.4.3	IFT measurement and optimal concentration of EA in brine . .	28
2.5	Experiment Setup and Control . . . . .	30
2.5.1	Single-phase flow (permeability measurement) . . . . .	31
2.5.2	Two-phase flow (water or surfactant flooding) . . . . .	31
2.6	Imaging Processing and Saturation Analysis . . . . .	32
CHAPTER 3 SINGLE-PHASE FLOW EXPERIMENTS AND PERMEABILITY . . . . .		37
3.1	Theoretical Calculation Based on Kozeny Equation . . . . .	37
3.2	Method and Equations . . . . .	38
3.3	Results and Comparison with LB Simulations . . . . .	39
3.4	Error Analysis . . . . .	40
CHAPTER 4 WATER FLOODING TESTS: OBSERVATIONS AND MEASUREMENTS . . . . .		43
4.1	Breakthrough Pattern and Breakthrough Time . . . . .	43
4.1.1	Water front movement and breakthrough pattern . . . . .	43
4.1.2	Breakthrough time, recovery factor and geometry effects . . . .	50
4.2	Oil Recovery after Breakthrough and Geometry Effects . . . . .	51



CHAPTER 5 SURFACTANT FLOODING TEST: OBSERVATIONS AND MEASUREMENTS . . . . .	53
5.1 Breakthrough Pattern, Breakthrough Time and Recovery Factor . . . . .	53
5.1.1 Observation of breakthrough pattern by surfactant flooding . . .	53
5.1.2 Breakthrough time and recovery factor in water and surfactant flooding . . . . .	56
5.2 Water Front Movement and Dynamics of Displacement . . . . .	59
5.3 Examination of Contact Angle for Potential Wettability Alteration . . .	67
5.4 Real Time Progression of Water and Surfactant Flooding . . . . .	68
5.5 Enhanced Oil Recovery of Surfactant Flooding at Each Stages . . . . .	71
5.6 Influence of Capillary Number . . . . .	71
CHAPTER 6 CONCLUSIONS AND RECOMMENDATION . . . . .	75
6.1 Technical Advancements . . . . .	75
6.2 Conclusion . . . . .	75
6.3 Limitations . . . . .	76
6.4 Future Works and Recommendation . . . . .	77
REFERENCES CITED . . . . .	79
APPENDIX - IMAGE-FIJI AND MATLAB SCRIPTS . . . . .	83
A.1 Image Processing . . . . .	83
A.2 Pixel Analysis . . . . .	84
A.3 Recovery Calculation . . . . .	84
CD-ROM . . . . .	Pocket



## LIST OF FIGURES

Figure 1.1 Etched epoxy resin with homogenous and heterogeneous patterns . . .	5
Figure 1.2 One-quarter five-spot glass micromodels with different coordination numbers (CN) and pore-throat ratios . . . . .	5
Figure 1.3 Etched silicon wafer with 1:1 Berea sandstone geometry . . . . .	6
Figure 1.4 (Left) Controlled grain algorithm (Right) Immiscible flooding in glass micromodel . . . . .	6
Figure 1.5 (Left) Pore and throat structure of ROC (Right) Network of the ROC . . . . .	7
Figure 1.6 Microscopic water flooding displacement schematic diagram . . . . .	9
Figure 1.7 Displacement of mineral oil (clean fluid) by Water (dark fluid) in 8 different scenarios . . . . .	11
Figure 2.1 Voronoi algorithm for geometry generation adapted from Wu et al. (2012) . . . . .	15
Figure 2.2 (Left) Probability of pore size distribution (Right) Schematic of vugs and posts within vugs . . . . .	16
Figure 2.3 20x microscopic image of inlet and outlet of $\mu$ PMA . . . . .	16
Figure 2.4 100x images of $\mu$ PMAs, the scale bar is 10 $\mu$ m. . . . .	17
Figure 2.5 Fabrication procedures of microfluidic micromodel . . . . .	18
Figure 2.6 Thickness of KMPR 1010 at different spinning speed . . . . .	18
Figure 2.7 Layout and microscopic pictures of silicon master . . . . .	19
Figure 2.8 Apparatus used to characterize wettability . . . . .	21
Figure 2.9 Contact angle measurement of glass at three different conditions . .	21
Figure 2.10 Contact angle measurement of PDMS at four different conditions . .	22



Figure 2.11 Non-uniform wettability before silane coating (200x Magnification) . . . . .	23
Figure 2.12 Uniform wettability after silane coating (200x Magnification) . . . . .	24
Figure 2.13 Cross-section view of a channel with fluorescent dye (Left) and a combined fluorescent and optical view of the channel (Right) under water-wet condition just after bonding . . . . .	25
Figure 2.14 Confocal microscope and laser-induced fluorescence show the distribution of fluids in a silane-treated channel . . . . .	26
Figure 2.15 Apparatus used to characterize fluids properties . . . . .	27
Figure 2.16 IFT between brine with different EA concentration and light mineral oil . . . . .	29
Figure 2.17 Schematic diagram of pressure-control system . . . . .	30
Figure 2.18 Image processing by Image-Fiji . . . . .	33
Figure 2.19 Flowchart of microscopic imaging processing in Image-Fiji . . . . .	34
Figure 2.20 Flowchart of pixel analysis in Image-Fiji . . . . .	35
Figure 2.21 Flowchart of recovery factor calculated in MATLAB . . . . .	36
Figure 3.1 Permeability by single-phase experiments, LB 3D simulations and the Kozeny equation . . . . .	39
Figure 3.2 Equipment errors and experimental errors . . . . .	41
Figure 3.3 Dimensionless equipment errors . . . . .	42
Figure 4.1 Breakthrough patterns of water flooding for Chip U, D and V . . .	45
Figure 4.2 Breakthrough patterns of water flooding for Chip S, SV, H and HV	46
Figure 4.3 The interfaces in nearby channels withdrew when water entered vugs . . . . .	47
Figure 4.4 Different water flooding patterns of Chip S at position 2 and position 6 . . . . .	48
Figure 4.5 (a) Breakthrough times of water flooding (b) Recovery factors at breakthrough . . . . .	50



Figure 4.6 (a) Breakthrough times of water flooding (b) Recovery factors at breakthrough . . . . .	51
Figure 4.7 (a) Breakthrough times of water flooding (b) Recovery factors at breakthrough . . . . .	52
Figure 5.1 Breakthrough patterns of surfactant flooding for Chip U, D and V . . . . .	54
Figure 5.2 Breakthrough patterns of surfactant flooding for Chip S, SV, H and HV . . . . .	55
Figure 5.3 (a) Breakthrough times of water flooding (b) Recovery factors at breakthrough . . . . .	57
Figure 5.4 Recovery factor versus breakthrough time of surfactant flooding . . . . .	58
Figure 5.5 Magnified (100x) movement of water fronts in Chip U at 10s interval in water flooding (Left) and surfactant flooding (Right) . . . . .	60
Figure 5.6 Magnified (100x) movement of water fronts in Chip D at 10s interval in water flooding (Left) and surfactant flooding (Right) . . . . .	61
Figure 5.7 Magnified (100x) movement of water fronts in Chip V at 10s interval in water flooding (Left) and surfactant flooding (Right) . . . . .	62
Figure 5.8 Magnified (100x) movement of water fronts in Chip S at 10s interval in water flooding (Left) and surfactant flooding (Right) . . . . .	63
Figure 5.9 Magnified (100x) movement of water fronts in Chip SV at 10s interval in water flooding (Left) and surfactant flooding (Right) . . . . .	64
Figure 5.10 Magnified (100x) movement of water fronts in Chip H at 10s interval in water flooding (Left) and surfactant flooding (Right) . . . . .	65
Figure 5.11 Magnified (100x) movement of water fronts in Chip SH at 10s interval in water flooding (Left) and surfactant flooding (Right) . . . . .	66
Figure 5.12 400x magnification image after water flooding and surfactant flooding . . . . .	68
Figure 5.13 Progression of water and surfactant flooding for each $\mu$ PMA . . . . .	69
Figure 5.14 Recovery factor of each $\mu$ PMA in water and surfactant flooding . . . . .	70



Figure 5.15 Recovery factor at breakthrough versus  $\log_{10}Ca$  of each  $\mu$ PMA in water and surfactant flooding . . . . . 72

Figure 5.16 Recovery factor at 3 PV injected versus  $\log_{10}Ca$  of each  $\mu$ PMA in water and surfactant flooding . . . . . 73



## LIST OF TABLES



## LIST OF SYMBOLS

Capillary number . . . . .	$Ca$
Viscosity . . . . .	$\mu$
Velocity of injecting fluid . . . . .	$u$
Interfacial tension . . . . .	$\sigma$
Water saturation . . . . .	$S_w$
Irreducible water saturation . . . . .	$S_{wi}$
Oil saturation . . . . .	$S_o$
Length of $\mu$ PMA . . . . .	$L$
Breakthrough time . . . . .	$t_{BT}$
Permeability . . . . .	$k$
Porosity . . . . .	$\phi$
Kozeny constant . . . . .	$c$
Specific surface . . . . .	$s$
Perimeter of channels within $\mu$ PMA . . . . .	$p_c$
Area of top or bottom of channels within $\mu$ PMA . . . . .	$A_c$
Width of $\mu$ PMA . . . . .	$w$
Height of $\mu$ PMA . . . . .	$h$
Flow rate . . . . .	$Q$
Cross-section area of $\mu$ PMA . . . . .	$A$
Pressure drop along $\mu$ PMA . . . . .	$\Delta P$



Diameter of measuring tube . . . . .	$D$
Interval of scales on measuring tube . . . . .	$dl$
Time interval for meniscus to pass the distance of $dl$ . . . . .	$dt$
Independent variables . . . . .	$x, y, z, \dots$
Standard deviation of independent variables . . . . .	$\delta x, \delta y, \delta z, \dots$
Standard deviation of viscosity . . . . .	$\delta \mu$
Standard deviation of diameter of measuring tube . . . . .	$\delta D$
Standard deviation of length of $\mu$ PMA . . . . .	$\delta L$
Standard deviation of measuring interval on the ruler . . . . .	$\delta dl$
Standard deviation of pressure drop . . . . .	$\delta \Delta P$
Standard deviation of Height of $\mu$ PMA . . . . .	$\delta h$
Standard deviation of width of $\mu$ PMA . . . . .	$\delta w$
Standard deviation of time interval . . . . .	$\delta dt$



## LIST OF ABBREVIATIONS

Breakthrough . . . . .	B.T.
Critical micelle concentration . . . . .	CMC
Coordination number . . . . .	CN
Computed microtomography . . . . .	CT
Enhance Oil Recovery . . . . .	EOR
Improved Oil Recovery . . . . .	IOR
Interfacial tension . . . . .	IFT
Lattice-Boltzmann . . . . .	LB
Lab-on-a-Chip . . . . .	LOC
Micro porous media analog . . . . .	$\mu$ PMA
Norland Adhesive 81 . . . . .	NOV81
Original Oil in Place . . . . .	OOIP
Polydimethylsiloxane . . . . .	PDMS
Poly(dimethylsiloxane-ethylene oxide polymeric) . . . . .	PEO-PDMS
Polyurethane Methacrylate . . . . .	PUMA
Pore volume . . . . .	PV
Recovery factor . . . . .	RF
Reservoir-on-a-Chip . . . . .	ROC
Scanning electron microscope . . . . .	SEM
Thermoset Polyester . . . . .	TPE



Uniform	.....	U
Pore Size Distribution	.....	D
Uniform Vugs	.....	V
Square	.....	S
Square Vugs	.....	SV
Square	.....	H
Square Vugs	.....	HV



## ACKNOWLEDGMENTS

I would never have been able to finish my dissertation without the guidance of my committee members, help from my colleagues and friends, and the support from my parents and girlfriend.

I would like to express my deepest gratitude to my advisor, Dr. Xiaolong Yin, for his patience, guidance and supporting on me, making me a better researcher. I would like to thank my co-adviser, Dr. Keith Neeves, who leads me to enter the world of microfluidic. I would also like to thank my committee members, Dr. Hossein Kazemi and Dr. Yu-Shu Wu, who teach me the knowledge of EOR and give me insightful advice on my research.

I would like to thank Mengjie Wu, the previous student, who has meticulously laid the foundation of this research. I would like to thank my colleagues Jeong Tae Ok and Feng Xiao. Without their skillful fabrication and simulations, this research can not be finished. And I would like to thank my colleagues in Dr. Keith Neeve's group, Abimbola Onasoga, Adam Wufsus, Joanna Sylman, Ryan Hansen and Steven Barton. Without their help I will never know how to use these chemicals and sophisticated microscopes. I would like to thank Baharak Alamdari and TIORCO Inc for the supporting the IFT measurement. Also I would like to thank Zach Aman, Hongfei Xu and Eric Webb for their supporting of fluid properties measurement. What's more, I would like to thank my friends Chang Liu and Ronglei Zhang for teaching me how to use LaTex.

I would like to thank my parents for their support and encouragement from the other side of the earth. Finally, I would like to thank my girlfriend, Sijia Wang. She was always there cheering me up and providing me with pipettes and stir bars.



For those that shall follow after.



# CHAPTER 1

## INTRODUCTION

This chapter introduces the overall objective of this research and methodology. Also, a literature review is provided here to cover the basics of core flooding, micro-model technology and the mechanism of surfactant flooding.

### 1.1 Objective

Core flooding and micromodels are two common laboratory methods to study improved oil recovery (IOR) and enhanced oil recovery (EOR) processes. Laboratory study is necessary before any IOR/EOR process can be scaled up and applied to pilot studies. The success of the pilots will decide whether or not the IOR/EOR strategy can be applied to the field. To visualize the microscopic displacement and flow inside porous media, micromodels are the better option because of their transparency.

Microfluidic studies the behavior, precise control and manipulation of fluids in a tiny scale. With the development of micro- and nano- fabrication, the concept of 'Lab-on-a-Chip' (LOC), which was derived from the field of microfluidic/nanofluidics and means that several laboratory functions are integrated on a tiny-scale chip, may hold great promise for the study of micro- and nano-scale flow and transport in porous media. Polydimethylsiloxane (PDMS) is a polymeric material which is widely used in microfluidic study. The objective of this research is to use PDMS-based micromodel to study the effect of geometry on water and surfactant flooding processes. Our micromodels are highly random and complex, and their porosity and permeability can be designed to match those of real porous media. Hence, they are named as micro porous media analogs ( $\mu$ PMA).

In this study, seven different designs were fabricated to study the effect of geometry (porous media texture). We first conducted single-phase flow experiments to verify if

the permeability of  $\mu$ PMAs is as designed; in two-phase oil experiments, we developed water- and surfactant-flooding test systems for our PDMS-based micromodels. The effects of pore geometry and reduction in the interfacial tension (increase in the capillary number) due to surfactant were studied.

## 1.2 Literature Review

In this section, a brief literature review is provided to cover the basics of core flooding, micromodel technology and the mechanism of surfactant flooding.

### 1.2.1 Review of traditional core flooding

Core flooding is a laboratory test in which fluid is injected into cores to displace oil. The purpose is to measure the absolute and relative permeability of the rock, the interactions between rocks and fluids and the recovery factor of different flooding methods.

Normally, the core is taken from the reservoir of interests. A core holder holds the core to maintain the reservoir temperature and overburden pressure. It is a good choice to study a particular reservoir by using cores from the same formation. However, the cores are not always available, and they are usually expensive to obtain and preserve. In this situation, artificial cores are good candidates for core flooding test.

In core flooding test, the fluids are injected from one side of the core. The flow rates at both sides of the cores are measured. Normally, the saturation change and the recovery factor are calculated by the volume of the displaced fluids compared to the pore volume (PV). Bruining et al. (1998) had developed a new method for saturation measurement by using frequency domain reflectometry technology. Via this method the saturation distribution can be obtained fast and less expensive.

It is often desired to visualize the evolutions of oil saturations in core flooding experiments. Nuclear magnetic resonance (NMR) technology can be used to obtain

saturation profile. It is a useful tool in saturation analysis in laboratory core flooding test. By NMR technique, Enwere (1992) indicates that saturation profile is influenced by both viscous forces and capillary forces. Computed microtomography (CT) is another technology used to characterize the saturation distribution. Recently, Bataweel et al. (2011) studied the displacement front of different EOR method by using CT scan. These are, of course, selected examples of the many references that are available in these areas.

Water flooding is the most widely used improved oil recovery (IOR) method. IOR is a method of recovering oil by water or gas injection after the depletion of natural energy (expansion of fluids, gravity). Many water flooding researches were done using laboratory core flooding. For example, Mungan (1964) studied how wettability and interfacial tension influence water flooding by core flooding test. Farle and Redline evaluated the effect of water quality in West Montalvo Field by water flooding test in reservoir cores (Farle and Redline, 1968). Instead of using 1-D linear cores, Stalker and Graham (2008) developed a dual radial wedge core to study near wellbore flow. Rivet et al. (2010) had study the low salinity brine displacing oil by epoxy encased core flooding test. These studies show that core flooding is a reliable tool to assess the performance of IOR processes and strategies before the anticipated field application.

Core flooding is widely used not only in IOR, but also EOR researches. EOR works by changing the properties of reservoir fluids after primary recovery and IOR processes. There are three methods of EOR, namely chemical flooding, miscible flooding and thermal recovery. Core flooding is commonly used to test chemical and miscible flooding. Among others, Asar et al. (1987) did a miscible flooding study with Arabian carbonate cores. Levitt et al. (2006) used Berea sandstone cores and dolomite cores to test the performance of EOR surfactants in different reservoir lithology. Austad (1993) used core flooding tests to study the retention mechanisms of Ethoxylated sulfonates. Alamdari et al. (2012) conducted many surfactant flooding

tests in fractured carbonate cores. The cores were held in a centrifuge in order to scale up the core to reservoir condition by generating a high gravity head to assist drainage from oil wet rocks.

Traditional core flooding is a reliable method to study the optimum design for water flooding and enhanced oil recovery. With real rock and approximated reservoir condition, the flooding process can be well simulated. However, the core flooding test has its deficiencies. As mentioned before, the cost of core flooding is quite high, and the flooding process is quite time-consuming. Typically, a core flooding test need several days because of the small flowrate in cores. Whats more, even though some new technologies have been applied to characterize the flow in core flooding, direct visualization is still difficult due to lack of transparency.

### 1.2.2 Review of micromodel technology

In order to visualize displacement processes, capillary tube and micromodel have been introduced. Micromodels are very useful in visualizing the flow and transport phenomena at pore level.

Traditional micromodels use glass or epoxy resin porous media (Peden and Husain, 1985), made from chemical etching which cannot be precisely controlled, followed by bonding with a transparent cover. Flowrate is kept at a user-defined value. Cameras are used to record the images or to film the displacement process. The pores are three-dimensional, but the micromodel span is in two-dimensions with many designed patterns.

At early times, etched patterns are usually uniform. Peden and Husain (1985) showed some homogenous and heterogeneous epoxy resin etched micromodel. Lenormand and Zarcone (1985) developed a glass micromodel fabrication method using photochemical etching and transparent resin molding. In their micromodel, the pore size had a distribution from 0.1 to 0.6 mm. Many microscopic phenomena have been studied, for example, invasion percolation (Lenormand, 1990) and diffusion limited

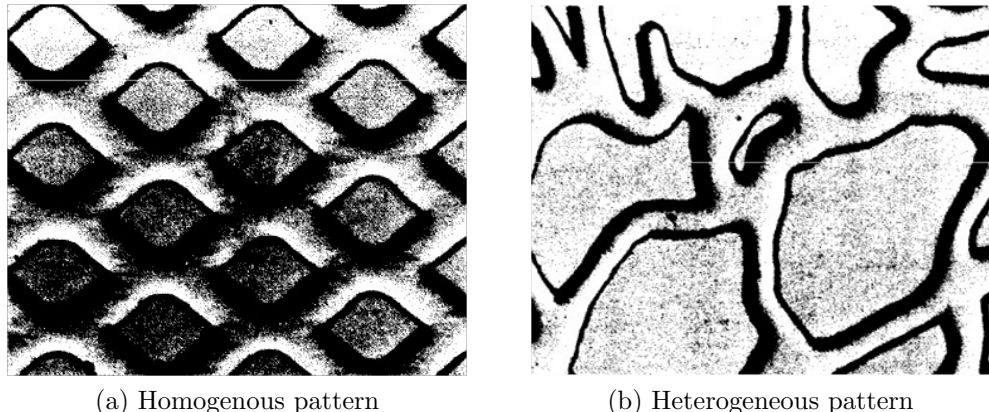


Figure 1.1: Etched epoxy resin with homogenous and heterogeneous patterns (Peden and Husain, 1985).

aggregation (Lenormand and Zarcone, 1985). Also the relationship between flow pattern and viscosity ratio or capillary number was shown in their studies.

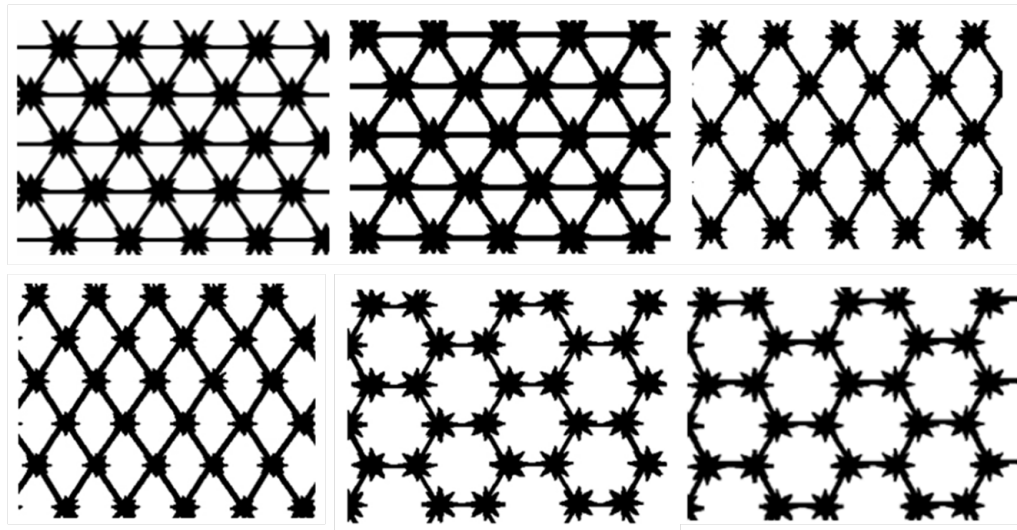


Figure 1.2: One-quarter five-spot glass micromodels with different coordination numbers (CN) and pore-throat ratios (Dehghan and Kharrat, 2009)

Dehghan and Kharrat (2009) studied the pore geometry issue and the influences of wettability and co-solvent by one-quarter five spot glass micromodels . The pore structures were designed periodically to have CN of 3, 4 and 6 and pore-throat ratio of 4 and 6. The pore-throat ratio is the parameter to show the ratio of large pore between rock grains to the small channel connecting pores. The results showed that

higher CN or higher pore-throat ratio lead to higher recovery.

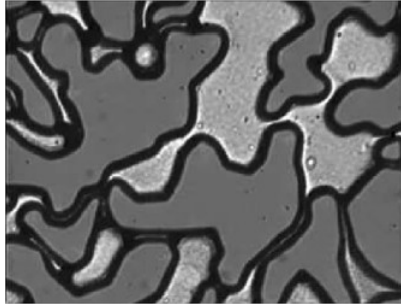


Figure 1.3: Etched silicon wafer with 1:1 Berea sandstone geometry (Kovscek et al., 2007)

Real rock geometries are more commonly used in recent micromodel studies. Scanning electron microscope (SEM) technology is used to obtain microscopic images of rocks porous geometry and then the image is casted onto micromodels. For example, Kovscek et al. (2007) etched a 1:1 Berea sandstone geometry on a silicon wafer to make a sandstone replica micromodel, which is shown in Figure 1.3. The depth of the flowing channel is  $25 \mu\text{m}$  and the width has a large distribution ranged of 10 to  $100 \mu\text{m}$ .

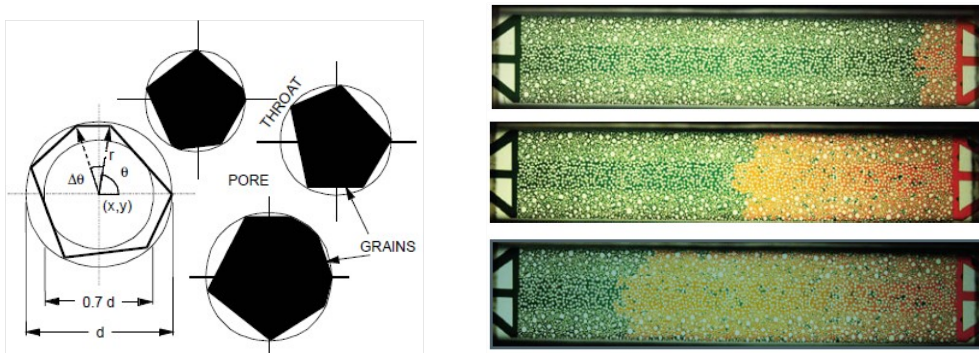


Figure 1.4: (Left) Controlled grain algorithm (Right) Immiscible flooding in glass micromodel (Sayegh and Fisher, 2008)

Besides, some three phase experiments had been done in micromodels. Because of the transparency of micromodels, the motion of gas bubbles and their breakup and coalescence can be observed clearly. Hawes et al. (1997) studied solution gas releasing

in residual oil after water flooding using micromodel technology. Oren (1992) use a regular square pattern micromodel to study the double-drainage mechanism when gas is injected after water flooding. (George et al., 2005) studied the solution-gas-drive mechanism by using silicon micromodel with a sandstone pattern.

Enhanced oil recovery studies, including miscible, immiscible and chemical flooding, have also been carried out on micromodels. Observation made through micromodel experiments is very useful to understand the complex flow phenomena in enhanced oil recovery processes. Some studies have been done on  $\text{CO}_2$  flooding (Sayegh and Fisher, 2008) and  $\text{CO}_2$ -enriched water injection (Riazi and Sohrabi, 2009) in glass micromodels. For chemical flooding, polymer flooding study has been done in Berea sandstone replica micromodel (Buchgraber et al., 2011). Several polymer solutions with different concentrations were tested in  $5\text{cm} \times 5\text{cm}$  silicon-etched micromodel. The polymer concentration was optimized to retard the viscous fingers and improve sweep efficiency. Also, different surfactants were tested on micromodels (Alshehri et al., 2009; Mohan, 2009; Wu et al., 2008) to study the effects of reduced interfacial tension (IFT).

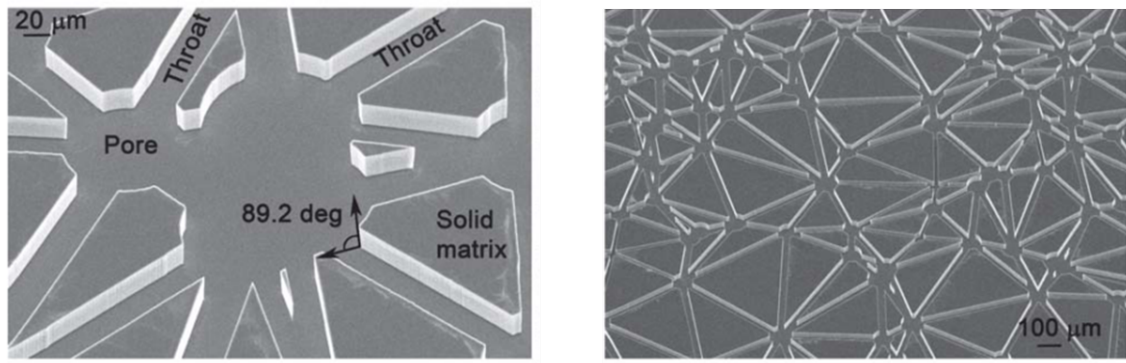


Figure 1.5: (Left) Pore and throat structure of ROC (Right) Network of the ROC (Gunda et al., 2011)

Compared with traditional micromodel where not much etching control is available, recent micromodels have used more controlled etching based on micro/nano fabrication (Gunda et al., 2011; Kovscek et al., 2007). Gunda et al. (2011) proposed

the term of Reservoir-on-a-Chip (ROC) based on the concept of LOC. The structure is shown in the Figure 1.5. This microfluidic micromodel was etched in a silicon substrate with a 2D network from a cross-section of 3D rock reconstruction. And water flooding test was done on this ROC system.

In addition, some polymer micromodels have been invented and are widely used in biochemical and biomedicine applications. In some recent studies (Javadpour and Fisher, 2008; Wu et al., 2012), Polydimethylsiloxane (PDMS) micromodels were used to study microscopic phenomena that are relevant to oil and gas industry applications.

Compared with glass and silicon micromodels, PDMS micromodels, fabricated by rapid prototyping, are easy to mold and cast and the cost are much lower (Javadpour and Fisher, 2008). Though PDMS has certain deficiencies, e.g. deformability, gas permeability, and incompatibility with certain organic solvents, there is a good opportunity that use of other transparent polymeric materials (Sollier et al., 2011) can overcome these deficiencies and lead to low-cost, disposable chips that may be used to rapidly screen IOR/EOR methods or find representative pore structures that can best simulate a give porous medium..

### 1.2.3 Mechanism of surfactant flooding

In water flooding processes, the displacement is called *drainage* in oil-wet formations, and *imbibition* in water-wet formations. From the Figure 1.6(a), in water-wet formation, the water is imbibed on the rock surface, and the residual oil is trapped in the center of large pore.

Some research shows that the carbonate formations are slightly oil-wet (Mohan, 2009; Wu et al., 2008). It is believed by some researcher (Agbalaka et al., 2008; Anderson, 1987) that the efficiency of water flooding is higher in a water-wet reservoir than one in an oil-wet reservoir. In oil-wet formations, water forms flow channels in the large pores, and oil in the small pore and on the rock surface is left behind . From Figure 1.6, Raza et al. (1968) illustrated the mechanism of water flooding in

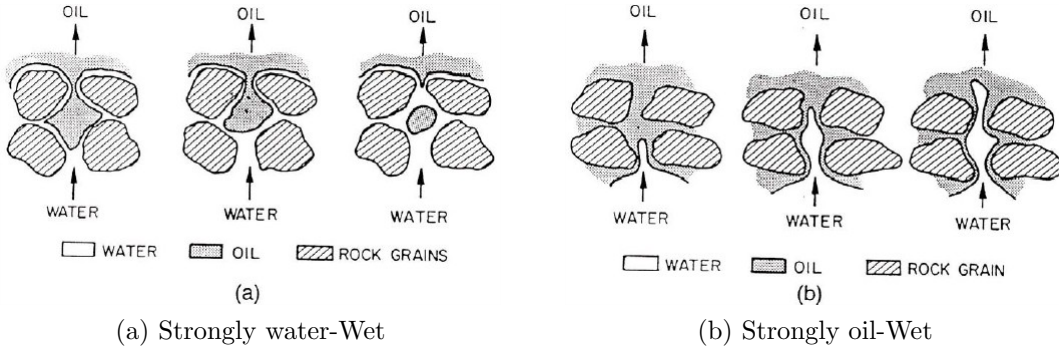


Figure 1.6: Microscopic water flooding displacement schematic diagram (Raza et al., 1968)

water-wet and oil-wet rocks. Owens and Archer (1971) did core flooding test in cores with different wettability which is achieved by a chemical solution named barium dinonyl naphthalene sulfonate , and found that water-wet formation has better water flooding performance than oil wet. Also, Dehghan and Kharrat (2009) had studied the effects of wettability on the recovery factor by micromodels. The results indicate that the reservoirs with water-wet or mixed wettability are easier to achieve higher oil recovery.

Because of capillary trapping, immiscible flooding can never achieve complete displacement and recovery. There is always residual oil saturation. The capillary number  $Ca$ , a dimensionless number which describes the ratio of viscous force to capillary force, influences the residual oil saturation and irreducible water saturation. It is defined as:

$$Ca = \frac{u\mu}{\sigma} \quad (1.1)$$

where:  $\mu$  is the viscosity of injecting fluid;  $\sigma$  is IFT between injecting and displaced fluids.

Increasing capillary number above the critical capillary number can reduce the residual oil saturation (Lake, 1989). There are three ways to increase the capillary number: increase the viscosity of water, increase the injection rate and lower the IFT

between water and oil. The most effective way is to lower the IFT between water or oil by surfactant flooding.

Typically, the capillary number in water flooding is from  $10^{-7}$  to  $10^{-5}$  (Lake, 1989). When capillary number is low, the capillary forces play an important role, leading to quick breakthrough and high residual oil saturation. There is a critical capillary number that the residual oil saturation remains the same when the capillary number is below this critical value. When the capillary number is higher than the critical capillary number, the influence of capillary force is low and the displacement front is more stable and the residual oil saturation begins to decrease. The critical capillary number of water-wet formation is about  $10^{-4}$  and of oil-wet reservoir is about  $10^{-3}$  (Lake, 1989).

Besides lowering the IFT, another mechanism of surfactant flooding to enhance oil recovery is the alteration of rock wettability (Schramm, 2000). Some surfactants are adsorbed onto the surface of the rock, changing the contact angle and making it more water-wet. This mechanism can play an important role in mixed-wetting and oil-wetting reservoir. However, this mechanism is usually very slow to take place.

The definition of surfactant flooding is to inject a surface-active agent to improve oil recovery. So alkaline flooding is not in this classification because it generates surfactant in situ. Surfactant flooding is also known as micellar-polymer flooding (MP flooding), because the surfactant in water is predominantly in the micelle form (Lake, 1989). Micelle is an aggregation of surfactant monomers. The forming of micelles can further lead to emulsification where the oil droplets are entrapped in the cores of micelles, reducing the fraction of the immobile oleic phase from the rocks.

The process of surfactant flooding in the oilfield begins with a 0–100% pore volume (PV) preflush to make the approaching surfactant more effective by changing the reservoir brine to optimal salinity. Then it is followed by a 5–20% PV MP slug with primary surfactant to drive more oil out. Behind the MP slug, a 0–100% PV mobility

buffer with polymer solution drives the MP slug to achieve good sweep efficiency. Chase water is further behind to push the mobility buffer. Between the mobility buffer and chase water, there is a taper to gradually decrease the concentration of polymer. However, in this research, this field procedure of surfactant flooding is not followed. In this experiment we use surfactant as a means to change the IFT and the capillary number to study the influence on the microscopic displacement efficiency.

When designing surfactant flooding, many issues should be carefully considered, for example, critical micelle concentration (CMC), optimal salinity and reservoir condition. A good surfactant flooding design should use highly active surfactant in sufficient quantities, and achieve large area swept and incremental oil recovery. The economics of used chemicals must be considered, too.

#### 1.2.4 Previous work (Wu et al., 2012)

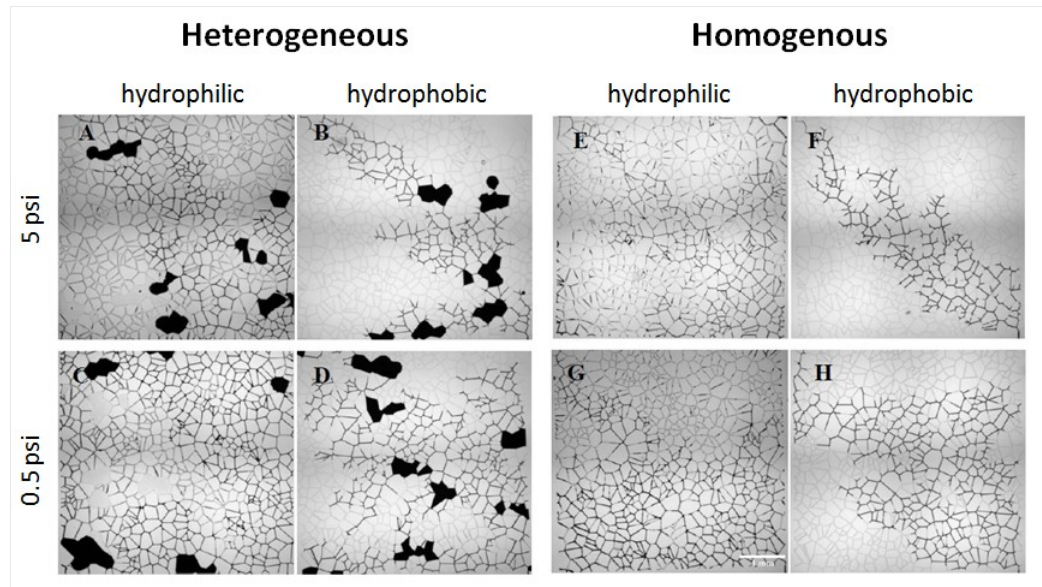


Figure 1.7: Displacement of mineral oil (clean fluid) by Water (dark fluid) in 8 different scenarios (Wu et al., 2012)

Wu et al. (2012) conducted several two-phase displacement experiments on  $5mm \times 5mm$  corner-to-corner PDMS-based micromodels. The flow was driven by a constant pressure. From Figure 1.7, in Wu's research, 8 different scenarios are studied, includ-

ing heterogeneous versus homogenous pattern, hydrophilic versus hydrophobic wall and high pressure head versus low pressure head.

The breakthrough time, saturation at breakthrough and final saturation were measured. The final saturation was measured when there was no further change in the saturation 20 minutes after the last observed change. In Wu's experiment, the water viscosity is 1.73 cP and mineral oil is 183 cP. The viscosity ratio is 107. At high pressure, less breakthrough time, less branches in saturation pattern and lower oil recovery were found. Also, the wettability of the wall is crucial. In the hydrophobic cases, the capillary force adds some resistance to the displacement process, while it assists the displacement in the hydrophilic cases. Thus the number of branches increases in the hydrophilic cases. Between homogenous and heterogeneous patterns, there is less difference on breakthrough saturation.

### 1.3 Methodology

In this study, as the objective is to study the effect of pore geometry and Capillary number on the efficiency of water-oil drainage process where water is the non-wetting phase, PDMS micromodels with seven different textures were fabricated and tested. The geometries were designed to have the same porosity (19%) and similar permeability (about 200 mD). The patterns were first transferred to silicon masters. PDMS micromodels were then molded on the masters and then bonded with glass substrates. Silane was coated to the side of the channels by vaporization in order to create uniform wettability between the PDMS and the glass substrate.

For each  $\mu$ PMA, permeability was measured from single-phase flow experiments where flow rates were altered by the application of different pressure drops. Darcy's law was then applied to find the permeability. The results were compared with the Kozeny Equation and lattice-Boltzmann Simulations.

Water flooding and surfactant flooding tests were conducted using a constant-pressure drive system and were repeated for at least three times for averaging. Mi-

croscopic images were taken at intervals of 0.5 pore volume injected and also at the breakthrough time by an Olympus inversion microscope. Image processing software, ImageJ-Fiji, were used to process and analyze the microscopic images to obtain the water saturation and the recovery factor.

The methodology will be elaborated again in Chapter 2 Experimental Procedure, and the results will be presented in Chapters 3–5.

#### 1.4 Thesis Content

Chapter 1 states the objective and methodology of this research. A review on the basics of core flooding, micromodel technology and surfactant flooding is also included. Chapter 2 presents the fabrication procedures, including the design of  $\mu$ PMA, the molding process, wettability control and fluids characterization. Also, the procedure of single- and two-phase flow experiment and image processing are covered. Chapter 3 compares the permeability obtained from single-phase flow experiment to those from LB simulations and the Kozeny Equation. Also, the procedure to estimate the error of measured permeability is presented. Chapter 4 shows the images and results of water flooding in each  $\mu$ PMA. The influences of geometry on breakthrough time, flow pattern and recovery factor are discussed. Chapter 5 shows the images and results of surfactant flooding in each  $\mu$ PMA. The displacement patterns are compared to those of water flooding. The influences of surfactant and the capillary numbers on the breakthrough time, flow pattern and recovery factor are discussed. Chapter 6 concludes the thesis and gives recommendations for futures work.



## CHAPTER 2

### EXPERIMENTAL PROCEDURE

#### 2.1 Design of porous media geometry

In this study, 3 random and 4 periodic geometries are designed. Random porous media geometry is generated using an algorithm based on Voronoi diagram (Wu et al., 2012). The process is shown in Figure 2.1:

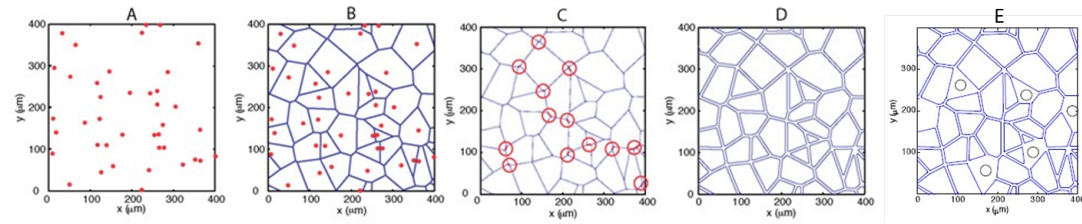


Figure 2.1: Voronoi algorithm for geometry generation adapted from Wu et al. (2012). Steps: A: Several Poisson points are generated in the target area. B: Around each Poisson point, a polygon is created with its vertices connected to three other vertices. C: Sides shorter than a predetermined threshold value are removed D: The edges are displaced to yield a network of channels with a finite width. E: Randomly selected grains are removed to created heterogeneity

The dimension of each  $\mu$ PMA is  $30\text{mm} \times 3\text{mm} \times 15\mu\text{m}$ . All these  $\mu$ PMA are designed to have similar porosity of 19% and permeability about 200 mD. From Figure 2.3, inlet and outlet holes are punched with 0.75 mm radius. The punched holes are connected with  $\mu$ PMA via micro-channels that are  $30\ \mu\text{m}$  wide and 1.5 mm long.

Compared to the algorithm used in the previous work(Wu et al., 2012), the updated algorithm used in this study allows one to specify a channel size distribution to study the effect of pore size distribution on oil trapping. Instead of using a fixed width, a distribution of channel widths between 4 and  $8\ \mu\text{m}$  with a  $0.5\ \mu\text{m}$  incremental

change is generated in Step D. The distribution is a Gaussian which is shown in the Figure 2.2(a). In addition, when selected grains are removed, a post is automatically left behind, providing a structural support to the large pores (vugs) so that they do not stick to the glass substrate and remain open. This is needed because the depth of the channels in this study ( $14\text{--}15 \mu\text{m}$ ) is much smaller than that in the previous study ( $60 \mu\text{m}$ ).

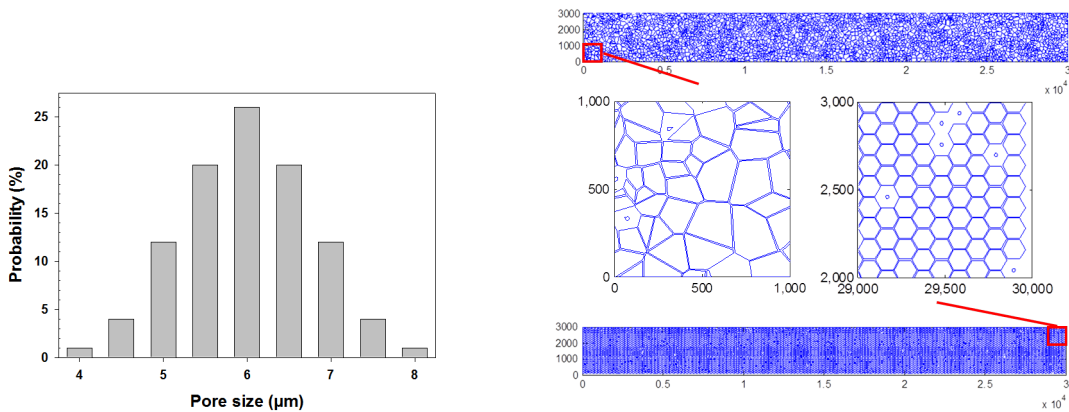


Figure 2.2: (Left) Probability of pore size distribution (Right) Schematic of vugs and posts within vugs

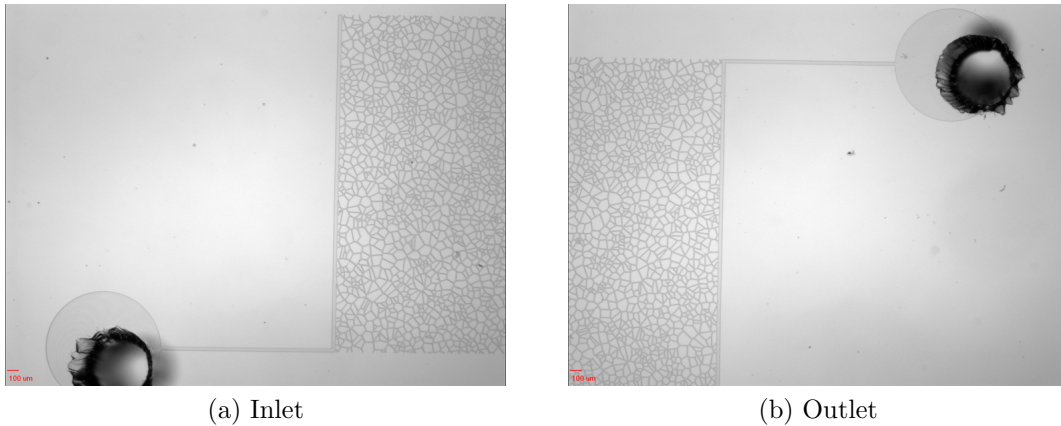


Figure 2.3: 20x microscopic image of inlet and outlet of  $\mu\text{PMA}$

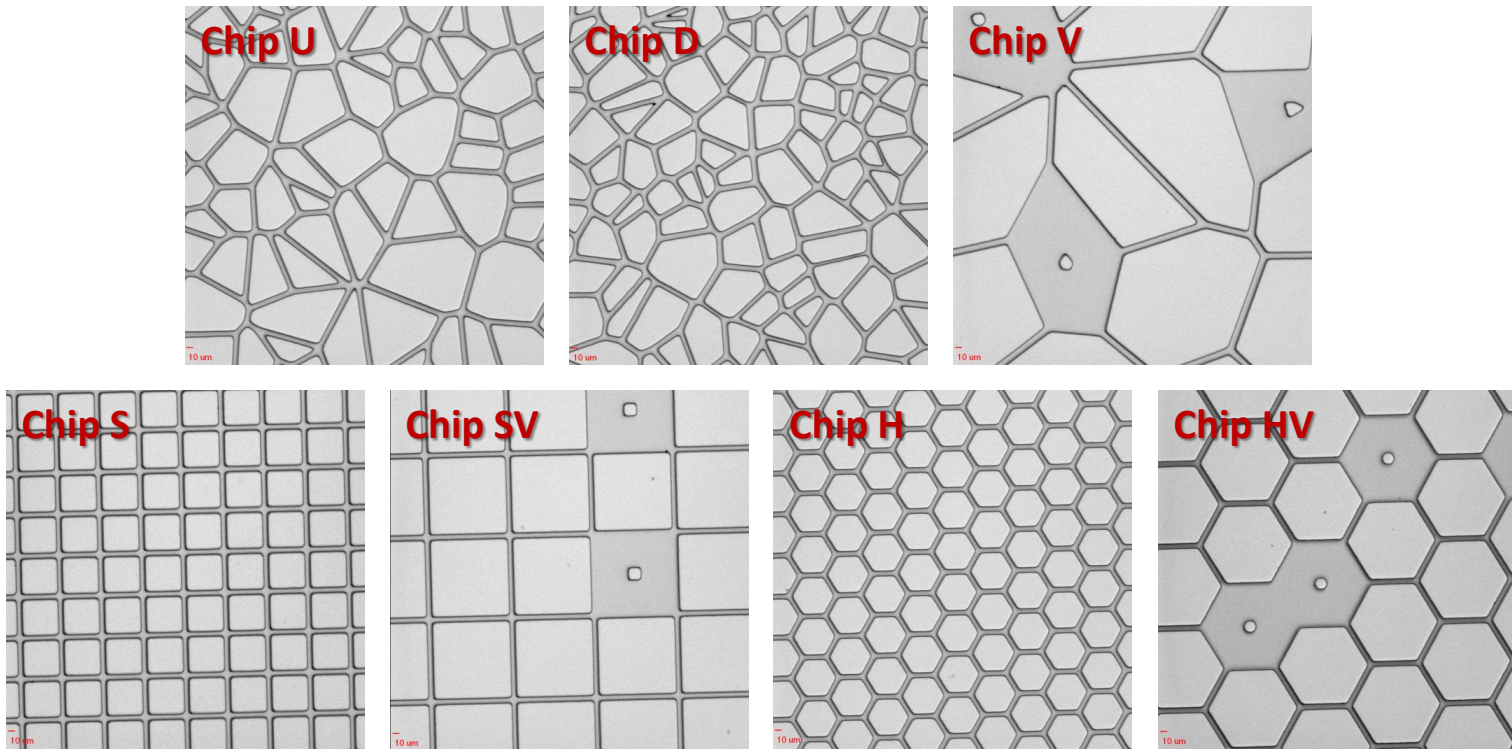


Figure 2.4: 100x images of  $\mu$ PMAs, the scale bar is 10  $\mu$ m. Chip U: Random pore geometry with 6  $\mu$ m channel; Chip D: Random pore geometry with 4–8  $\mu$ m channel size distribution; Chip V: Random pore geometry with 8  $\mu$ m channel and vugs; Chip S: Periodic square geometry with 6  $\mu$ m channel; Chip SV: Periodic square geometry with 6  $\mu$ m channel and vugs; Chip H: Periodic hexagon geometry with 6  $\mu$ m Channel; Chip HV: Periodic hexagon geometry with 6  $\mu$ m channel and vugs

## 2.2 Fabrication of PDMS Micromodel

The molding and bonding steps are already described by several researchers (McDonald et al., 2000; Wu et al., 2012). In this study, our procedures are based on Wu's work (2012).

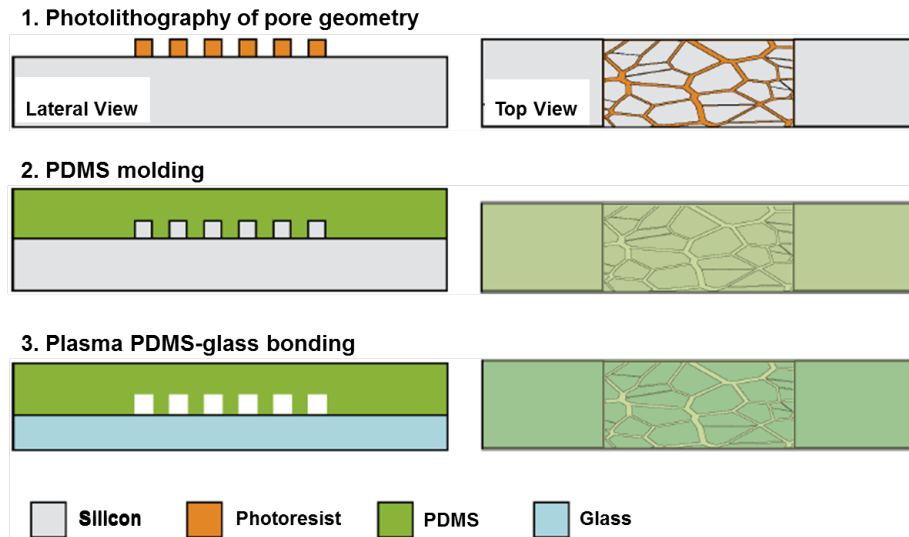


Figure 2.5: Fabrication procedures of microfluidic micromodel(Wu et al., 2012)

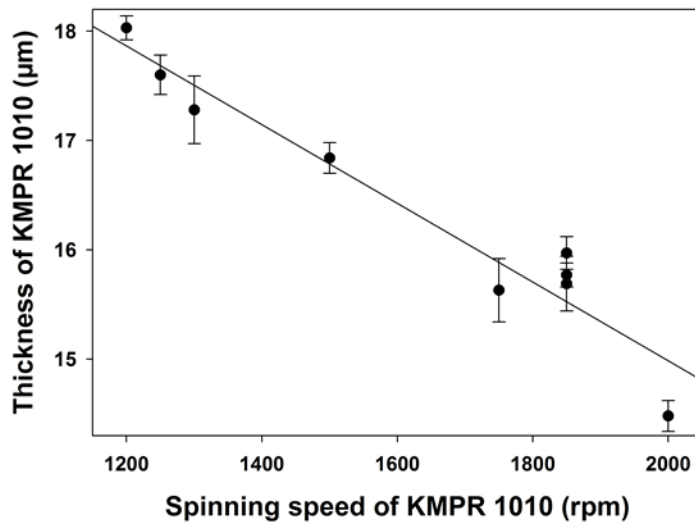


Figure 2.6: Thickness of KMPR 1010 at different spinning speed

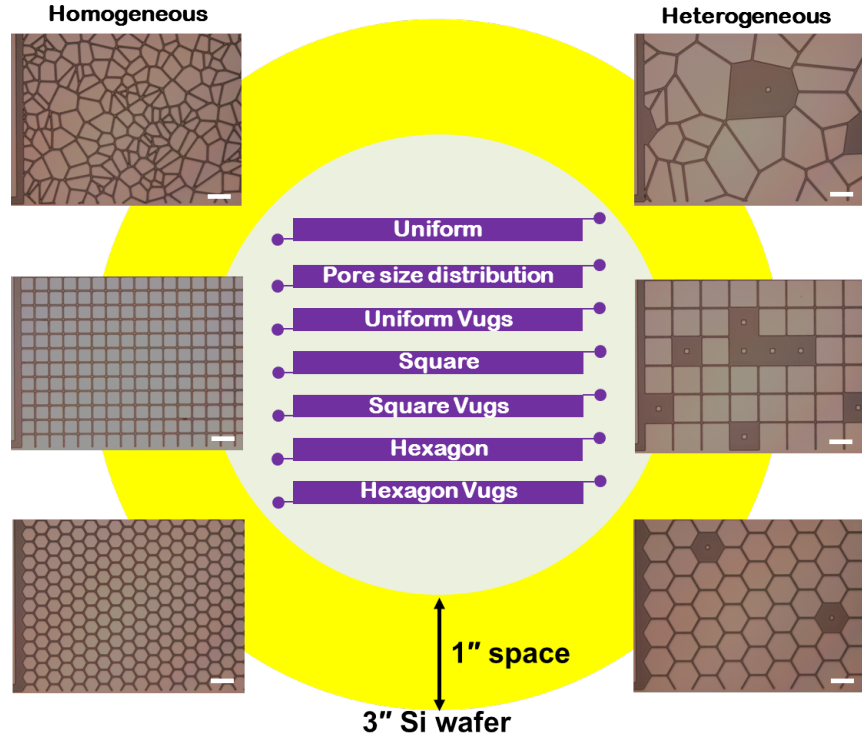


Figure 2.7: Layout and microscopic pictures of silicon master

The fabrication procedures are shown in Figure 2.5. The geometries of  $\mu$ PMA described in the last section were transferred onto a photomask, and then onto a silicon wafer by photolithography. A negative tone photoresist (KMPR 1010, KAYAKU Microchem) was used for PDMS mold with a depth of about  $15\ \mu\text{m}$ . It is very important to accurately control the thickness of photoresist, because the thickness plays a significant role in the properties of our  $\mu$ PMA. Based on preliminary experiments results shown in ??, the relationship between the mold thicknesses and spinning speed is found. In this study, we used about 1900 rpm spinning speed to obtain  $15\ \mu\text{m}$  thick devices. In the figure (b), the lay out and a photo of silicon master with KMPR is shown.

The silicon master was treated by silane to keep the master hydrophobic. Then 50g PDMS with a 10:1 ratio of base agent to curing agent was molded on the silicon master, as shown in Figure 2.5 Step 2, followed by drying 3 hours in oven for at least

3 hours. Then the PDMS chips were cut and inlet and outlet holes were punched. Afterwards, in order to remove the dust on PDMS, the PDMS chips were first sonicated in 1M HCl for 8 minutes, and then in acetone and ethanol for 5 minutes, respectively. Meanwhile, the glass substrate was cleaned in 1:1 ration of 1M HCl to 1M methanol for 1 hour.

After drying for 1 hour, both the PDMS chip and the cover slide were treated by oxygen plasma for 30 sec and then bonded together. The depth of the channel is only  $15\ \mu\text{m}$ , so care must be taken when bonding. PDMS was slightly pushed onto the glass substrate by a roller. After bonding, the micromodel was put in 80 degree oven for at least one hour to strengthen the bonding.

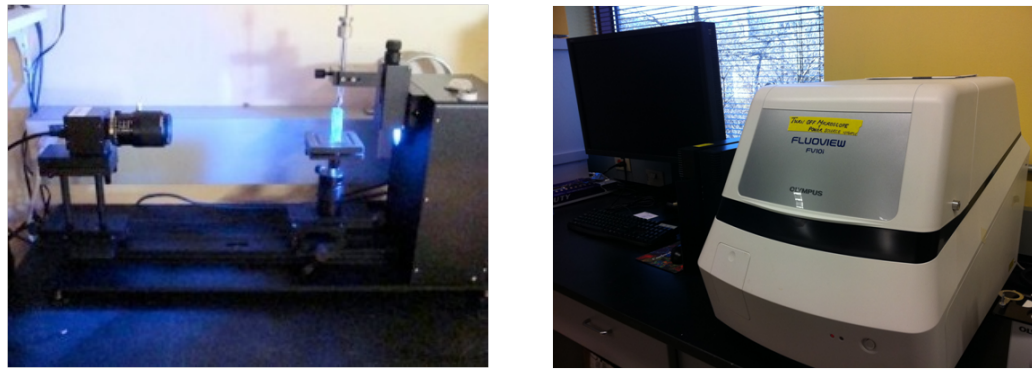
### 2.3 Wettability Control of Micromodel

An advantage of PDMS is that the wettability can be easily controlled. Wu et al. (2012) mentioned that the plain PDMS is hydrophobic, and it becomes hydrophilic after treated by oxygen plasma. The hydrophilic state, however, is not stable. Yao and Fang (2012) presented a method to make an stable hydrophilic poly(dimethylsiloxane-ethylene oxide polymeric) (PEO-PDMS) by adding surfactant.

In this section, the wettability of our microfluidic micromodel is presented. Contact angles of water-air system on PMDS and glass substrates were measured after the substrates were treated with plasma or silane. Inverted and confocal microscopes were used to examine the wettability of water-oil system inside the  $\mu\text{PMA}$ .

#### 2.3.1 Contact angle measurement

The wettability of PDMS and glass substrates were studied by contact angle measurement. Initially, the PDMS is hydrophobic and glass is hydrophilic. Both PDMS and glass become strongly hydrophilic after oxygen plasma bonding. After about 24 hours, the PDMS returns to intermediate wetting condition. However, the glass substrate is still hydrophilic. As a result, the wettability condition of PDMS-glass



(a) CAM 200

(b) FV10i confocal microscope

Figure 2.8: Apparatus used to characterize wettability

$\mu$ PMA is not uniform.

To solve this problem, Trichlorosilane (Tridecafluoro-1, 1, 2, 2-Tetrahydrooctyl-Trichlorosilane, Gelest) was used to treat glass in the same way as to treat the silicon wafer. To verify the wettability, contact angles of PDMS and glass were measured under three conditions: no treatment, oxygen plasma treatment, and silane treatment after oxygen plasma.

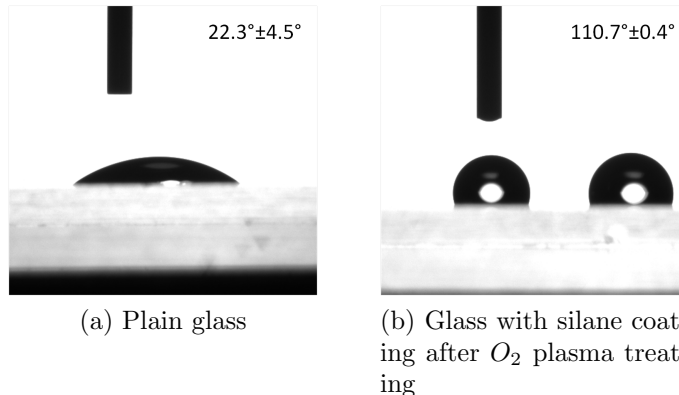


Figure 2.9: Contact angle measurement of glass at three different conditions

The contact angles of water phase in air were measured by CAM 200 (Figure 2.8(a)) from KSV Instruments in the laboratory of Center for Hydrate Research. The accuracy of this instrument is  $0.1^\circ$ . Because of the restriction of the lab, only DI water contact angle in the air was measured. For each measured sample, at least

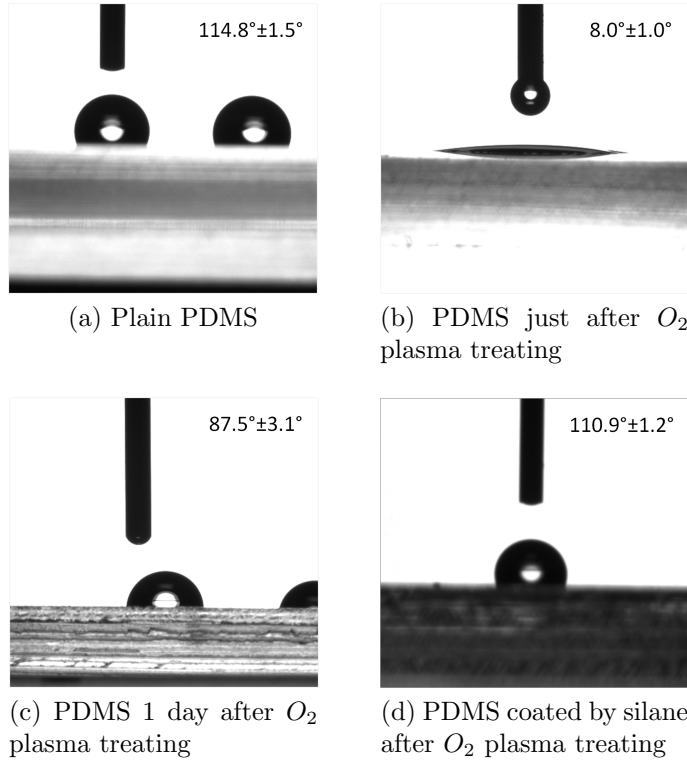


Figure 2.10: Contact angle measurement of PDMS at four different conditions

10 droplets were placed at different positions of the surface and measured in order to minimize the error. Because of the large spread area on hydrophilic surface, the contact angle on a hydrophilic surface has larger error than that measured on a hydrophobic surface. The standard error for a hydrophilic case is from  $1^\circ$  to  $4^\circ$  and for a hydrophobic case is around 1 degree.

Figure 2.9 shows that plain glass is very hydrophobic with an average contact angle of  $22.3^\circ \pm 4.5^\circ$ . After the oxygen plasma treatment, the glass became extremely hydrophobic. The water droplet quickly spreads and the contact angle is nearly  $0^\circ$ . Silane treatment is very effective to generate hydrophobic wettability for glass substrate after oxygen plasma bonding. The average contact angle is  $110.7^\circ \pm 0.4^\circ$ . Figure 2.10 shows that PDMS treated by oxygen plasma has a strong hydrophilic wettability within 30 minutes with an average contact angle of  $8.0^\circ \pm 1.0^\circ$ . After 24 hours, PDMS returns to intermediate wettability with a contact angle of  $87.5^\circ \pm 3.1^\circ$ .

After silane coating, the contact angle of PDMS is  $110.9^\circ \pm 1.2^\circ$ , which is very close to the silane coated glass. This shows that silane coating can be applied to create uniform wettability in our microfluidic micromodel.

### 2.3.2 Effectiveness of silane coating

In the previous section, the effectiveness of silane treatment applied to the surfaces of PDMS and glass is proved. However, in the micromodel fabrication process, silane treatment must be applied after the oxygen plasma bonding. Because it was not clear whether silane molecules can freely enter channels, water and mineral oil were infused into a micromodel that was exposed to silane vapor for 4 hours. The contact angle between water and oil phases inside the channel were measured by ImageJ-Fiji using the microscope pictures.

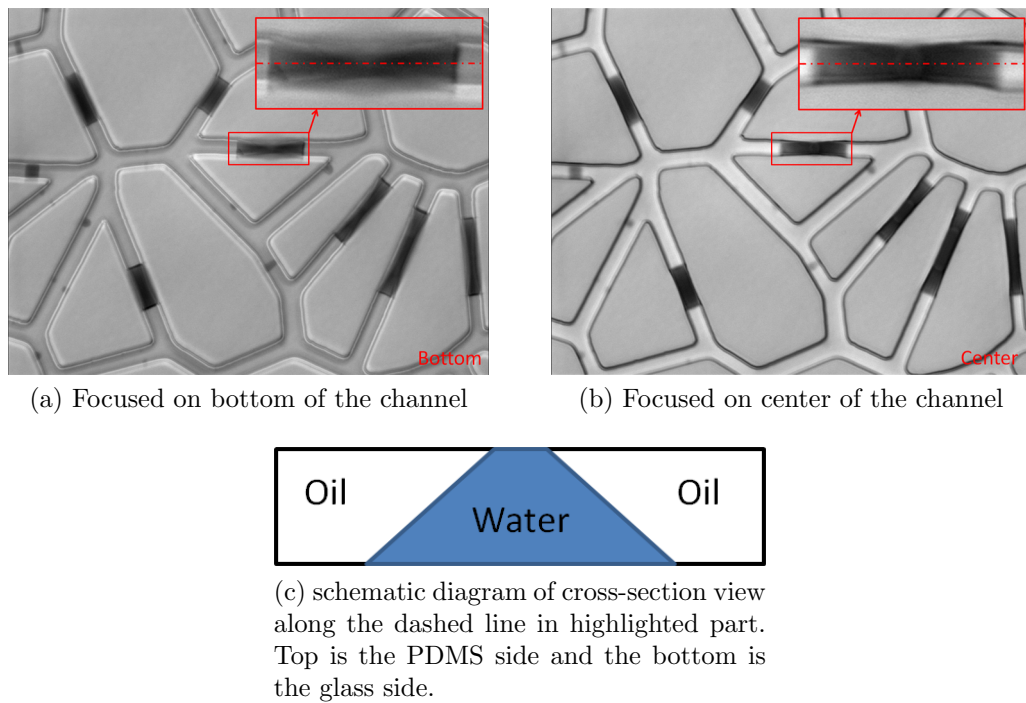


Figure 2.11: Non-uniform wettability before silane coating (200x Magnification)

For micromodel without silane coating, the porous media analog was firstly saturated with water (dark color) and then infused with oil (light color). From the left

figure, at the bottom of the channel (glass side), the color is lighter at both sides of the highlighted water slug than in the middle. At the middle of the channel, it is clear that water is more saturated than at both sides. Combining these two views, the shape of water slug along the highlighted cross-section should be trapezoid, whose schematic diagram is shown in Figure 2.11(c).

The trapezoidal shape of the cross-section and the preference of water to adhere to the glass show that the glass is hydrophilic. On the bevel zone of the trapezoid, the color of water is lighter than that in the middle, suggesting that oil is on top of the water. By a contact angle around  $87^\circ$ , the PDMS wall is intermediately wet between water and oil. Additionally, some water dots were identified in confocal image focused to the vicinity of the glass slide, but was nearly faded out in the image focused to the middle of the channels. This observation further supports that the PDMS and the glass substrate have different wettability to oil and water phases.

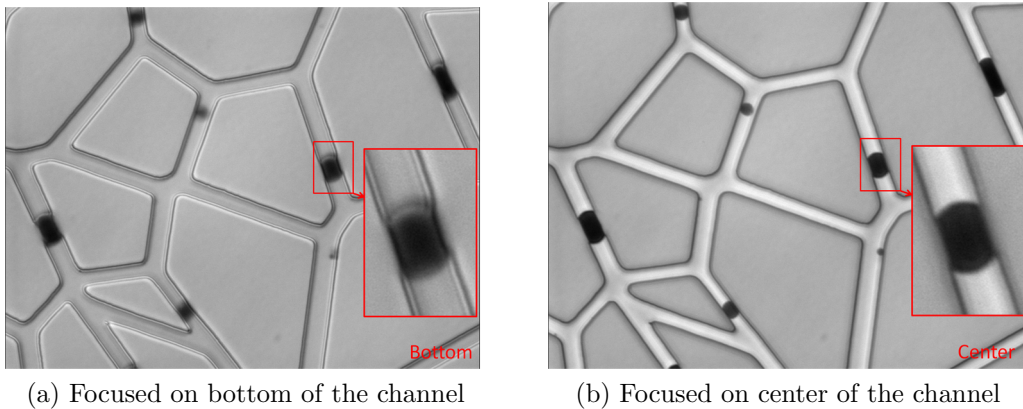


Figure 2.12: Uniform wettability after silane coating (200x Magnification)

To make the wettability uniform, after plasma bonding, the newly bonded microfluidic micromodels were vacuumed, exposed to silane vapor for 3 minutes , and then kept in the vacuum chamber for 4 hours. Using inverted microscope, we examined the effects of silane coating following the same steps as mentioned earlier. The interface on the bottom and middle level is similar and the contact angle is about

120 degree, which shows the PDMS wall is hydrophobic as well as the glass substrate. This also serves as a direct measurement of the contact angle of the water-oil system in a silane-coated PDMS/glass micromodel, showing that the micromodel is oil-wet.

### 2.3.3 Wettability characterized by laser-induced fluorescence under the confocal microscope

To further verify the effectiveness of the silane coating, confocal microscope was used to examine oil-water systems labeled with laser-induced fluorescence. This microscope can scan different height (Z value) of micromodel channels and generate cross-section and 3D view, which shows the distribution of wetting and non-wetting fluids.

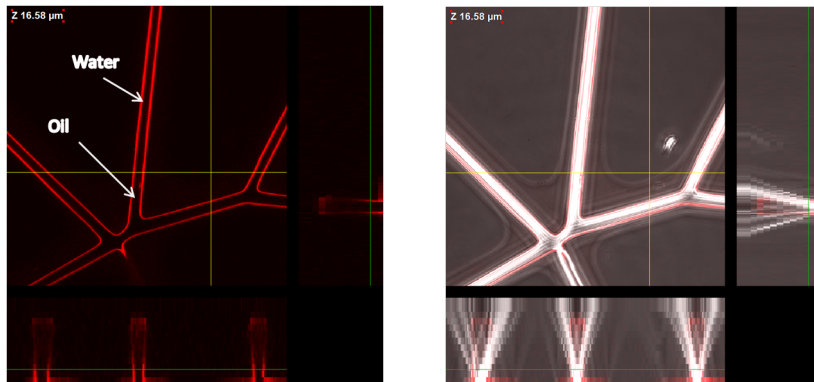


Figure 2.13: Cross-section view of a channel with fluorescent dye (Left) and a combined fluorescent and optical view of the channel (Right) under water-wet condition just after bonding. The Channel is  $60\ \mu\text{m}$  in height and  $11\ \mu\text{m}$  in width. The red phase is water dyed with Texas Red, and rest of the channel is filled with oil. The yellow lines in the top-down view show the location of XZ and YZ cross-section location. The green lines in cross-section views show the focus level (Z value) in the micromodel.

In the Figure 2.14, at the glass side there is only oil present. There is no water film on the glass like in the Figure 2.13, which indicates that the glass substrate is oil-wet. With increasing Z value, water began to appear in the middle of the PDMS channel. When the Z-value continued to increase, the water in channel became narrow. The two sides and the top of the channel were all occupied by oil. From these cross-section

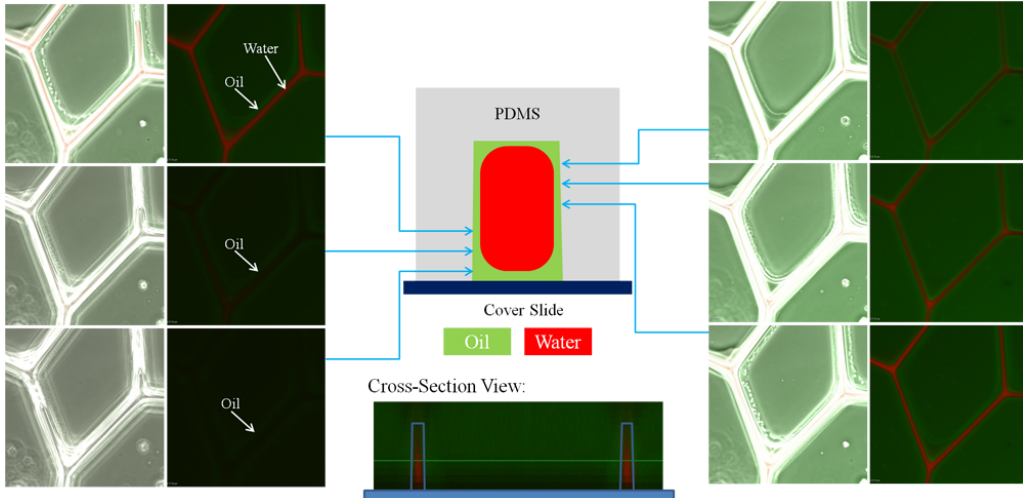


Figure 2.14: Confocal microscope and laser-induced Fluorescence (Texas Red in water phase and BODIPY in oil phase) show the distribution of fluids in a silane-treated channel. The channel is  $60\ \mu\text{m}$  in height and  $11\ \mu\text{m}$  in width. The green lines in cross-section views show the focus level (Z value) in the micromodel.

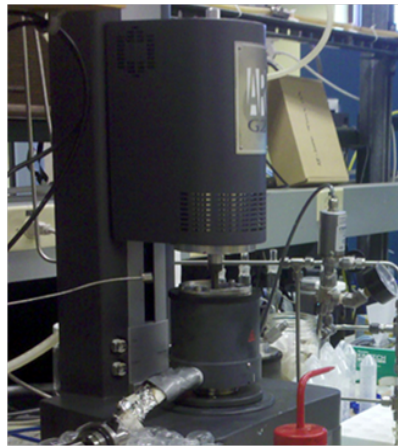
views, it is clear that the wettability of the silane-treated channels is uniformly oil-wet.

We also tried to use confocal microscope to quantify the two phase distribution in our silane treated channels. In the previous (Wu et al., 2012) and the current study, the wetting phase clinging on the wall cannot be observed and measured by top-down viewing through a regular microscope. However, this attempt did not succeed because the absorption of the fluorescence dye for the oil phase. From the Figure 2.14, it is clear that the BODIPY dye in the oil phase had infiltrated the PDMS matrix and made it impossible to isolate and quantify the oil phase.

## 2.4 Fluid Properties (Density, Viscosity and the IFT measurements)

### 2.4.1 Properties of Ethoxylated Alcohol (EA)

In this research, NEODOL 91-8 ethoxylated alcohol, a nonanionic surfactant from Shell Chemicals was chosen to make surfactant solution. Alamdari et al. (2012) used this ethoxylated alcohol in surfactant flooding test. Compared with other surfactant, ethoxylated alcohol generates little emulsion, which is advantageous for after-production separation of oil and water phases.



(a) Discovery Hybrid Rheometer-3



(b) Spinning Drop Tensiometer

Figure 2.15: Apparatus used to characterize fluids properties

From the production data of Shell Chemical, density of this NEODOL 91-8 is similar to water. The solution of this EA product in water is transparent. The CMC value of NEODOL 91-8 is 380 ppm, which can be easily achieved in our experiment.

Table 2.1: Properties of NEODOL 91-8 Ethoxylated Alcohol at 40 °C

Density g/cc	Kinematic Viscosity cSt	CMC ppm
0.996	27	380

#### 2.4.2 Viscosity measurements

Viscosity measurements were performed using a cone-plate rheometer shown in Figure 2.15(a) (Discovery Hybrid Rheometer-3, TA instruments). The employed cone-plate geometry has 2° cone angle and 40 mm diameter, which allowed for shear rates up to  $8,500\text{ s}^{-1}$  to be explored. All measurements were conducted at  $25^\circ \pm 0.1^\circ\text{C}$ , with temperature control provided by the Peltier element. For steady-state measurements, it was programmed to accept point if 3 consecutive measurements taken every 3 seconds are within 3% of each other in a 2 minute window. The shear rates investigated ranged from 0.1 to  $100\text{ s}^{-1}$  during the shear rate ramping step. 2

data points per decade were collected (7 points total).

In this research, the viscosity of brine, surfactant solution and light mineral oil is measured by DHR-3. The results are presented in Table 2.2.

#### **2.4.3 IFT measurement and optimal concentration of EA in brine**

In this research, interfacial tension between oil and brine phases was measured by a spinning drop tensiometer from TIORCO in Denver.

This spinning drop tensiometer is shown in Figure 2.15(b). It uses a tube that contains a droplet of fluid of lesser density suspended in a bulk fluid with higher density. When the tube is rotated rapidly around its long axis, the droplet moves to the center of the tube and is deformed. By using the deformation of the drop, the densities of the fluids and the rotational speed, the interfacial tension can be obtained from the shape of the interface by computerized image analyses. It can measure extremely low IFT between oil and water generated by surfactant. Also, the IFT at reservoir temperature can be measured. Because the surfactant is quite sensitive to reservoir temperature, it is a good tool to study the stability of surfactant at in-situ temperature. Because this micromodel study was carried out at room temperature, the IFT measurements were also conducted at room temperature.

In order to measure the needed fluid density for interfacial tension measurement, we used a 10ml pipette to sample oil and measured its weight to calculate the density. A fixed 10 ml volume was taken by the pipette, and the measurement of mass was done by using a precision top-loading balance (Denver Instruments, PI-6001). The readability of the precision top-loading balances is 0.1 g, the repeatability is 0.2 g, and the linearity is 0.2 g. The maximum error of 10 ml pipettes is  $\pm 0.1$  mL, so the relative error is  $\pm 1.0\%$ . The density of mineral oil, measured by the pipette and the balance, is 0.848 g/cc. The Standard deviationfig:non-uni wet is 0.008 g/cc. This density was used in the IFT measurements.

In this research, we measured the IFT between the mineral oil and eight brine/EA solutions. The concentrations of brine were 0.5 wt% or 1.5 wt%, and four different EA concentrations were applied to two brine solution: 0 wt%, 0.1 wt%, 0.5 wt% and 1.0 wt%.

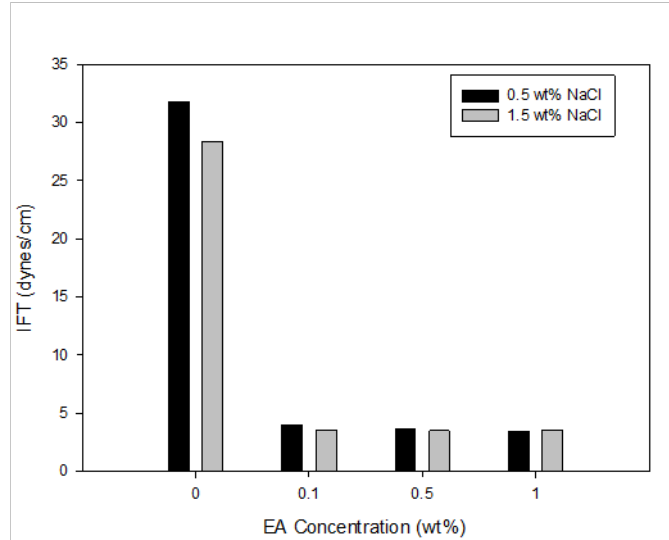


Figure 2.16: IFT between brine with different EA concentration and light mineral oil

Table 2.2: Properties of fluids at 25 °C

Fluids	Density g/cc	Viscosity cP	IFT dynes/cm
DI water	1	0.89	Not Measured
Brine with Food dye (NaCl:1.5 wt%, Food dye: 1.0 wt%)	1.006	0.94	28.37
Brine with Food dye and EA (NaCl:1.5 wt%, Food dye:1.0 wt%, EA:0.5 wt%)	1.007	1.13	3.57
Mineral Oil	0.848	42.46	N/A

From Figure 2.16, for the two brine tested, lower salinity led to higher IFT. EA can reduce the interfacial tension to about 1/10 of the original (without EA). In

this study, due to the insignificant variation in the IFT with NaCl concentration and with surfactant concentration beyond 0.1 wt%, we used 1.5 wt% NaCl brine and 0.5 wt% EA in water and surfactant flooding tests. A light mineral oil (O121-4, Fisher Chemical) was used as the oleic phase in this research. Blue food dye (1.0 wt% FD&C #1, Spectrum Chemical) is added to both the brine and the EA solutions to visualize the aqueous phase.

## 2.5 Experiment Setup and Control

In this study, compressed nitrogen is used to drive the displacing liquid. The inlet pressure is controlled by a miniature precision pressure regulator (R-800-30, AIRTROL) and measured by a digital pressure gauge (0–50 psi, SSI Technologies). The outlet pressure is the same as atmosphere pressure. The inter-connections were made by small-bore Tygon tubing (0.254 mm ID, Fisher).

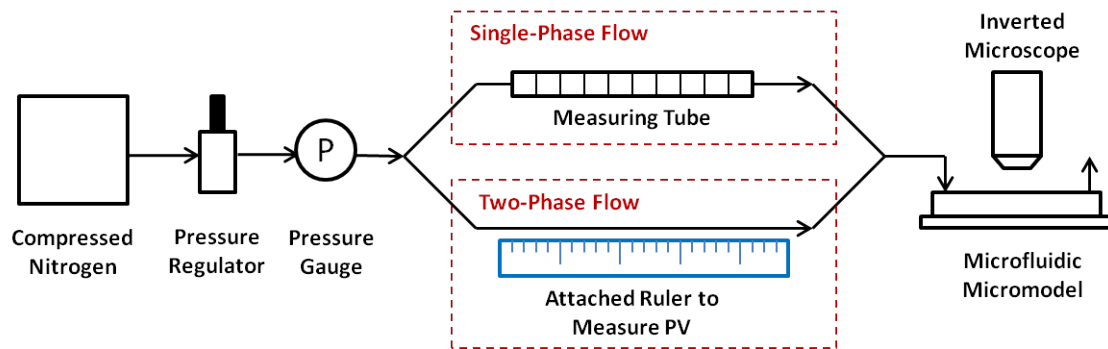


Figure 2.17: Schematic diagram of pressure-control system

In single-phase flow experiments, a measuring tube (0.84 mm ID) was connected between the pressure gauge and the  $\mu$ PMA to measure the flowrate.

In two-phase flow experiments, the flow is much slower than in the single-phase flow, and the flowrate is not constant in two-phase flow experiments because of the relative permeability changing with changing saturations. Thus, we removed the measuring tube in two-phase experiment. The pressure gauge and the  $\mu$ PMA were directly connected by a capillary tube with ID of 0.254 mm, and a ruler was attached

to the capillary tube to monitor the injection volume.

The average front velocity can be roughly calculated by this equation:

$$u = \frac{L}{t_{BT}} \quad (2.1)$$

Where  $u$  is the average front velocity,  $L$  is the length of the  $\mu$ PMA and  $t_{BT}$  is the breakthrough time. In this study, the average front velocity was used in the calculation of capillary number in 1.1.

### 2.5.1 Single-phase flow (permeability measurement)

In single phase flow experiment, we flowed DI water through the porous media under a constant pressure drop of 4 psi. The velocity was measured by recording the time it took for the gas meniscus to pass five calibration lines on the 0.84 mm ID measuring tube with 2mm interval. The flowrate is then obtained using velocity multiplied by the cross-section area of the measuring tube (0.84mm ID). The permeability was calculated from the Darcy's Law using flow rates measured at different pressure drops (Wu et al., 2012). However, in this study we found that at high pressures the dependence between flow rate and the pressure drop had deviations from the expected linear behavior, possibly due to the deformation of the PDMS material. Therefore, only the rate at the lowest pressure was used to calculate the permeability.

### 2.5.2 Two-phase flow (water or surfactant flooding)

In water flooding experiments, firstly, brine (1.5 wt% NaCl) was injected at 15 psi to make sure there is no gas left in the porous medium, and seven 20x microscopic pictures were taken at different parts of the porous media for saturation analysis which will be discussed in detail in the next section. In the second step, mineral oil was injected at 15 psi for 20 minutes to displace water to establish the irreducible water saturation. Then, again, seven 20x microscopic pictures were taken at the end of this step. The irreducible water saturation is about 10% or less. The third step

was to flood with brine or surfactant solution (1.5 wt% NaCl, 1.0 wt% Food Dye and 0.5 wt% Ethoxylated Alcohol) at 1.5 psi. The injected volume of brine was monitored by a ruler attached to the capillary tube (ID = 0.254 mm). Pictures were taken at each 0.5 pore volume (PV) injected and at the water breakthrough. The flooding test was stopped after 3 PV of injection.

In the field, surfactant flooding always follows water flooding. Because of the high cost, it is uneconomical to inject chemicals too early. However, this research focuses on the effect of geometry and interfacial tension/capillary number on microscopic displacing efficiency. In order to maintain the initial condition, the brine with surfactant was directly injected.

## 2.6 Imaging Processing and Saturation Analysis

Because of the tiny size of the porous media models, the volume of displaced fluid is difficult to measure. Optical method was used instead to measure the saturations. In the previous study (Wu et al., 2012), 4 pictures were taken by a microscope using 20x magnification and were stitched in ImageJ software. The stitched picture was then converted to 8 bits and applied threshold of about 122 on a 0–255 scale to subtract the water-saturated area. In order to measure the change in saturation in the displacement process, first a picture of micromodel fully-saturated with water was taken as the entire pore area (100% water saturation). The water saturation was then determined by counting the number of pixels in water-occupied zones over the entire pore area.

Our  $\mu$ PMA is 30 mm long and 3 mm wide. With 20x inverted microscope (Olympus IX81), seven images are needed to cover the whole  $\mu$ PMA. The  $\mu$ PMA slide was fixed on the holder of the microscope and the seven photographic locations were saved in the Olympus microscope software. Images taken at the different stages of the flooding process (breakthrough time or 0.5 PV intervals) were named in the order of stages.

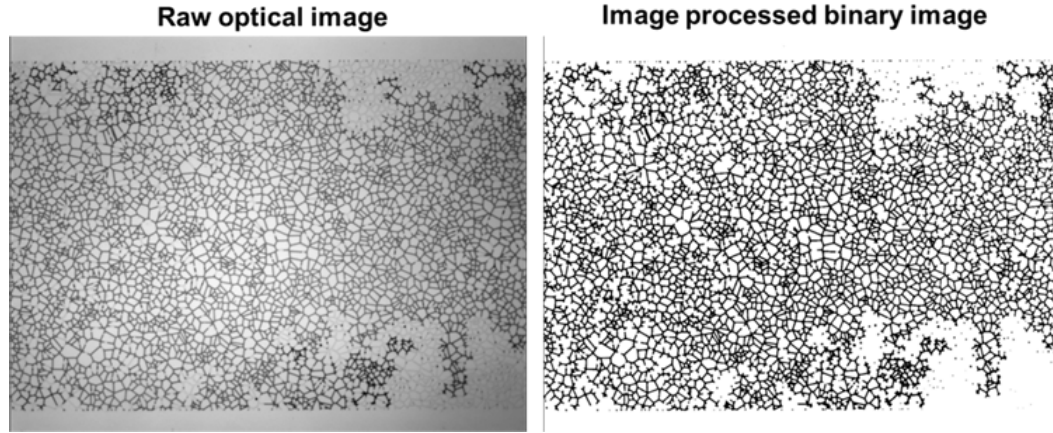


Figure 2.18: Image processing by Image-Fiji

ImageJ-Fiji, an open source image processing software, was used to process and analyze the microscopic images. A macro was written to batch-process the images, as shown in the flowchart in Figure 2.19. The example image is shown in Figure 2.18. After that, another macro, the flowchart which is shown in Figure 2.20, was used to analyze the binary images to get the area fraction data for the water saturation calculation. These data were then manually saved in a CSV file.

A Matlab script was developed to calculate the recovery factor. The flowchart is shown in Figure 2.21. It reads the CSV file that is previously saved and calculates the water saturation by dividing the area fraction of current stage by the fraction of the fully saturated  $\mu$ PMA. Using the saturation of the origin oil in place (OOIP), which was achieved by the area fraction of the oil saturated  $\mu$ PMA. The recovery factor at different stages can be calculated by the following equation:

$$RF = \frac{S_w - S_{wi}}{1 - S_{wi}} \quad (2.2)$$

Where: RF is the recovery factor;  $S_w$  is the water saturation;  $S_{wi}$  is the irreducible water saturation.

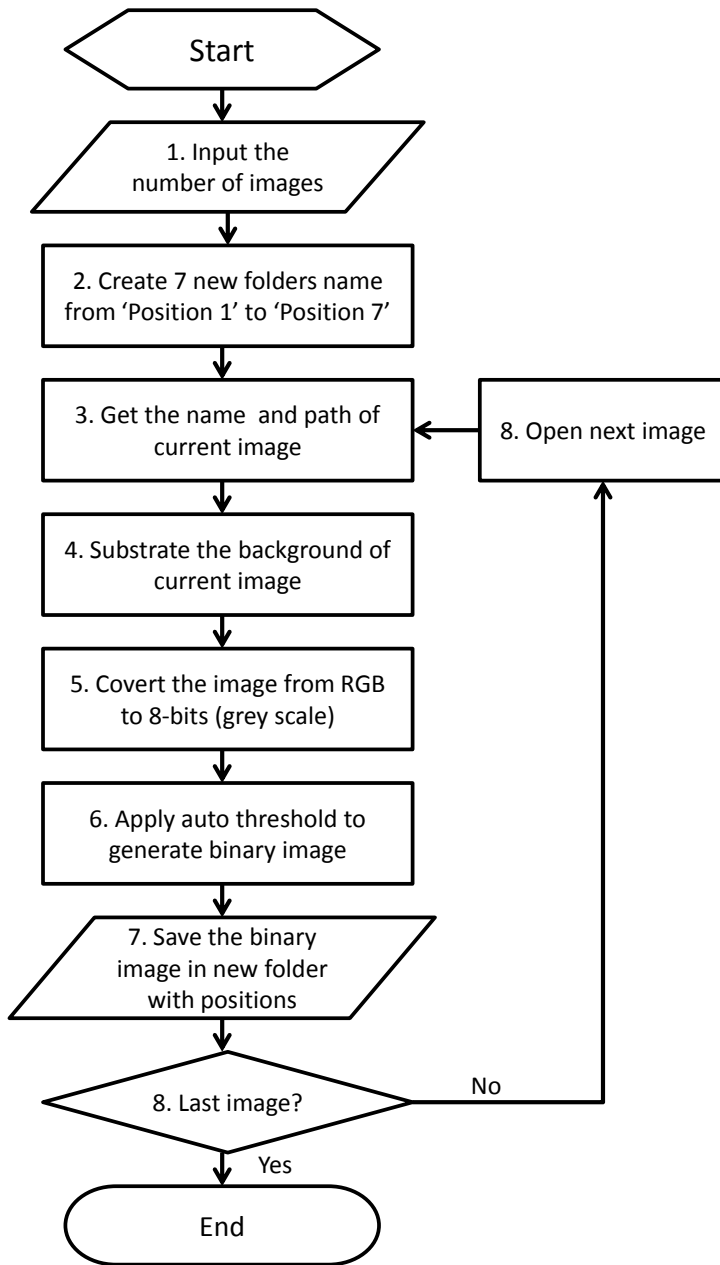


Figure 2.19: Flowchart of microscopic imaging processing in Image-Fiji. Steps: (1) Input the number of images in the sequence and open the first image. (2) Create seven new folders with names from Position 1 to 7. (3) Analyze the file name of the current image to extract location information. (4) Substrate the background of the current image, and enhance the contrast (optional). (5) Convert the image from RGB to 8-bits grey scale. (6) Apply automatic thresholding to generate a binary image. (7) Save the binary image in new folder with positions. (8) open the next image and follow step 2 to 7 until the last image is processed.

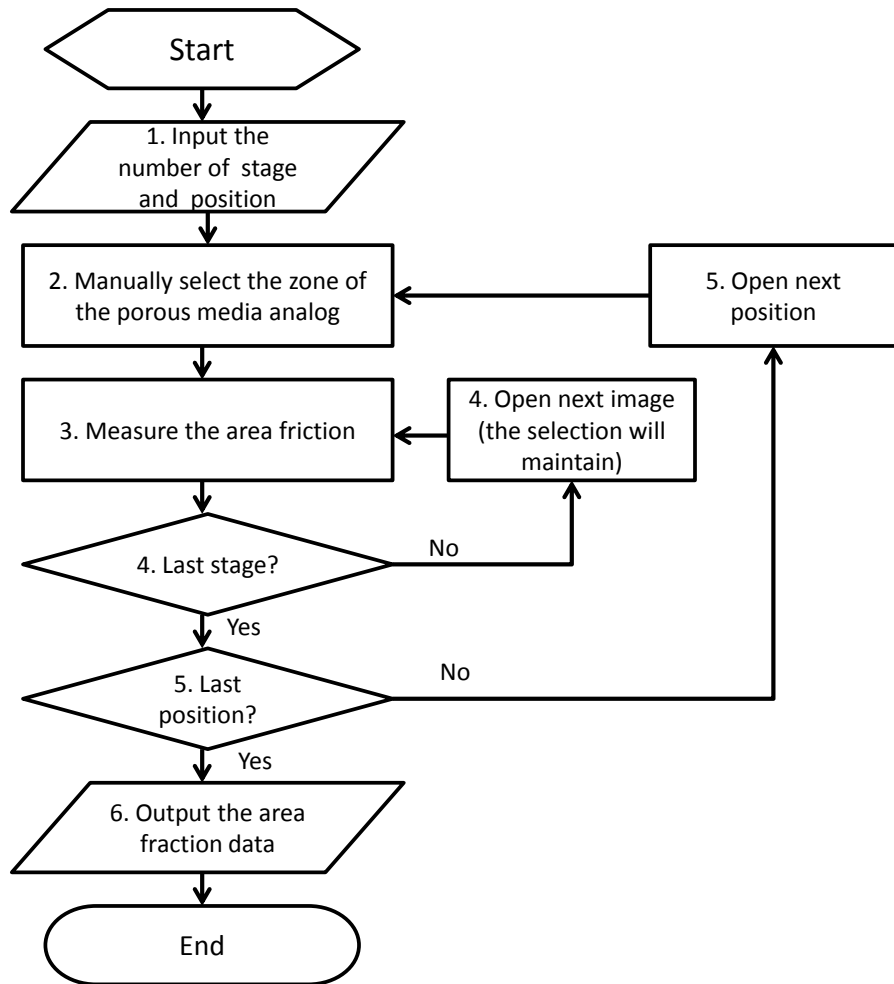


Figure 2.20: Flowchart of pixel Analysis in Image-Fiji. Steps: (1) Input the number of stages and positions and open the first binary image in the first position folder. (2) Manually select the zone of the  $\mu$ PMA . (3) Measure the area fraction. (4) Go to the next picture (the zone selected in step 2 remains the same) and measure the area fraction till all images in the folder are processed. (5) Repeat steps 1 through 4 to process images stored in other position folders. (6) Save the area fraction data to a CSV file

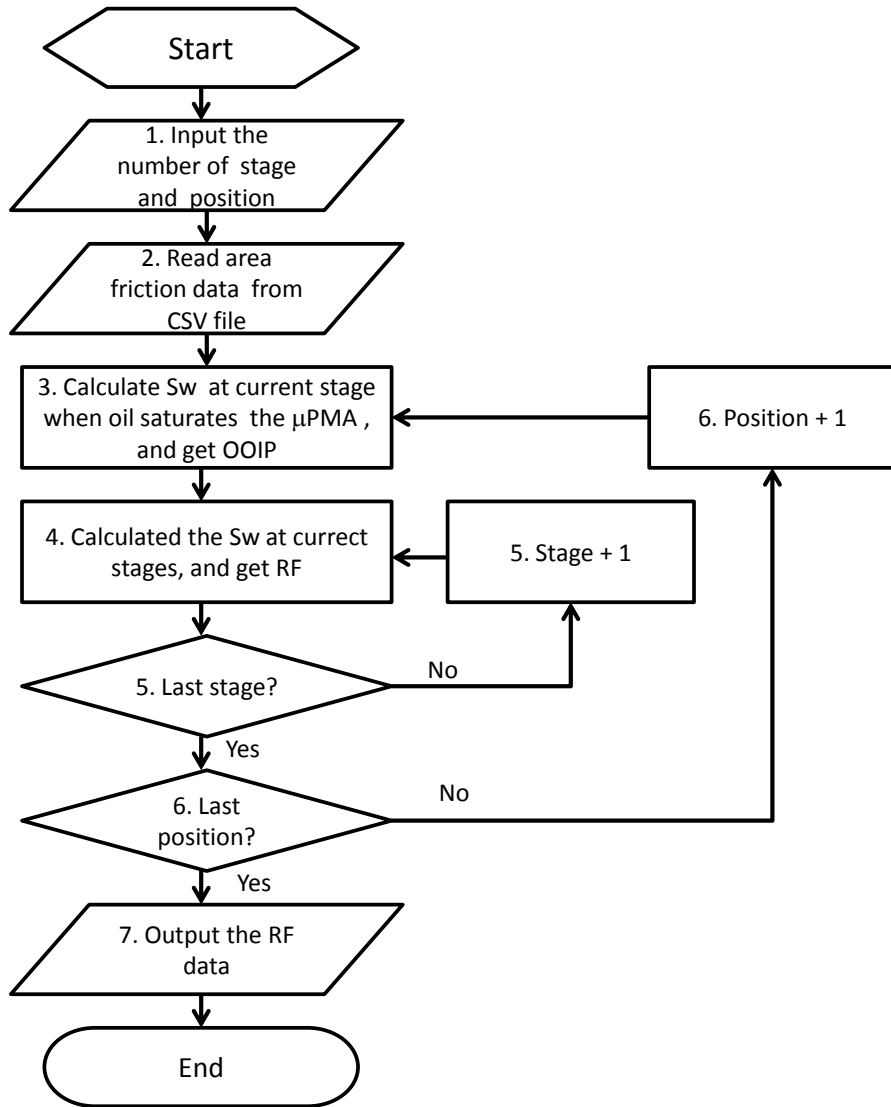


Figure 2.21: Flowchart of Recovery Factor Calculated in MATLAB. Steps: (1) Input the number of stages and positions. (2) Read area fraction data from the CSV file. (3) Calculate the water saturation at the current location of stage 2, and calculate the saturation of OOIP. (4) Calculate the Sw of the current stage (start from 3), and calculate the recovery factor. (5) Repeat steps 4 until the last stage is processed. (6) Repeat steps 3–5 until the last position processed. (7) Output the recovery factor.

## CHAPTER 3

### SINGLE-PHASE FLOW EXPERIMENTS AND PERMEABILITY

In this chapter, single phase flow experiments were conducted to measure the permeability of each porous media analog. The measured results were compared with LB 3D simulations and the Kozeny equation.

#### 3.1 Theoretical Calculation Based on Kozeny Equation

Besides experimental measurements, we also calculated the permeability using the Kozeny equation:

$$k = \frac{\phi^3}{cs^2} \quad (3.1)$$

Where:  $k$  is the permeability,  $\phi$  is the porosity,  $c$  is the Kozeny constant which is taken as five for random geometry(Wu et al., 2012), and  $s$  is the specific surface area defined as surface area per unit volume of porous medium. The specific surface area was calculated by the following equation:

$$s = \frac{p_c h + 2A_c}{Lwh} \quad (3.2)$$

Where:  $p_c$  is the perimeter of the 2D Voronoi diagram based on which  $\mu$ PMA is made,  $A_c$  is the area of ceiling or floor of the channels,  $L$  is the length of the  $\mu$ PMA,  $w$  is the width of the  $\mu$ PMA and  $h$  is the height of the  $\mu$ PMA. The units in this equation must be SI.

Wu et al. (2012) showed that the Kozeny equation overestimates the permeability of  $\mu$ PMA with vugs. So in this research, Kozeny equation was only applied to homogeneous analogs (U, D, S and H) to estimate their permeability.

### 3.2 Method and Equations

In the single phase flow experiment, with increasing pressure, the increase in the flow rate did not show a good linear relationship. There was always a negative intercept, which means at high pressure, the flow rate was higher than expected based on Darcy's law with a constant permeability and fluid viscosity. Several researchers (Gervais et al., 2006; Hardy et al., 2009; Sollier et al., 2011) showed that PDMS begins to deform at about 2 psi. From the measured data with pressure drop of 4, 8, 12, 16 and 20 psi, the nonlinear increase in the flow rate at high pressure observed in our experiments is probably due to PDMS deformation due to elevated pore pressure. Hence, in this study, only the flow rate at 4 psi data was used to calculate the permeability.

Darcy's law was used in this research to calculate the permeability:

$$Q = \frac{kA}{\mu} \times \frac{\Delta P}{L} \quad (3.3)$$

Where: Q is the flow rate; k is permeability; A is the cross-section area of the  $\mu$ PMA;  $\mu$  is the viscosity of the liquid; dp is the pressure drop along the  $\mu$ PMA; L is the length of the  $\mu$ PMA.

In the single-phase flow experiment, the flow rate was achieved by:

$$Q = \pi \left( \frac{D}{2} \right)^2 \frac{dl}{dt} \quad (3.4)$$

Where: D is the diameter of the measuring tube; dl is the interval of scales on measuring tube; dt is the time interval for meniscus to pass the distance of dl.

The cross-Section area of  $\mu$ PMA can be calculated by:

$$A = w \times h \quad (3.5)$$

Where: w is the width of the  $\mu$ PMA; h is the height of the channels.

Substitute 3.4 and 3.5 into 3.3, the permeability is obtained:

$$k = \frac{\mu L \pi \left(\frac{D}{2}\right)^2 dl}{\Delta P w h dt} \quad (3.6)$$

### 3.3 Results and Comparison with LB Simulations

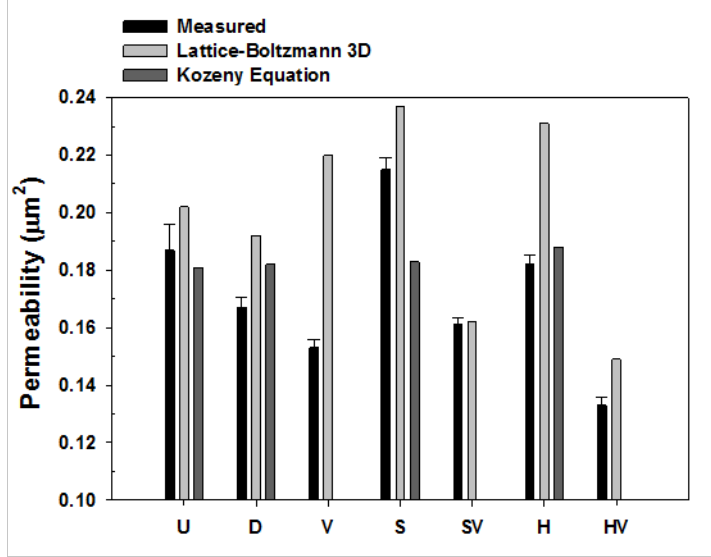


Figure 3.1: Permeability by single-phase experiments, LB 3D simulations and the Kozeny equation

Table 3.1: Parameters and permeability results of  $\mu\text{PMA}$

	No. of Grains	Porosity	Measured( $\text{Stdev}$ ) $\mu\text{m}^2$	LB 3D $\mu\text{m}^2$	Kozeny Equ $\mu\text{m}^2$
U	25626	0.190	0.187(0.0091)	0.202	0.181
D	25629	0.191	0.167(0.0037)	0.192	0.182
V	3413	0.185	0.153(0.0027)	0.220	-
S	29088	0.192	0.215(0.0042)	0.237	0.183
SV	6250	0.189	0.161(0.0026)	0.162	-
H	25000	0.190	0.182(0.0035)	0.231	0.188
HV	7344	0.185	0.133(0.0026)	0.149	-

From Figure 3.1 and Table 3.1, the measured data is 0.01–0.07  $\mu\text{m}^2$  lower than those from LB simulation. A possible reason for the deviation is that the depth our silicon master for PDMS molding is  $14.2 \pm 0.2\mu\text{m}$ , which is about 1  $\mu\text{m}$  less than designed. The LB simulation is base on a depth of 15  $\mu\text{m}$ . The shallower depth of

the channels will reduce the permeability. For the four homogenous micromodels, the Kozeny equation calculations were based on the true depth of 14  $\mu\text{m}$  so that the results are closer to measured ones.

### 3.4 Error Analysis

In this study, the error of our equipment was calculated by the error propagation law, and compared with the experimental error (standard deviation of calculated permeability, which is shown in Figure 3.1 and Table 3.1). The most common formula of error propagation law is:

$$\delta f = \sqrt{\left(\frac{\partial f}{\partial x}\right)^2 \delta x^2 + \left(\frac{\partial f}{\partial y}\right)^2 \delta y^2 + \left(\frac{\partial f}{\partial z}\right)^2 \delta z^2 + \dots} \quad (3.7)$$

Where:  $s_f$  is the error cause by several independent variables;  $x, y, z \dots$  are the independent variables;  $\delta x, \delta y, \delta z \dots$  are the errors of independent variables.

Substitute 3.6 into 3.7, the error of permeability is:

$$\begin{aligned} \delta k = & \sqrt{\left(\frac{\delta k}{\delta \mu}\right)^2 \delta \mu^2 + \left(\frac{\delta k}{\delta L}\right)^2 \delta L^2 + \left(\frac{\delta k}{\delta dl}\right)^2 \delta dl^2 + \left(\frac{\delta k}{\delta D}\right)^2 \delta D^2 + \left(\frac{\delta k}{\delta \Delta P}\right)^2 \delta \Delta P^2} \\ & + \left(\frac{\delta k}{\delta dt}\right)^2 \delta dt^2 + \left(\frac{\delta k}{\delta w}\right)^2 \delta w^2 + \left(\frac{\delta k}{\delta h}\right)^2 \delta h^2 \end{aligned} \quad (3.8)$$

In this research, these values were used at the errors of eight independent variables:

$$\delta \mu = 0.02 cP = 2 \times 10^{-5} \text{ Pa} \cdot \text{s} \quad (3.9)$$

$$\delta L = 0.1 \text{ mm} = 10^{-4} \text{ m} \quad (3.10)$$

$$\delta dl = 0.1 \text{ mm} = 10^{-4} \text{ m} \quad (3.11)$$

$$\delta D = 0.01 \text{ mm} = 10^{-5} \text{ m} \quad (3.12)$$

$$\delta \Delta P = 0.01 \text{ psi} = 2.76 \times 10^4 \text{ Pa} \quad (3.13)$$

$$\delta w = 10 \mu\text{m} = 10^{-5} \text{ m} \quad (3.14)$$

$$\delta h = 0.2\mu m = 2 \times 10^{-7}m \quad (3.15)$$

$$\delta dt = 0.1s \quad (3.16)$$

Figure 3.2 showed that the experimental error is less than the equipment error, which proved the reliability of our permeability measurement.

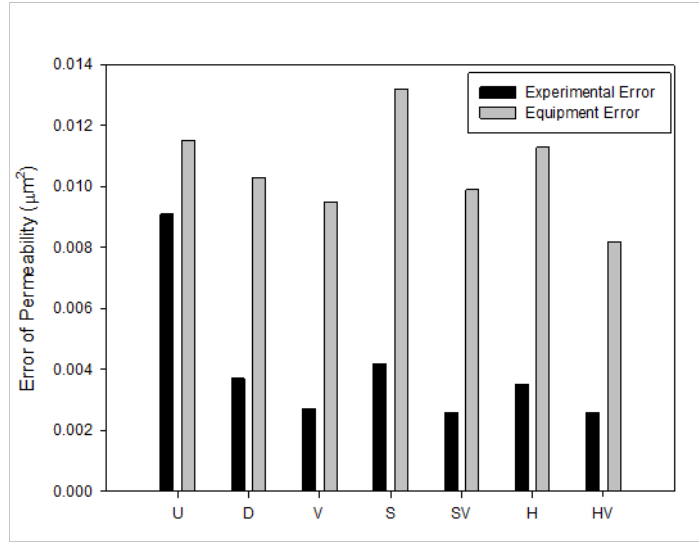


Figure 3.2: Equipment errors and experimental errors

The eight independent variables in the error calculation were analyzed to study their influence on the permeability. The errors from each independent variable,  $(\frac{\delta k}{\delta \mu})^2 \delta \mu^2$ ,  $(\frac{\delta k}{\delta L})^2 \delta L^2$ ,  $(\frac{\delta k}{\delta dl})^2 \delta dl^2$ ,  $(\frac{\delta k}{\delta D})^2 \delta D^2$ ,  $(\frac{\delta k}{\delta \Delta P})^2 \delta \Delta P^2$ ,  $(\frac{\delta k}{\delta w})^2 \delta w^2$ ,  $(\frac{\delta k}{\delta h})^2 \delta h^2$  and  $(\frac{\delta k}{\delta dt})^2 \delta dt^2$ , were devided by  $\delta k^2$  to get dimensionless errors. From Figure 3.3, the error from the measuring ruler (dl) is predominant. Then followed by the diameter of measuring tube (D), the viscosity ( $\mu$ ) and the height of  $\mu$ PMA. The errors in the length (L) and width (w) of  $\mu$ PMA, the pressure reading( $\Delta P$ ) and the time reading (dt) are negligible.

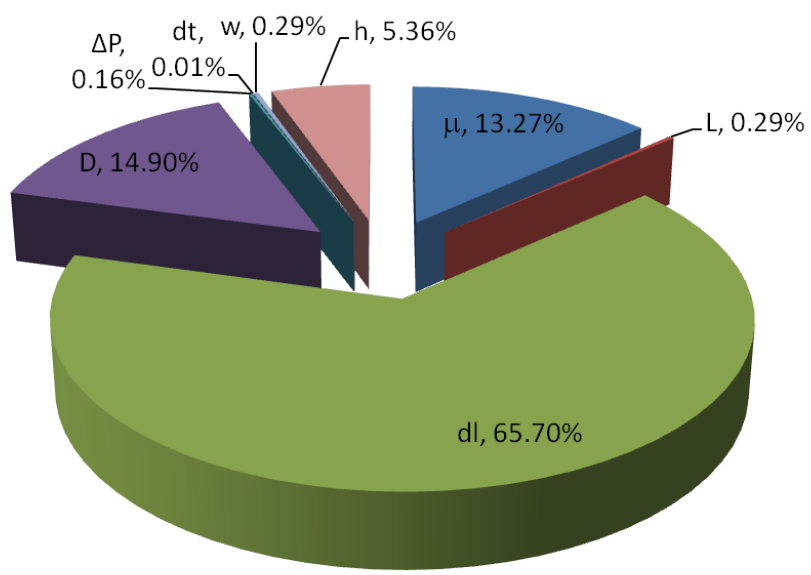


Figure 3.3: Dimensionless equipment errors

## CHAPTER 4

### WATER FLOODING TESTS: OBSERVATIONS AND MEASUREMENTS

In this chapter, we present the water flooding results. The tests were repeated under 1.5 psi driving pressure on each  $\mu$ PMA for at least three times. All micro-models used in water flooding were treated by silane so that the inside channels are hydrophobic. Breakthrough pattern and time were recorded for each analog. Also, the patterns at each 0.5 PV injected were recorded and the recovery factors were calculated.

#### **4.1 Breakthrough Pattern and Breakthrough Time**

In this section, the breakthrough patterns of water flooding in each porous media analog are presented. Some high magnification images are shown to illustrate the detail of water front movement. Finally, the breakthrough times and recovery factors will be tabulated and plotted for comparison.

##### **4.1.1 Water front movement and breakthrough pattern**

In Figure 4.1(a), the water flooding process is quite stable in the Chip U, showing a piston-like displacement. The first four positions were almost totally saturated by the displacing brine. From the fifth position, the water front began to develop some branches and started to break through in the center of the porous media analog. The edges of 6th and 7th were not fully swept. After the water front passed by, there is little residual oil left. The average breakthrough time of this analog is 2840s, and the average breakthrough recovery factor is 85.9%, which is quite high.

In Figure 4.1(b), the water front in the Chip D pore size distribution random geometry analog is not as stable as Chip U. Because the difference in pore size causes difference in the capillary pressure, which is the main resistance in water flooding

(drainage), water prefers to go through wider channels with less capillary pressure. The first three positions were almost filled entirely by the displacing water. From the 4th position on, the bypassing of water front began and there were many branches in the last three positions. As a result, there was significant amount of residual oil after water front went by. The average breakthrough time of this analog is 3171s, and the average breakthrough recovery factor is 75.4%, lower than Chip U.

In Figure 4.1(c), the water front prefers to go through the vugs rather than channels in Chip V. The first two positions were filled by displacing water. From the 3th position on, the fingering formed and waterfront went along the one side of the analog. As a result, there is a lot of residual oil in the other side of the porous media analog.

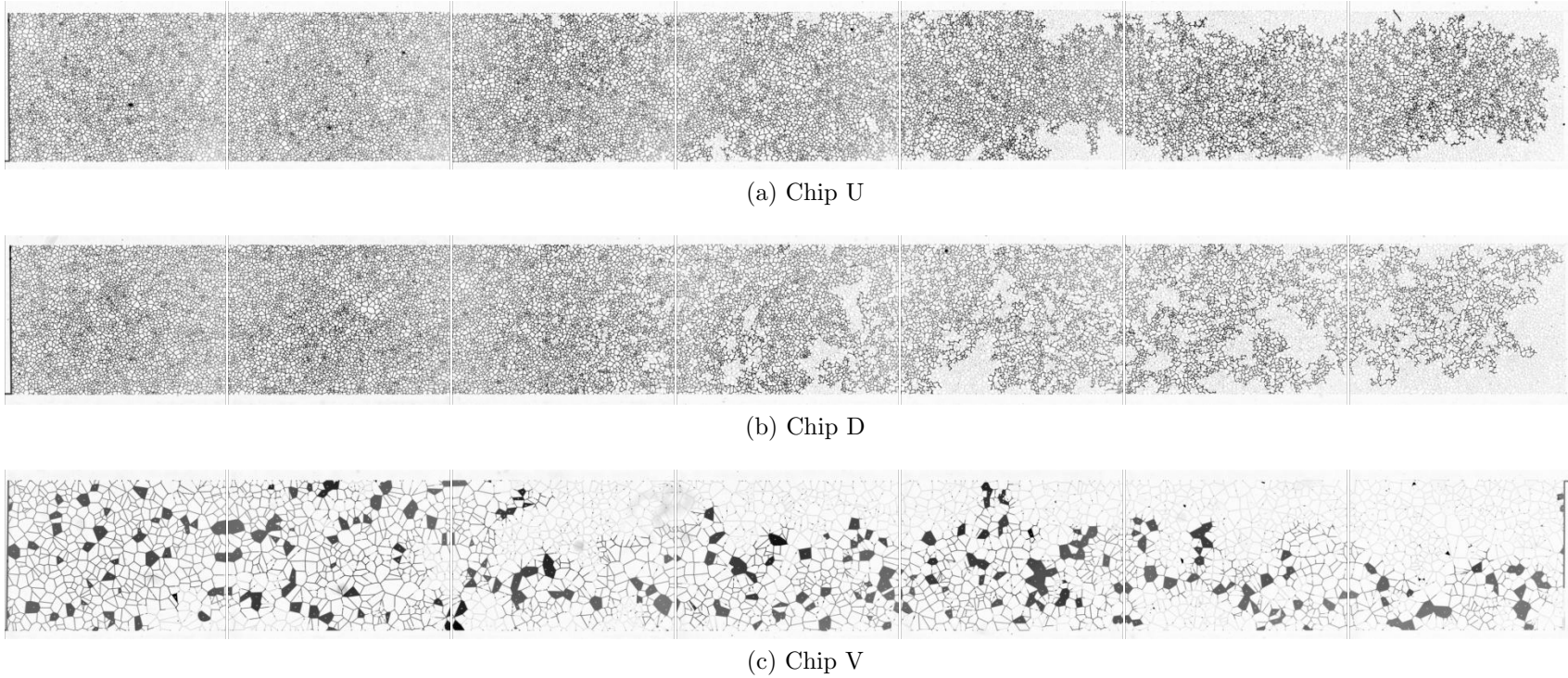


Figure 4.1: Breakthrough patterns of water flooding for Chip U, D and V

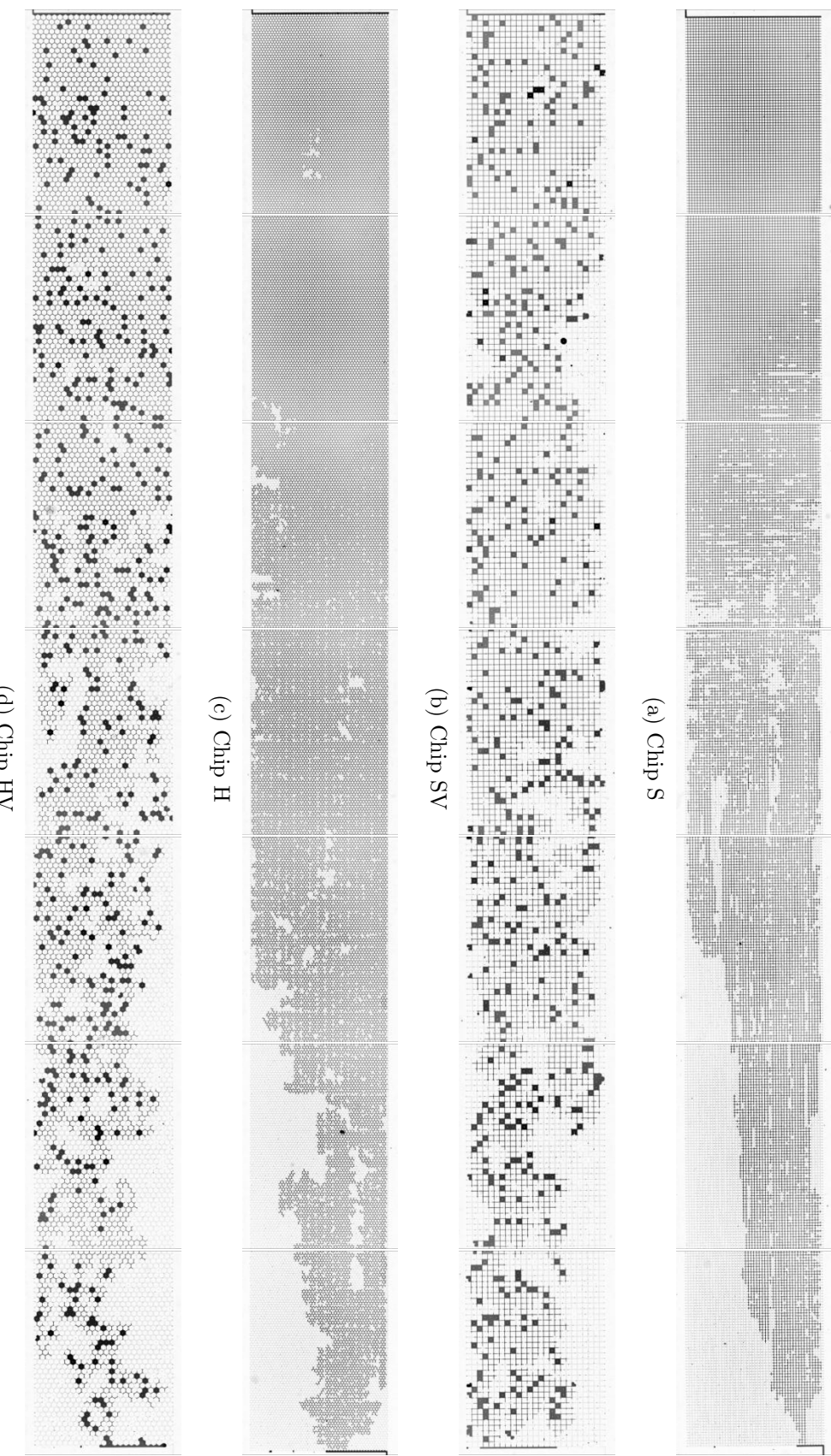


Figure 4.2: Breakthrough patterns of water flooding for Chip S, SV, H and HV

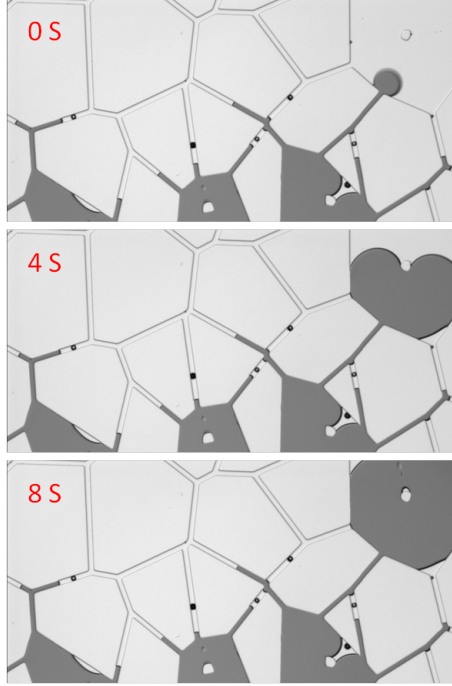


Figure 4.3: The interfaces in nearby channels withdrew when water entered vugs

Also, an interesting phenomenon was found at 100x magnification. In Figure 4.3, the water-oil interfaces in the channels were observed to retreat when water entered a nearby vug. The reason is that when water enters the vug, the low capillary pressure makes the vug a low-pressure area, generating water flow into the vug. Meanwhile, the displaced oil from the vug increases the local oil pressure and pushes water out from the smaller channels. This phenomenon also appeared in regular geometries with vugs (SV and HV). The average breakthrough time of this analog is 2658s, quicker than Chip U and D. The average breakthrough recovery factor is 65.5%, 20% lower than Chip U and 10% lower than Chip D.

In Figure 4.2(a), in the Chip S, the water front became sharper and sharper as it moved downstream. The first position was almost filled by the displacing water. From the second position on, there was some residual oil left. Water coning formed at position 5 and cut in the outlet, leaving large amount of unswept oil behind.

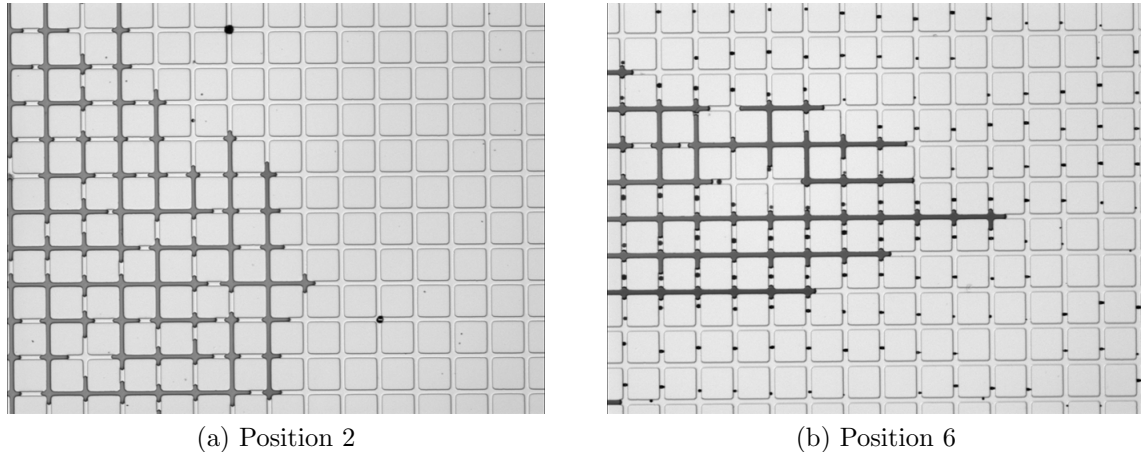


Figure 4.4: Different water flooding patterns of Chip S at position 2 and position 6

A special point for the water front in this square geometry is that the shape of the water front was different between the first four positions and the last three positions. As shown in Figure 4.2(a) and Figure 4.4, the water front in the first four positions was rather blunt; in contrast, the front appeared to be very sharp in the last three positions. There are two possible reasons to explain this phenomenon: pressure drop along the porous media and the straightforward channel directly connecting the inlet and outlet. Near the inlet the pressure is higher. The water can enter not only the straight channel, but vertical channels as well. When the water front reached the middle of the porous media, the pressure became much lower and insufficient to drive the water into the vertical channels. The vertical channels can be considered as equipotential lines at low pressure and the flow prefers to take a straight and horizontal path toward the exit. The average breakthrough time of this analog is 2741.6s, and the average breakthrough recovery factor is 67.8%. Compared with other homogenous geometries, this value is much lower due to the strong preference of the flow toward the horizontal channels.

The breakthrough feature of Chip SV appeared to be a combination of Chip V and S. The straight forward channels led to sharp front reaching for breakthrough. The vugs increased the heterogeneity of the porous media, further lowering the recovery

factor. The phenomenon shown in Figure 4.3 also happened in this geometry. In Figure 4.2(b), none of seven positions were fully saturated by water. In the second position, water front began to branch off and only one branch kept going. In the fourth and fifth position the water front became wider, and then narrowed down again in the following two positions till breakthrough. A lot of residual oil was left in position 3, 4, 6 and 7. The average breakthrough time of this analog is 2975s. The average breakthrough recovery factor is 57.8%, which is 10% low than Chip S periodic squares.

The breakthrough pattern of Chip H is quite similar to Chip U and is very differently from Chip S: it appears that the ‘Y’ junctions of the hexagonal structure effectively prevented the formation of a single sharp water cone. In Figure 4.2(c), the first and second positions were nearly saturated by the displacing water. The following three positions were well swept with little residual oil. At the last two positions, the water front went along one side of the micromodel and reached breakthrough. The average breakthrough time of this analog is 4328s, the longest in seven geometries. The average breakthrough recovery factor is 81%, a very high recovery that is second only to Chip U.

The breakthrough pattern of Chip HV hexagon vugs is quite similar to Chip D. The vugs increased the heterogeneity. In Figure 4.2(d), the first two positions were almost fully swept by the displacing water. The following three positions were highly swept, but some residual oil were trapped behind the front. From the fifth position on, the water front went along one side of the porous medium leaving an unswept zone on the other side. The average breakthrough time of this analog is 3030s, which is much faster than Chip H. The average breakthrough recovery factor is 71.3%, which about 10% lower than Chip H.

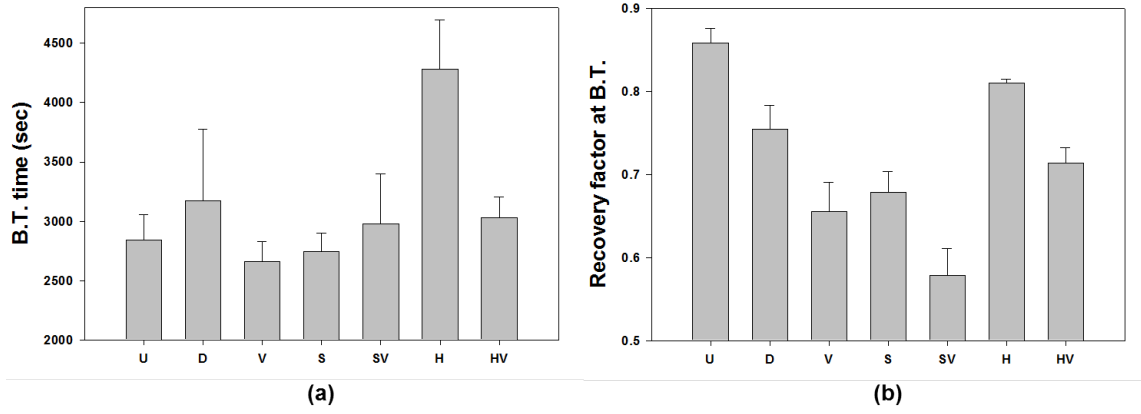


Figure 4.5: (a) Breakthrough times of water flooding (b) Recovery factors at breakthrough

#### 4.1.2 Breakthrough time, recovery factor and geometry effects

Figure 4.5(a) shows the breakthrough time and recovery factor of the water flooding process. Chip H, which has an average of 4328s, has the highest breakthrough time. The breakthrough times of other analogs are about 2600-3200s. The breakthrough of Chip S is a little bit quicker than the one of Chip U, because the straight line structure facilitates the formation of water coning . Except for Chip SV, the square vug geometry, the other two vuggy geometry Chip V and Chip HV have reduced the breakthrough times compared with Chip U and Chip D because of the heterogeneity. Chip SV is unique because the vugs help to spread the displacement fluid away from the horizontal and straight channels, delaying the breakthrough time.

From the Figure 4.5(b), Chip U and Chip H have the highest recovery factors at breakthrough. Specifically, their recovery factors are much higher than that of Chip S. For both random (Chip U, D and V) and periodic (Chip S, SV, H and HV) geometries, it is consistently observed that the presence of heterogeneity (vugs or pore size distribution) significantly lowered the recovery factor.

In Figure 4.6, the average recovery factor measured at breakthrough is plotted as a function of average breakthrough time. Except the Chip U and Chip SV, others five

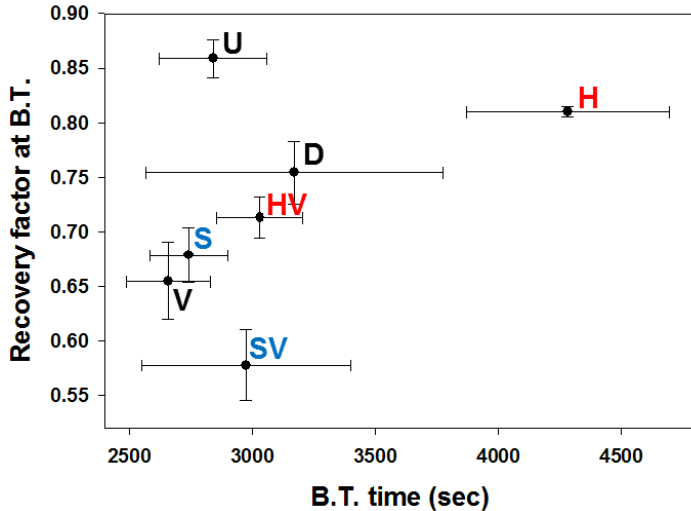


Figure 4.6: (a) Breakthrough times of water flooding (b) Recovery factors at breakthrough

geometries seem to indicate that the increase of breakthrough time is well correlated to the improvement in the recovery factor. While it is understandable that Chip S and Chip SV may have structures that are too special to fit into this general trend, it is not clear why Chip U showed a very short breakthrough time yet achieved a very high recovery factor at breakthrough.

## 4.2 Oil Recovery after Breakthrough and Geometry Effects

In the water flooding tests, 3 PV of water was injected and images were taken at intervals of 0.5 PV. In this section, the recovery factors as a function of injected PV are presented and the effects of geometry are discussed.

From Figure 4.7, the final recovery factors show the similar trend as the breakthrough one. The hexagon geometry, with a CN of three, has higher recovery factors than square geometry, with a CN of four in both homogenous and heterogeneous geometry. This result is opposite with another research on the effect of CN (Dehghan and Kharrat, 2009). Their results showed that the higher CN has the higher recovery factor. I think there are several possible reasons. The first one is the difference in

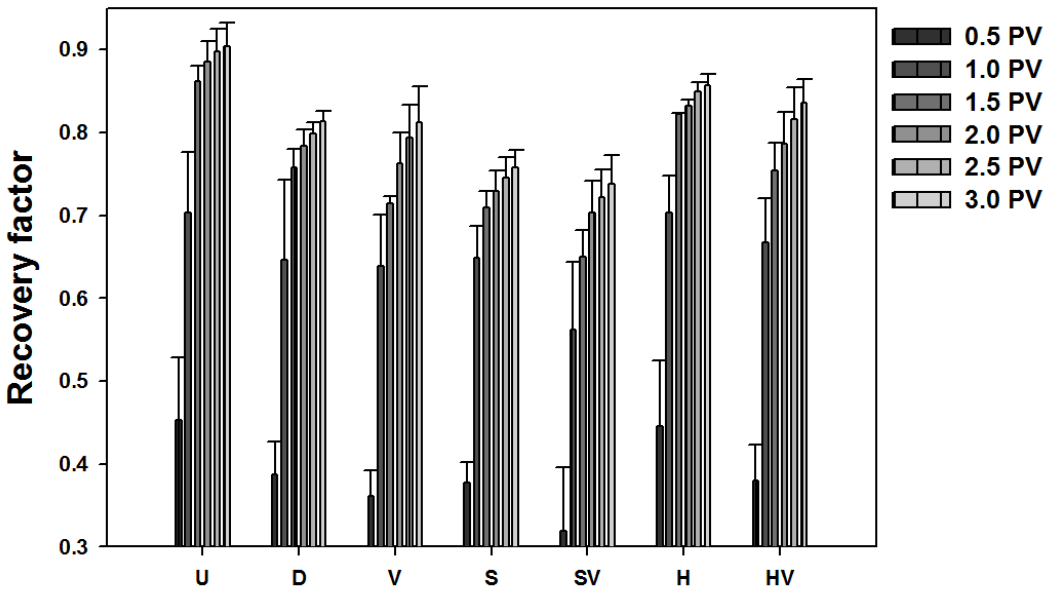


Figure 4.7: (a) Breakthrough times of water flooding (b) Recovery factors at breakthrough

porosity and permeability. The second one is the difference in the geometry, channels that are aligned and perpendicular to the pressure gradient direction; theirs are along the 45 degree diagonal directions. Also, their micromodels have pore to throat structures but our homogenous ones only have the channel. The third possible reason is that the straight line structure connected inlet and outlet line of our Chip S may lower the results.

As we compare homogenous and heterogeneous geometries, our results show that homogenous geometries all have higher recovery factors than heterogeneous geometries. For random geometry analog, the average recovery factor at 3 PV injected of uniform is 90.4%, of pore size distribution is 81.3%, and of vugs is 81.2%; for square geometry, the average recovery factor at 3 PV injected of square and square vugs are 75.8% and 73.8%; for hexagon geometry, the average recovery factor at 3 PV injected of hexagon and hexagon vugs are 85.7% and 83.6%. These differences in the recovery factors at 3 PV injected are all less than the differences observed at breakthrough.

## CHAPTER 5

### SURFACTANT FLOODING TEST: OBSERVATIONS AND MEASUREMENTS

In this chapter, we present the surfactant flooding tests, which were also carried under 1.5 psi driving pressuring for each  $\mu$ PMA and were repeated for at least three times. The concentration of EA is 0.5 wt%. As in the last section, we will first present breakthrough pattern and times recorded for each analog, and then the patterns and recovery factors at each 0.5 PV injected. We will show the differences between water flooding and surfactant flooding, and explain them in physical terms.

#### 5.1 Breakthrough Pattern, Breakthrough Time and Recovery Factor

In this section, the breakthrough patterns of surfactant flooding are shown and they are compared to those of water flooding in the last chapter. Also, the breakthrough times and recovery factors in surfactant flooding are presented.

##### 5.1.1 Observation of breakthrough pattern by surfactant flooding

Figure 5.1(a) showed that the addition of surfactant significantly improved the sweep efficiency. Except for the last position, oil at other positions was almost totally displaced by water. The average breakthrough of this analog is 1798.3s, and the average breakthrough recovery factor is 90.8%.

Figure 5.1(b) showed that surfactant also played an important role in Chip D. The branching of water front was significantly suppressed and residual oil saw significant reduction. This pattern looked like the one in Chip U, which indicates that the surfactant has successfully decreased the capillarity. The average breakthrough time of this analog is 1718.3s, and the average breakthrough recovery factor is 84.9%.

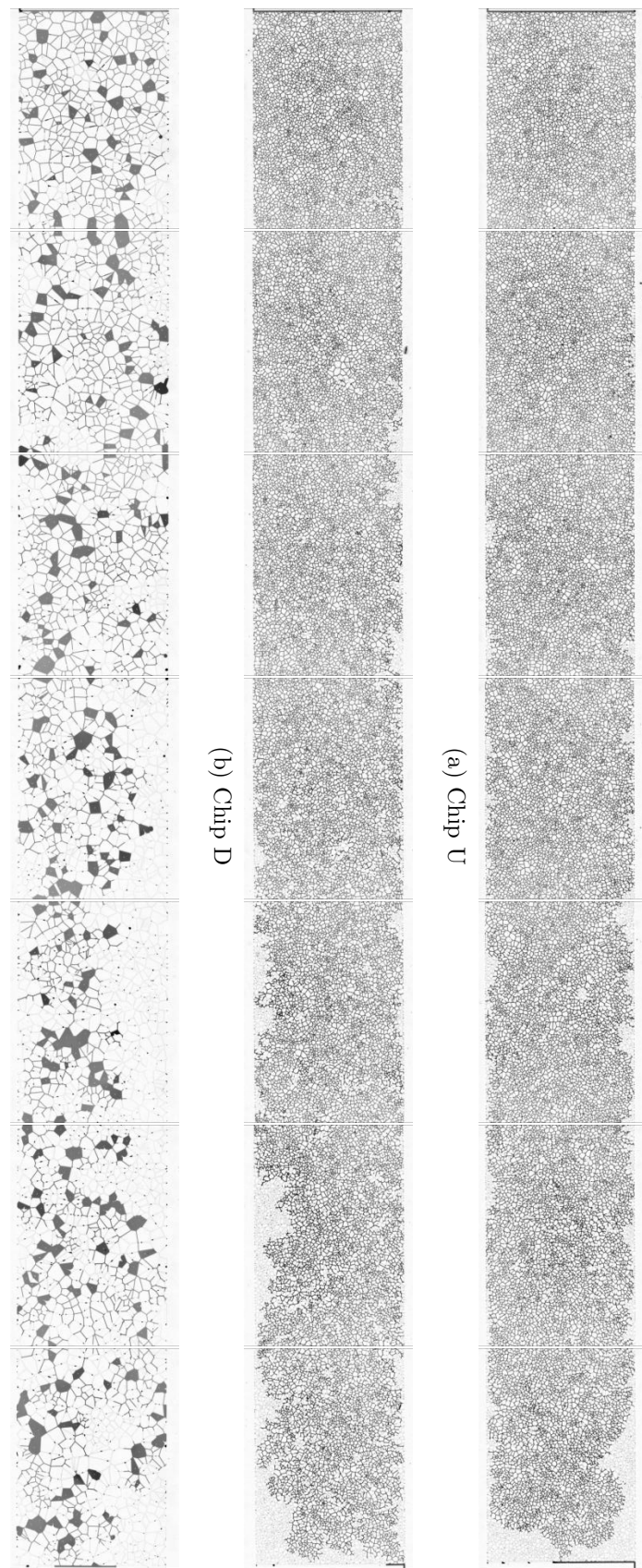
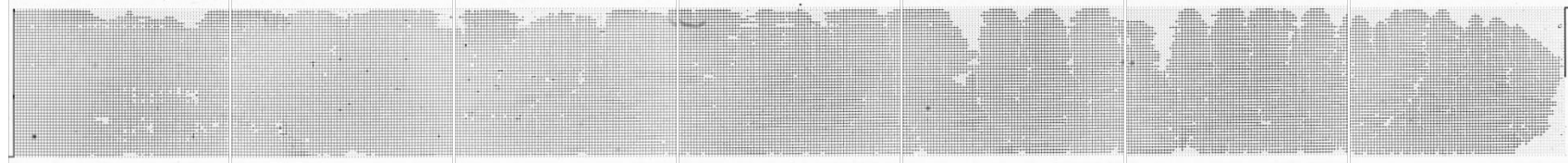
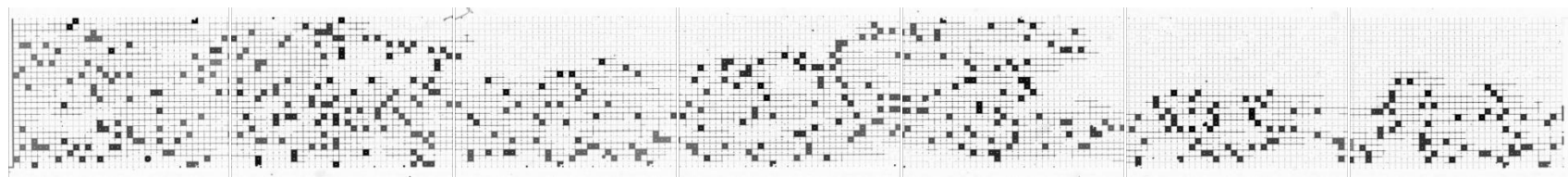


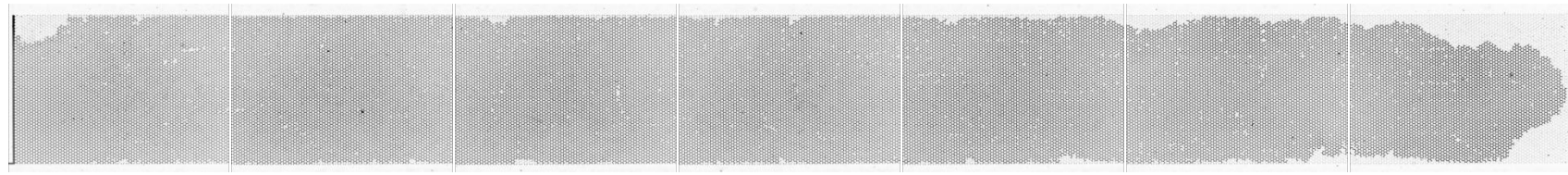
Figure 5.1: Breakthrough patterns of surfactant flooding for Chip U, D and V



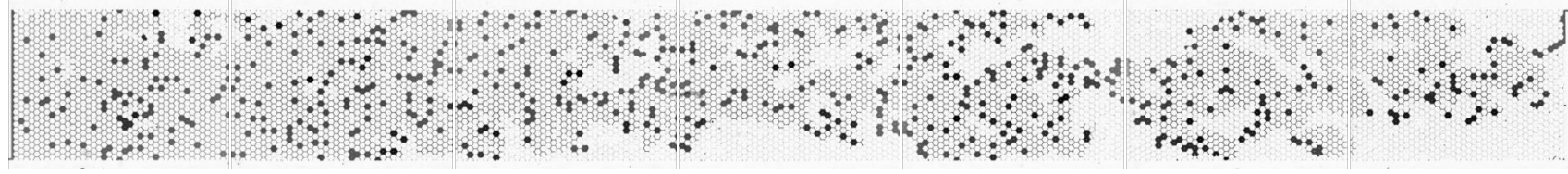
(a) Chip S



(b) Chip SV



(c) Chip H



(d) Chip HV

Figure 5.2: Breakthrough patterns of surfactant flooding for Chip S, SV, H and HV

Compared with Figure 4.1(c), the pattern of surfactant flooding of the Chip V in Figure 5.1(c) did not show obvious improvement. Using quantitative image analyses, we detected that with surfactant the water front still swept more area than in the water flooding. The average breakthrough time of this analog is 1256s, and the average breakthrough recovery factor is 73.4%, which is about 8% higher than that in water flooding.

Figure 5.2(a) showed that the surfactant dramatically improved the flooding process of Chip S, changing it from a water coning to a piston-like displacement. The average breakthrough time of this analog is 1723.7s, and the average breakthrough recovery factor is 90%.

In Figure 5.2(b), similar with Chip S, the surfactant restrained the water coning. Compared with water flooding, the oil was much better swept in surfactant flooding. The average breakthrough time of this analog is 1484.7s, and the average breakthrough recovery factor is 70.7%.

The sweep efficiency in water flooding of Chip H is already quite high. From Figure 5.2(c), the surfactant made the recovery factor even higher. The average breakthrough time of this analog is 2047.3s, and the average breakthrough recovery factor is 92.7%.

From Figure 5.2(d), visually, it is difficult to find an obvious difference between the breakthrough pattern of water and that of surfactant flooding in Chip HV. Like Chip V, quantitative difference was still detected, through image analyses. The average breakthrough time of this analog is 1741.7s, and the average breakthrough recovery factor is 75.3%, which is only 4% higher than that in water flooding.

### 5.1.2 Breakthrough time and recovery factor in water and surfactant flooding

Figure 5.3(a) shows that the surfactant dramatically reduced the breakthrough time. The trends for the seven analogs are similar, and they all show 1/3 to 1/2

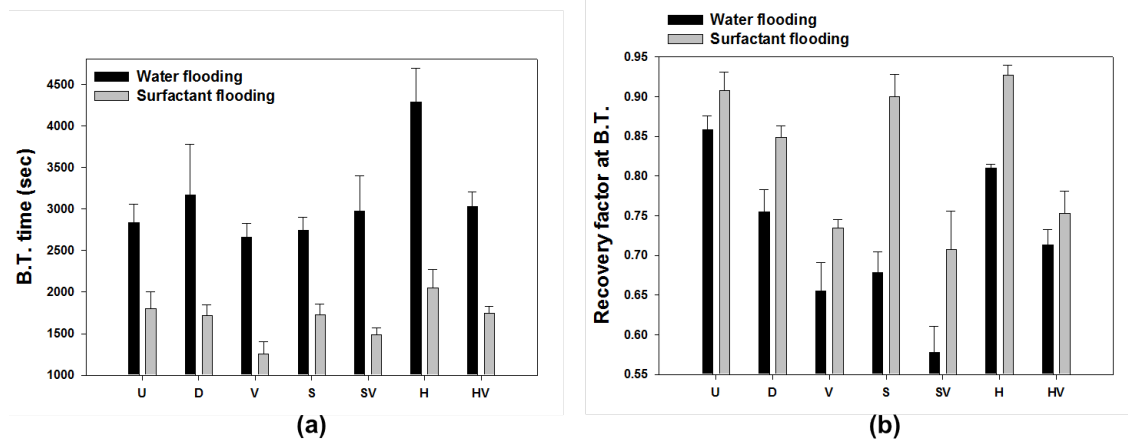


Figure 5.3: (a) Breakthrough times of water flooding (b) Recovery factors at breakthrough

reductions in breakthrough time.

One possible reason is that the reduction of IFT lowered the capillary pressure, which always acts against the frontal movement due to the hydrophobicity of the oil-wet  $\mu$ PMA (microfluidic micromodel). Based on a contact angle of 120 degrees and a radius of curvature of 6  $\mu$ m, the capillary pressure is 0.686 psi in waterflooding, and 0.086 psi in surfactant flooding. The compressed air provides a pressure of 1.5 psi, which means that the driving force is 0.814 psi for water flooding and 1.414 psi for surfactant flooding. This derivation is meant to be quantitative, but the nearly two times of difference in the driving pressure is on the same order of magnitude of the observed 1/2 to 1/3 reduction in the breakthrough time.

Additionally, in water flooding, the water front has more fingers and higher residual oil saturation. As a result, the relative permeability (or mobility) of water should be lower than in the surfactant flooding, where the front movement is mostly piston-like. This is also likely to increase the breakthrough time in water flooding relative to that in surfactant flooding.

From the Figure 5.3(b), the surfactant worked well for homogenous analogs than for heterogeneous ones. For Chip U, the breakthrough recovery increased from 85.9%

to 92.7%. This increase seems to be modest, but the water flooding recovery is already quite high. For Chip D, the breakthrough recovery increased from 75.5% to 84.9%. For Chip S, the breakthrough recovery increased from 67.9% to 90.7%, a dramatic enhancement. For Chip H, the breakthrough recovery increased from 81% to 92.7%, even higher than Chip U. Compared with these homogenous analogs, the improvements in heterogeneous analogs were consistently less. For Chip V, the breakthrough recovery increases from 65.5% to 73.4%. Note that this modest increase of 8% is over the already-low water flooding recovery, making it not as significant as the increases obtained previously. For Chip SV, the breakthrough recovery increased from 57.8% to 70.7%. Despite the 13% increase, the recovery at breakthrough is still low for surfactant flooding when compared to other chips. For Chip HV, the breakthrough recovery increased from 71.3% to 75.3%, which is almost negligible.

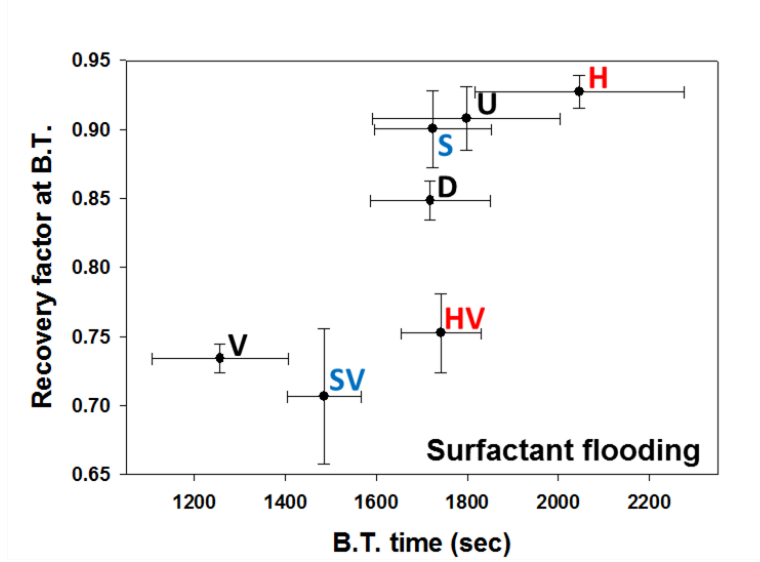


Figure 5.4: Recovery factor versus breakthrough time of surfactant flooding

In Figure 5.4, the average recovery factor measured at breakthrough is plotted as a function of average breakthrough time. There is a general trend that the increase of breakthrough time is correlated to the improvement in the recovery factor. However, just as in the water flooding cases, there are outliers (Chip SV and HV) that need to

be explained and analyzed.

## 5.2 Water Front Movement and Dynamics of Displacement

In this section, movies were taken at high magnification (100x) to illustrate the movement of water front in both water and surfactant flooding tests. Images at certain time intervals were extracted from the movies, and comparisons between water flooding and surfactant flooding were made.

From Figure 5.5, Chip U is a homogenous porous medium. By comparing the flooding pattern of water flooding to surfactant flooding, it is clear that in the surfactant flooding, the water front movement is more piston-like with less residual oil. Without surfactant, the front propagation is more fractal-like.

From Figure 5.6, the front movements in the Chip D with and without surfactant are similar to those in Chip U. The implemented pore size distribution caused more bypassing and oil trapping in the water flooding case, which decreased the recovery factor. Between 15s and 30s, consecutive images of water flooding show that the water front only moved along a few branches, whereas with lowered interfacial tension in surfactant flooding, the water front moved more uniformly in almost all directions, leaving very few residual oil behind.

From Figure 5.7, for Chip V, in water flooding, the water front prefers to go through vugs. The figures on the left show that the four vugs were filled sequentially. While the vugs were filled, withdrawal of the water from channels mentioned in the last chapter were observed. With surfactant, water front would still penetrate the porous medium through vugs. The withdrawals in the channels were still observed as the vugs were filled. The figures on the right shows that, at this particular location, more small channels were filled with surfactant. However, on the large scale, the improvement of surfactant is not as obvious as observed in Figure 5.1 and 5.2, as we have already learned from the recovery factor numbers

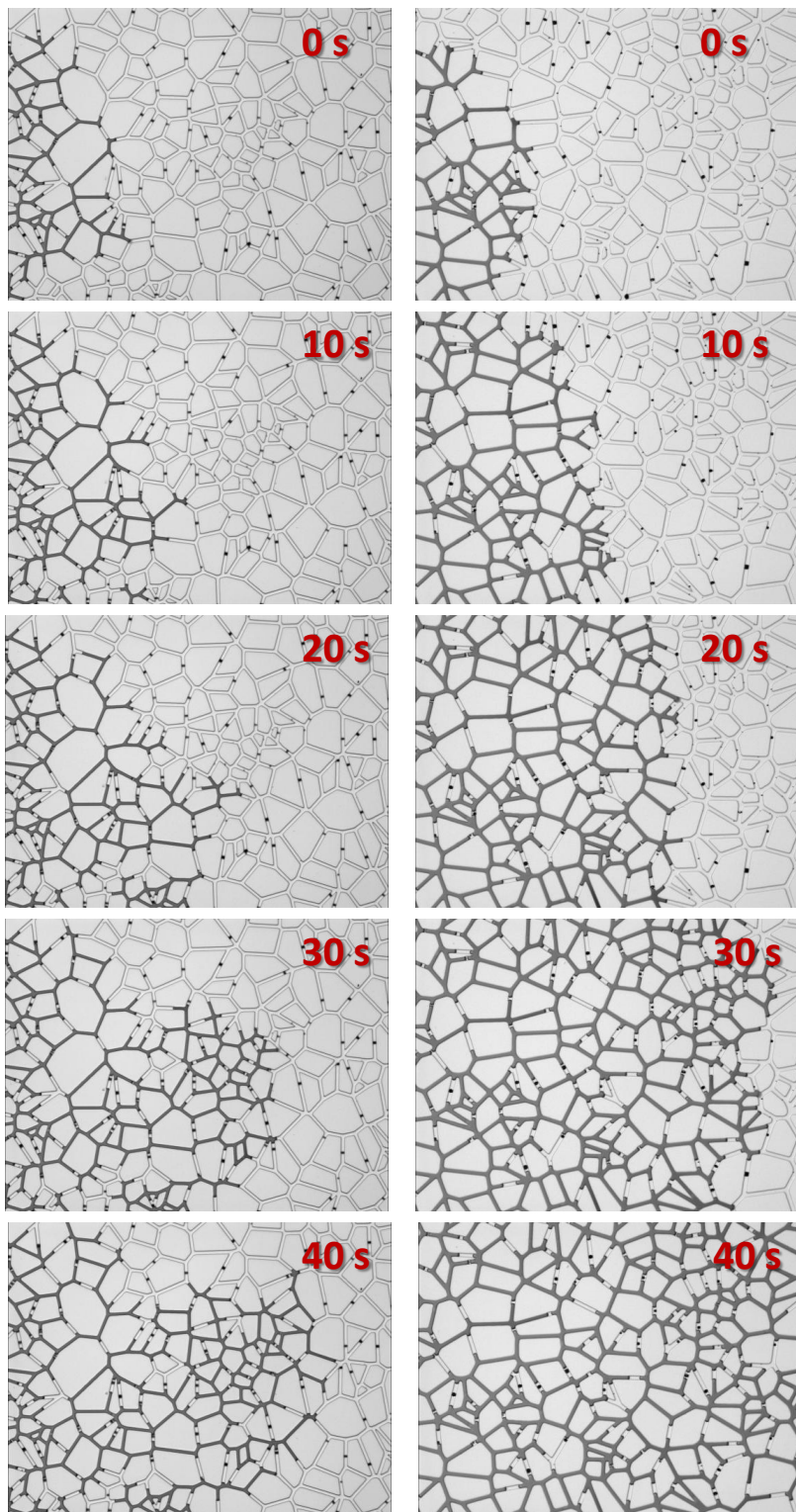


Figure 5.5: Magnified (100x) movement of water fronts in Chip U at 10s interval in water flooding (Left) and surfactant flooding (Right)

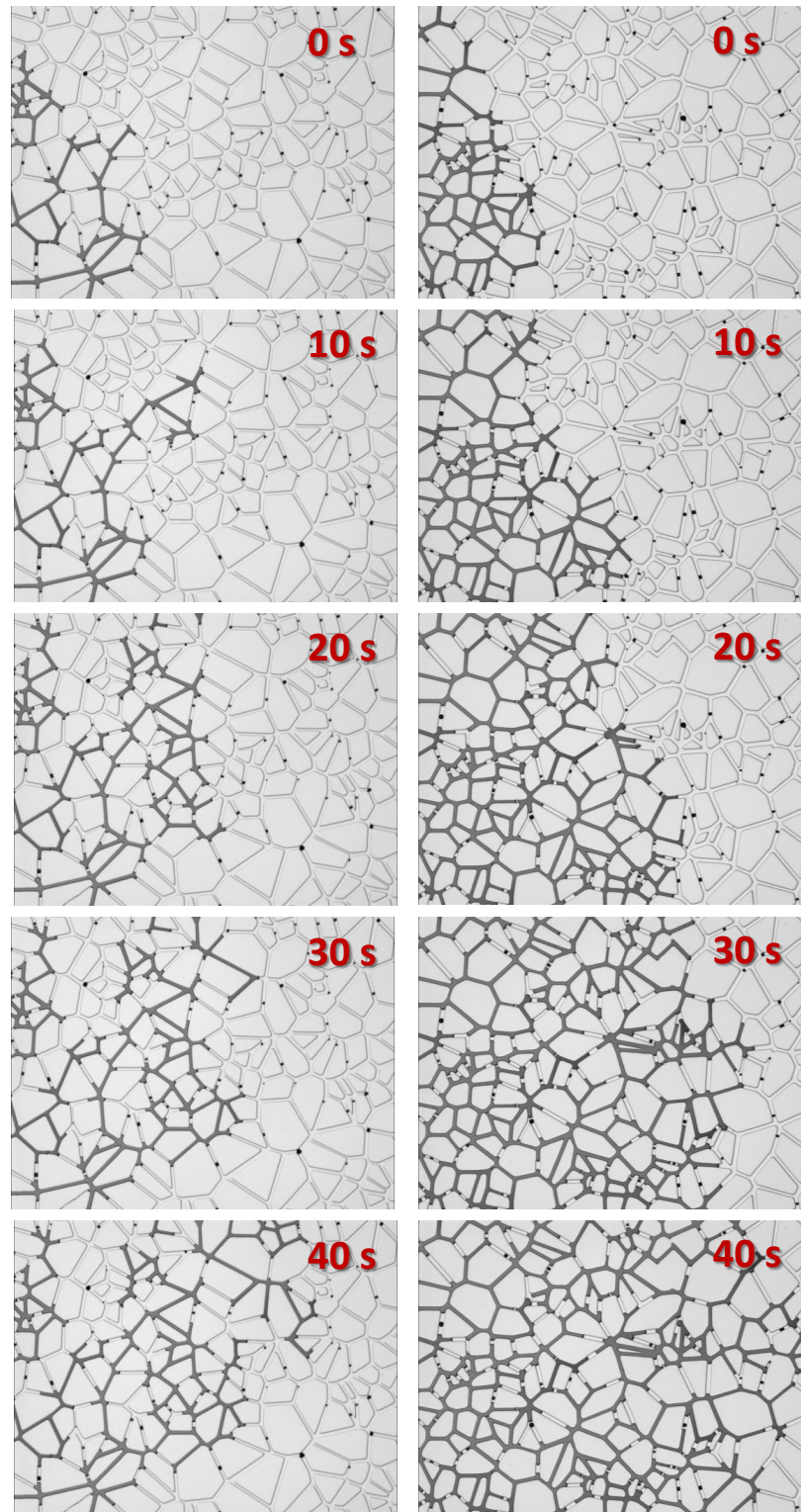


Figure 5.6: Magnified (100x) movement of water fronts in Chip D at 10s interval in water flooding (Left) and surfactant flooding (Right)

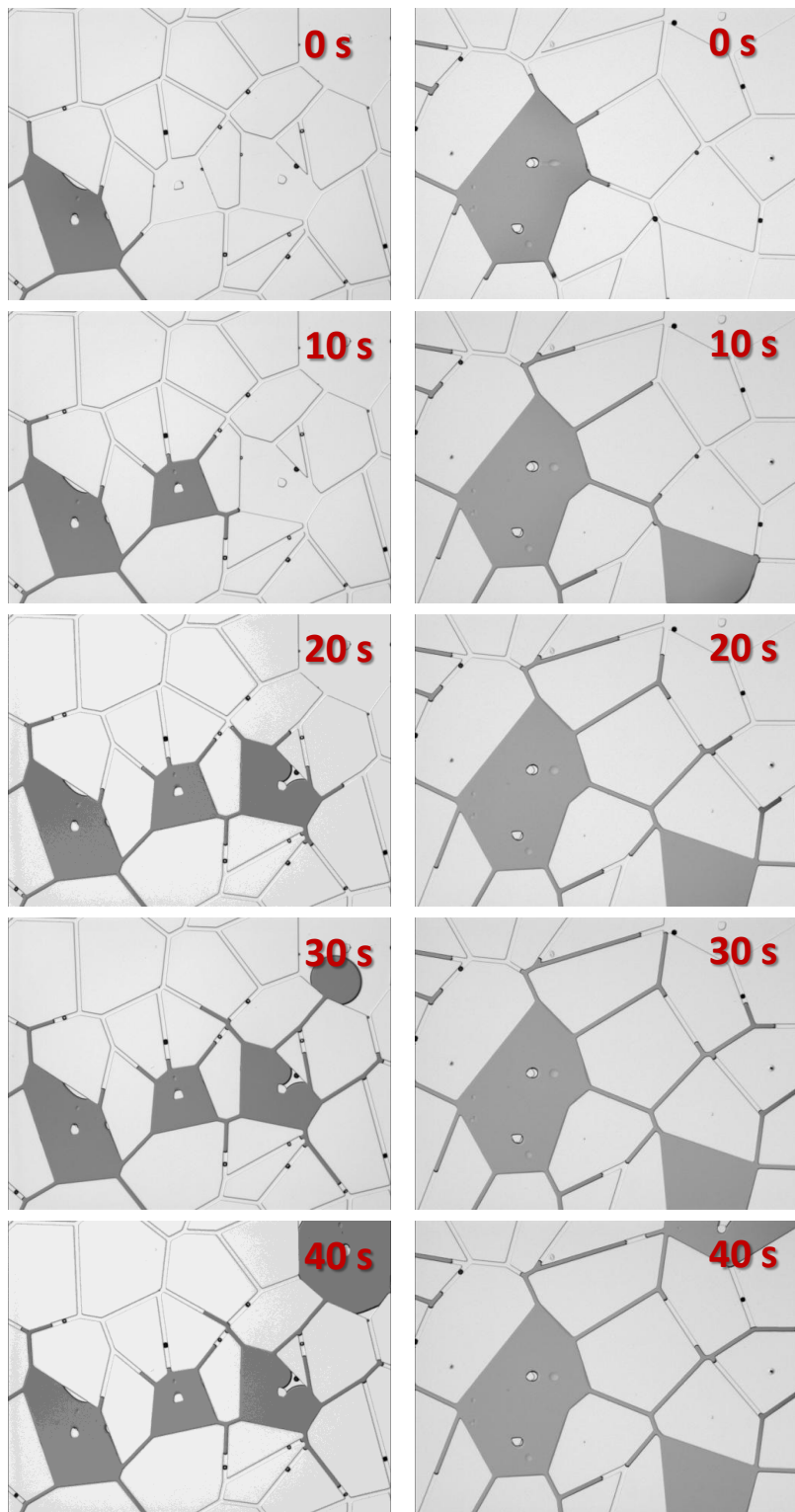


Figure 5.7: Magnified (100x) movement of water fronts in Chip V at 10s interval in water flooding (Left) and surfactant flooding (Right)

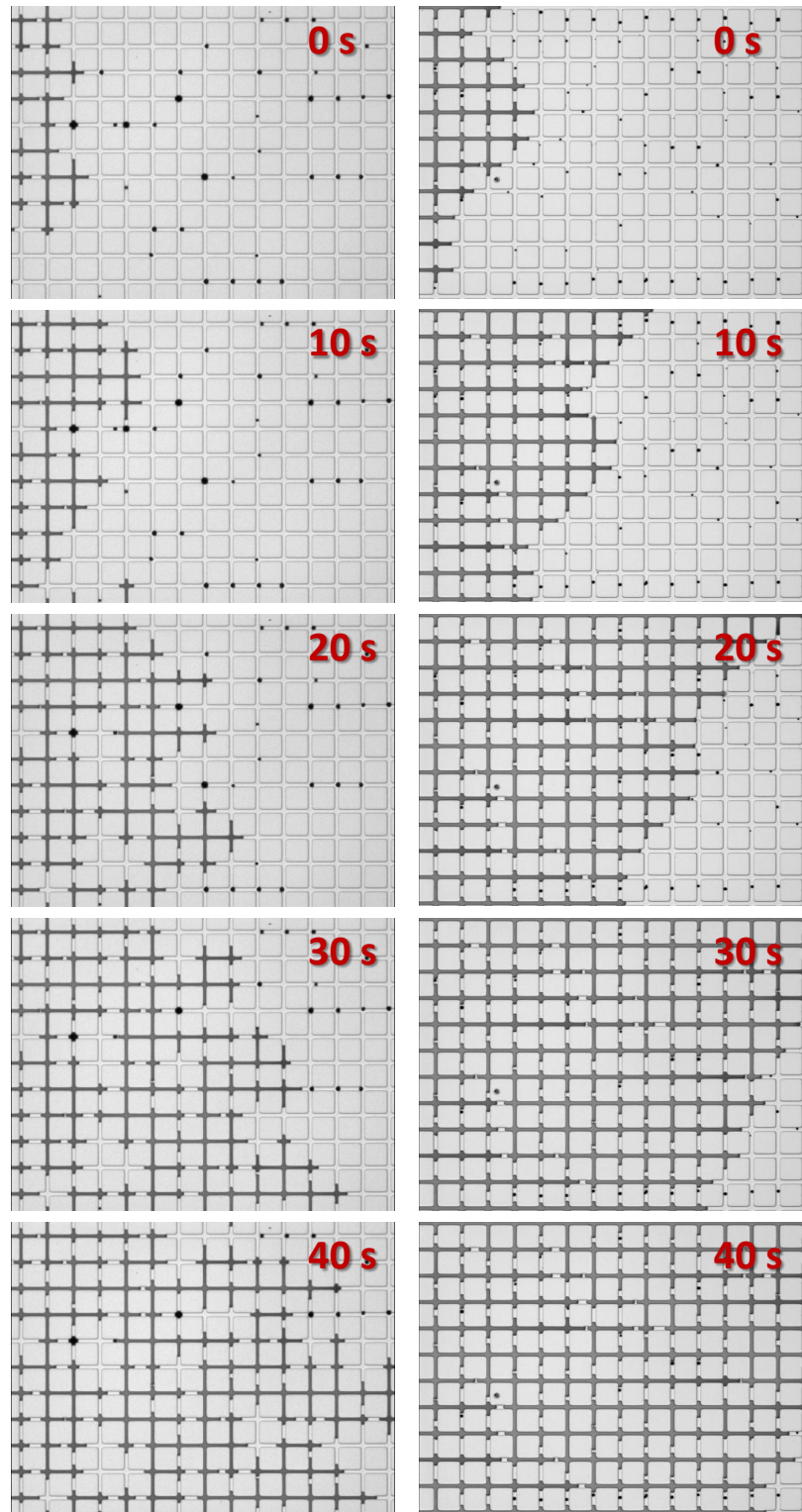


Figure 5.8: Magnified (100x) movement of water fronts in Chip S at 10s interval in water flooding (Left) and surfactant flooding (Right)

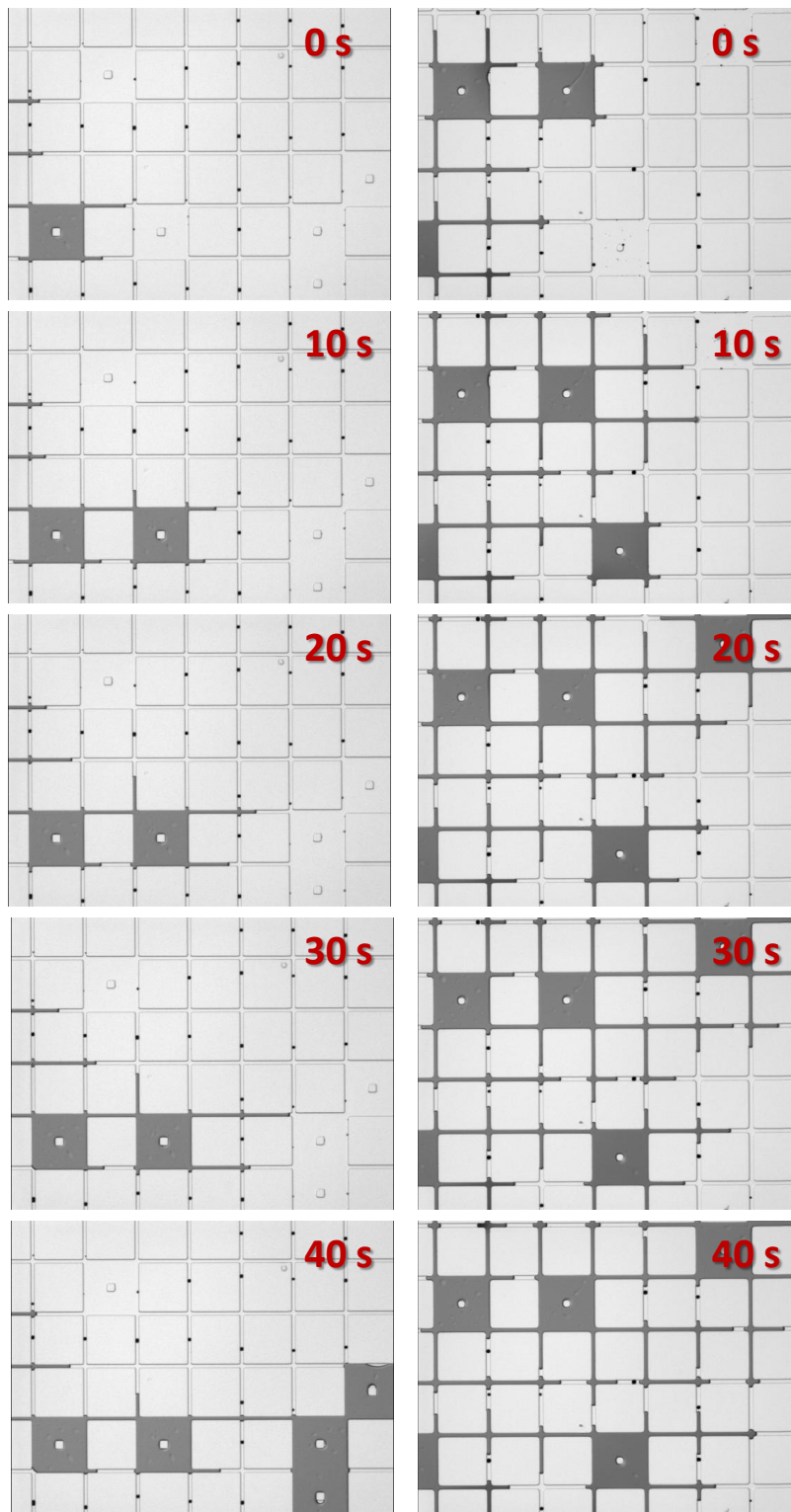


Figure 5.9: Magnified (100x) movement of water fronts in Chip SV at 10s interval in water flooding (Left) and surfactant flooding (Right)

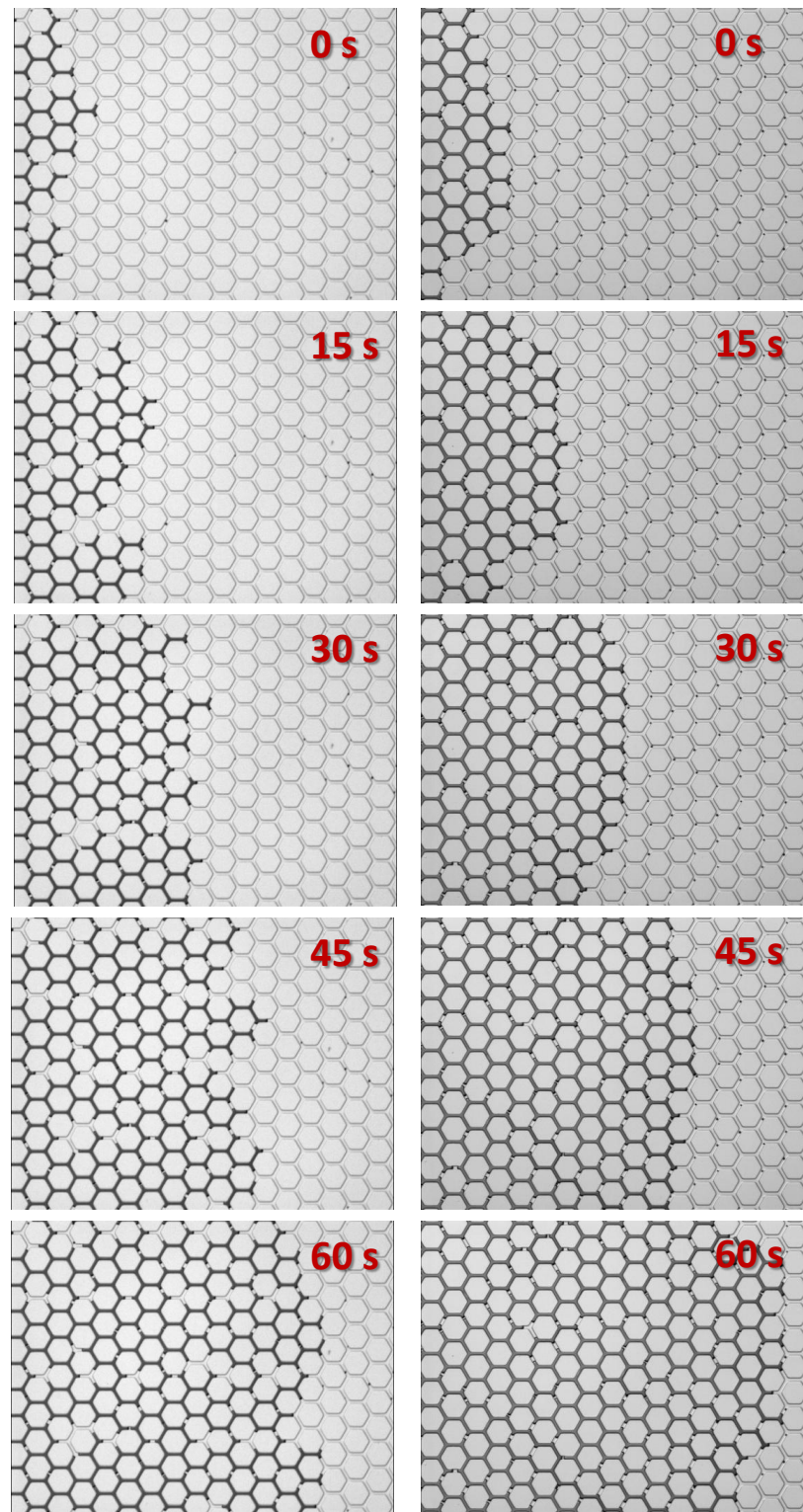


Figure 5.10: Magnified (100x) movement of water fronts in Chip H at 10s interval in water flooding (Left) and surfactant flooding (Right)

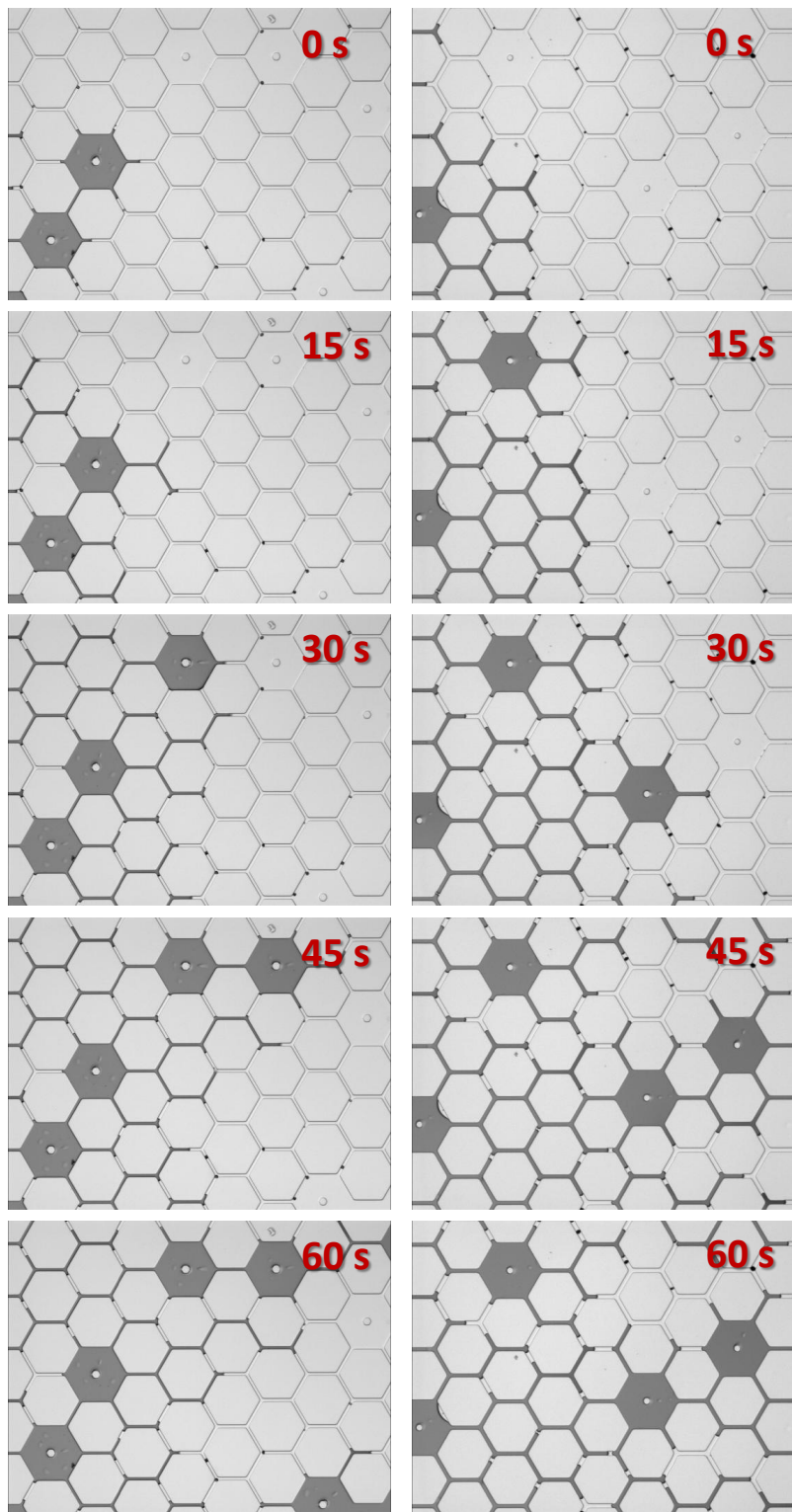


Figure 5.11: Magnified (100x) movement of water fronts in Chip SH at 10s interval in water flooding (Left) and surfactant flooding (Right)

From Figure 5.8, for Chip S, surfactant was very effective in suppressing the horizontal movement of the water front. As mentioned in the last chapter, in water flooding, the water front moved evenly in all directions at the first four locations and became in favor of the horizontal direction at the last three locations. In this figure, a sequence of images taken at positions 2 is chosen to show the water front in water flooding. While at this location the propagation of the front is not cone-like, there are significant residual oil left after the water front passed by. In the figures on the right, with surfactant, water front moved like a piston without branching, and few residual oil were left behind at this location. There was no cone-shaped breakthrough in the last three positions, either.

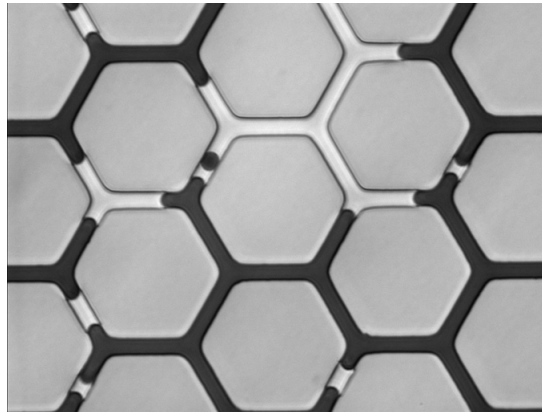
From Figure 5.9, for Chip SV, it may be observed that with surfactant, although water still preferred to go through the vugs, there were more small channels filled than the case without surfactant .

From Figure 5.10, in the Chip H, the water flooding process was already very stable with good displacement efficiency. Although some fingers were observed (between 30s and 45s), but the fingers can catch up with the front and there was no quick breakthrough for this geometry and not much residual oil was trapped and left behind. In the surfactant flooding, the water front appeared to be even more uniform and piston-like. Even small fingers were not spotted.

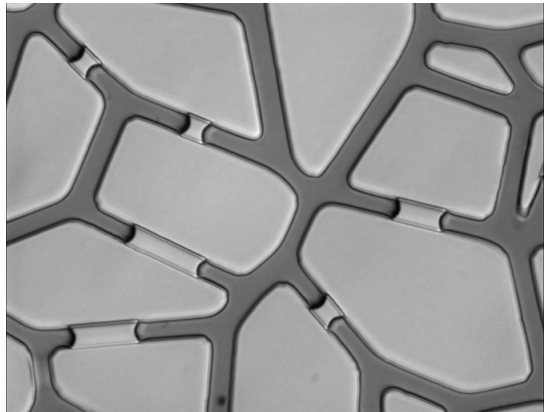
From Figure 5.11, it may be observed that smaller channels are more evenly filled when surfactant is present. Same as other vuggy geometries, water withdrawal from smaller channels were observed as the vugs were filled.

### 5.3 Examination of Contact Angle for Potential Wettability Alteration

To find out whether surfactant had altered the wettability of the porous medium, 400x images were taken after the water and surfactant flooding tests. From the contact angles shown in Figure 5.12, there is no sign of wettability alternation on the PDMS wall. However, it must be pointed out that this does not rule out the



(a) Contact angle after water flooding is  $121.7^\circ \pm 3^\circ$



(b) Contact angle after surfactant flooding is  $120.7^\circ \pm 2.2^\circ$

Figure 5.12: 400x magnification image after water flooding and surfactant flooding

possibility that EA would cause wettability alternation. Wettability alteration is a slow process and the duration of our experiments may not be sufficient for it to happen. In real reservoirs, interaction of EA with rock should also be different from that in our micromodels.

#### 5.4 Real Time Progression of Water and Surfactant Flooding

In this section, the progression of water flooding and surfactant flooding in our  $\mu$ PMA is presented in the form of injected PV versus time. For each chip, both water flooding and surfactant flooding have three times lines, respectively, from the three repetitions. Figure 5.13 shows that the injection of the first PV is usually the slowest. As breakthrough took place, and the subsequent two PVs can be quickly reached. In homogenous analogs, the decrease in time after breakthrough was more obvious than in heterogeneous analogs, because of the higher recovery factor at breakthrough, leading to the higher relative permeability of water.

The surfactant significantly reduced the overall time needed. The trend in the overall times with geometries is similar with the trend in the breakthrough times with geometries. The homogenous analogs generally have lower times to reach each PV point than heterogeneous analogs except Chip H and Chip HV.

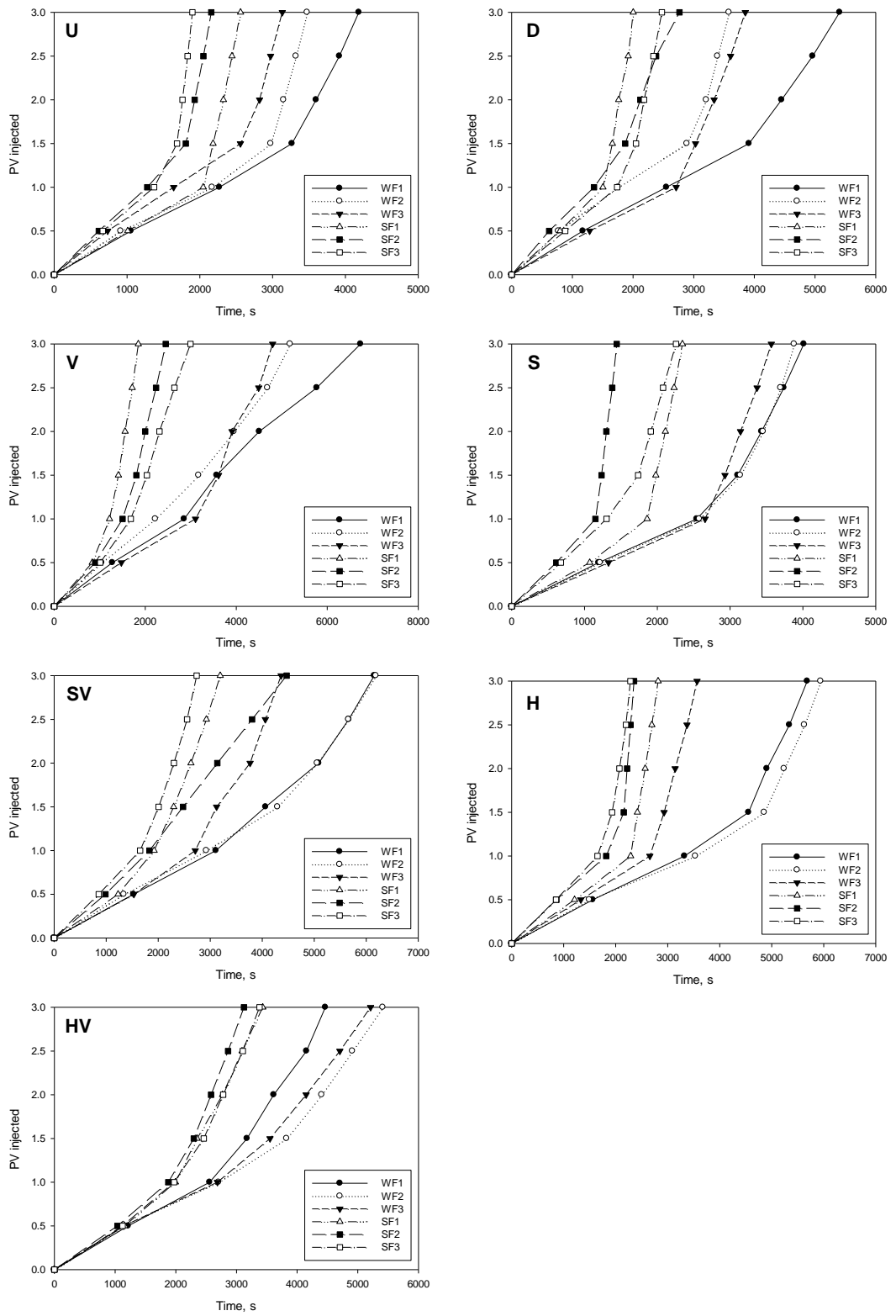


Figure 5.13: Progression of water and surfactant flooding for each  $\mu$ PMA

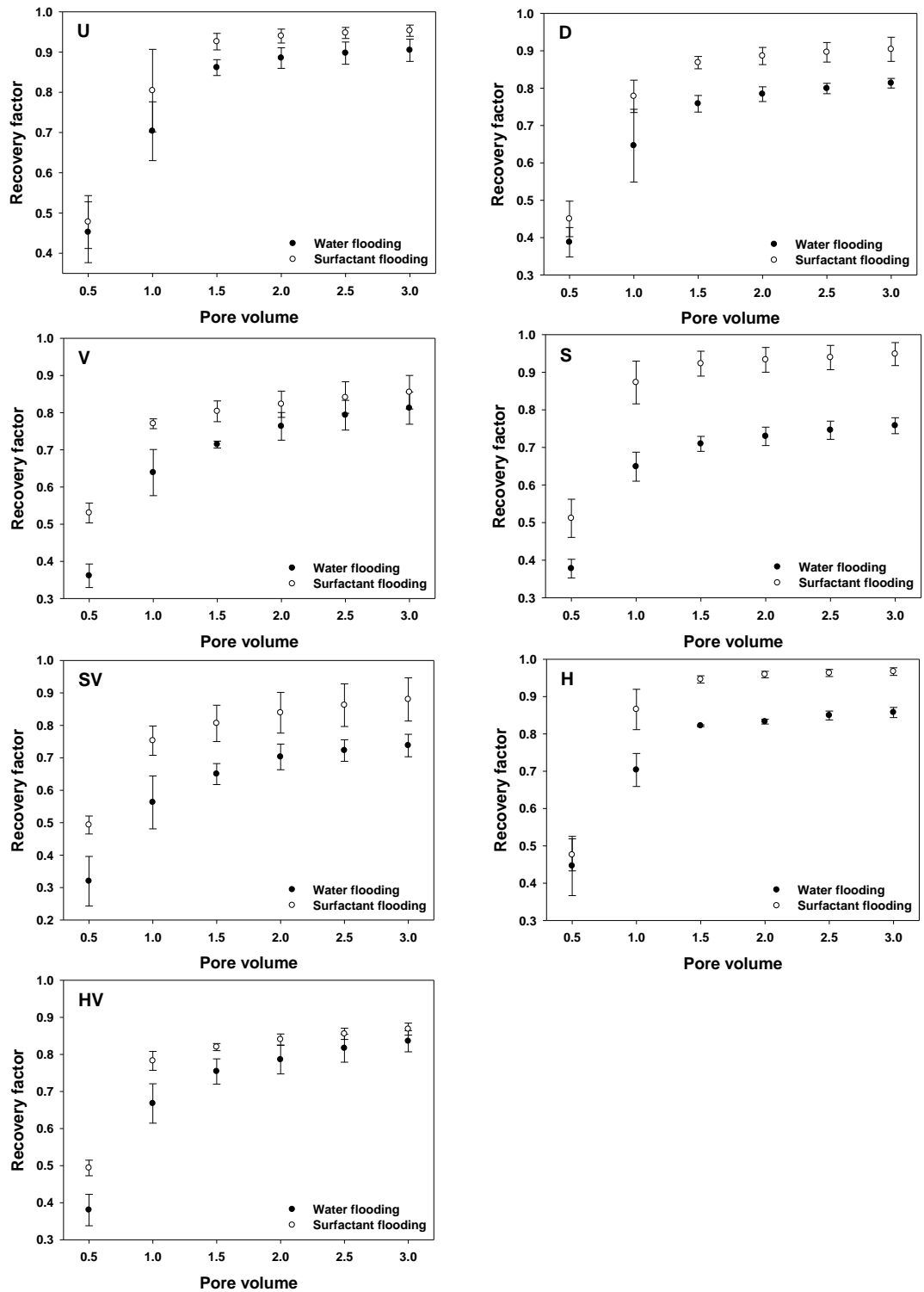


Figure 5.14: Recovery factor of each  $\mu$ PMA in water and surfactant flooding

## 5.5 Enhanced Oil Recovery of Surfactant Flooding at Each Stages

In this section, the recovery factor of water flooding and surfactant flooding at each 0.5 PV injected are compared. Figure 5.14 shows that the trend in the recovery factor at other times with geometries is similar with trend in the recovery factor at breakthrough with geometries. The homogenous analogs generally have higher enhancement over time than heterogeneous analogs except Chip SV.

For Chip U, the recovery factor at 3 PV injected increased from 90.5% to 95.3%. This 4.8% of increase is quite notable, as the water flooding recovery is already quite high. For Chip D, the recovery factor at 3 PV injected increased from 81.3% to 90.4%. For Chip S, the recovery factor at 3 PV injected increased from 75.8% to 94.8%. For Chip H, the recovery factor at 3 PV injected increased from 85.7% to 96.7%.

For Chip V, the recovery factor at 3 PV injected increased from 81.2% to 85.5%, only 4.3% increase. For Chip SV, the recovery factor at 3 PV injected increases from 73.9% to 88%, a quite good enhancement in the vugs family. For Chip HV, the recovery factor at 3 PV injected increased from 83.6% to 86.8%, which is, again, a negligible improvement.

## 5.6 Influence of Capillary Number

Because the contact angle was not modified in our experiments, of all the dimensionless quantities that control the displacement dynamics, only the capillary number was modified. In this section, the capillary numbers of all tests are calculated, and the recovery factors at breakthrough and 3 PV injected are plotted versus the capillary numbers to examine the relationship between these two parameters.

Table 5.1 shows that surfactant had increased the capillary for about 10 times and the increase in the recovery factor ranged from 4% to 20%. The results were shown in the Table 5.1.

Table 5.1: Capillary number (Ca No.) and recovery factor (RF) of each  $\mu$ PMA at breakthrough (B.T.) and 3PV

	Water Flooding			Water Flooding		
	Ca No.	RF at B.T.	RF at 3PV	Ca No.	RF at B.T.	RF at 3PV
U	3.59E-06	85.88%	90.45%	5.52E-05	90.81%	95.31%
D	3.28E-06	75.45%	81.31%	5.75E-05	84.86%	90.38%
V	3.84E-06	65.51%	81.22%	7.92E-05	73.43%	85.49%
S	3.72E-06	67.88%	75.77%	5.74E-05	90.03%	94.83%
SV	3.46E-06	57.81%	73.78%	6.65E-05	70.68%	88.00%
H	2.39E-06	81.01%	85.74%	4.85E-05	92.75%	96.69%
HV	3.36E-06	71.34%	83.56%	5.66E-05	75.25%	86.80%

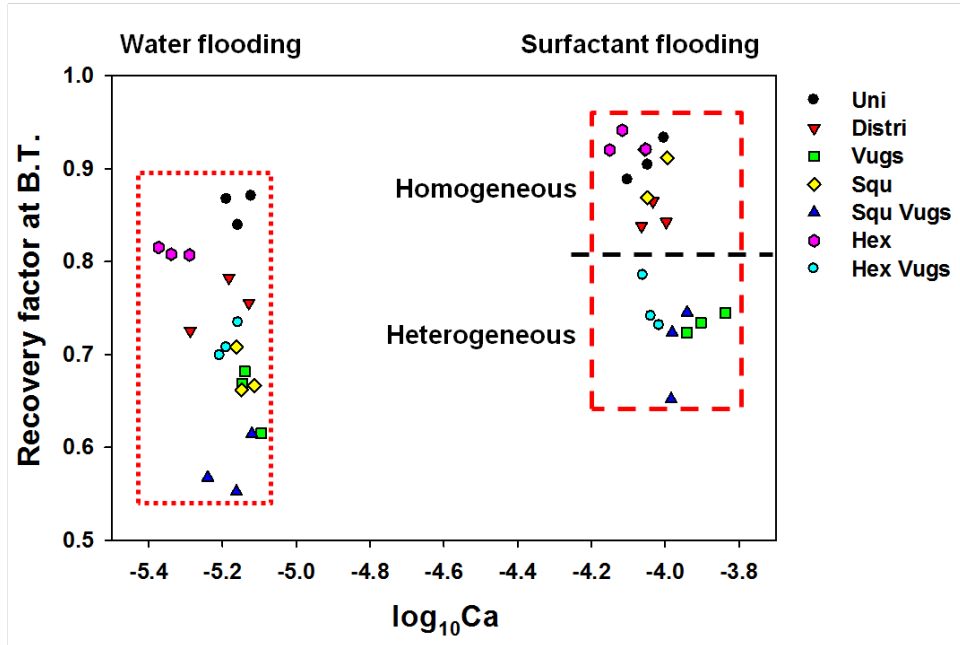


Figure 5.15: Recovery factor at breakthrough versus  $\log_{10}\text{Ca}$  of each  $\mu$ PMA in water and surfactant flooding

From this Figure 5.15, for water flooding, the capillary number were about  $3 \times 10^{-6}$ .

All the heterogeneous and the homogenous square analogs have lower recovery than homogenous analogs except the square one.

With addition of surfactant, the capillary number increased to about  $6 \times 10^{-5}$ . This increase not only came from the nearly 10 fold reduction in the surface tension, but also from the higher speed of water phase penetration likely caused by the reduction of capillary pressure as reflected by the reduced breakthrough time. This figure shows

clearly that increasing capillary number improves the recovery factor at breakthrough.

As to the effect of geometry, the recovery factors of seven analogs can be roughly divided into two zones. The recovery factors of homogenous analogs usually fall into the upper zone (except Chip S) and those of heterogeneous analogs fall into the lower. The division is close to the recovery recovery factor of 75% for water flooding, and 80% for surfactant flooding.

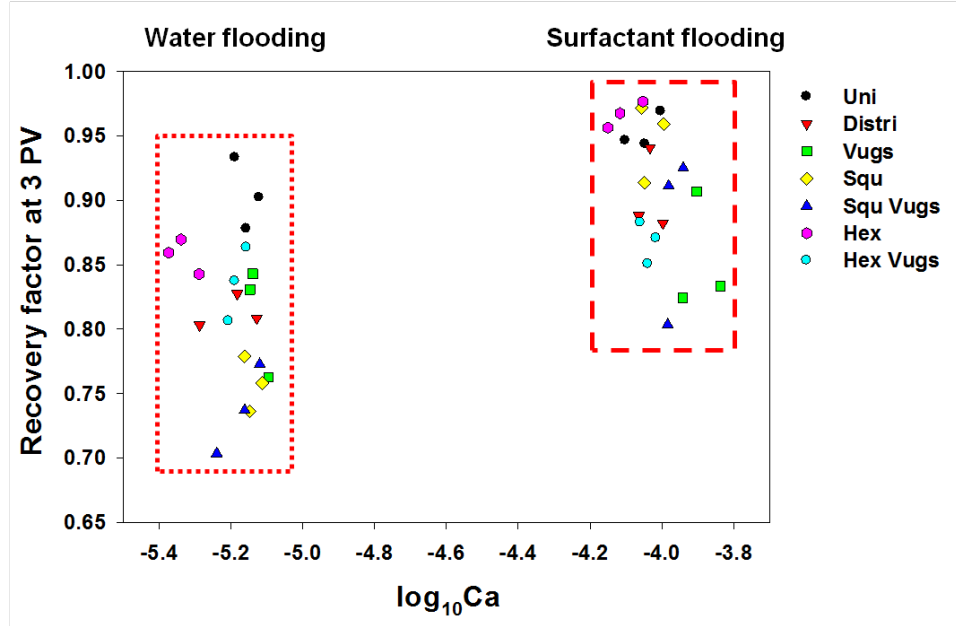


Figure 5.16: Recovery factor at 3 PV injected versus  $\log_{10} \text{Ca}$  of each  $\mu\text{PMA}$  in water and surfactant flooding

Figure 5.16 shows that the recovery factors at 3 PV of water flooding ranged from 70% to 94%. Among them, most values are between 80% and 90%. Chips U and H, two homogenous geometries, have the highest recovery factor, and then followed by the two heterogeneous geometries, Chip V and HV. Chip D and SV are lower than the last two vugs geometry. The recovery of Chip S is the lowest.

In surfactant flooding, all the recovery factors were above 80%. Homogenous geometries still in general have higher recovery factors than heterogeneous geometries. But, unlike The recovery factors at breakthrough, there is some overlap between the recover factors of homogeneous geometries, and those of heterogeneous geometries.



## CHAPTER 6

### CONCLUSIONS AND RECOMMENDATION

In this chapter, based on the experiments results and discussion, we draw conclusions of this research, and gave some suggestions for the future work.

#### **6.1 Technical Advancements**

In this research the pore geometries of  $\mu$ PMA were more complex and better controlled than those used previously. All  $\mu$ PMAs have similar porosity of 19%. Although the measured permeability of our micromodels are lower than LB simulations, they are still close to the designed target of about 200 md. These micromodels have a shape that more resembles the core flooding geometry than those in (Wu et al., 2012). And they contain much more grains to make them meaningful as porous media analogs. They also have improved inlet and outlet designs.

We showed that the wettability of our microfluidic micromodel can be modified by silane coating to provide a uniformly oil-wet condition. This is verified by microscopy.

#### **6.2 Conclusion**

By this research, these conclusions are achieved:

- In both water and surfactant flooding, pore size distribution structure lowers the recovery factor.
- Heterogeneous networks (vugs) always have negative effect on recovery factors in water flooding.
- Higher CN seems to lower the recovery factor. However this conclusion must be examined carefully as our square geometry is not the same as that used previously.

- 0.5 wt% EA solution can effectively modified the water front, reduce the breakthrough time and increase the recovery factor at breakthrough from 4% to 23%.

The final recovery at 3 PV injected was enhanced from 4% to 20%.

- In heterogeneous analogs, surfactant did not perform as well as in homogenous analogs.
- In the surfactant flooding by EA solutions, we did not observed any sign of wettability alternation in our PDMS micromodel. The only dimensionless variable that is changed by surfactant is the capillary number. Increasing of capillary number leads to an increasing of recovery factor.

### 6.3 Limitations

Through flooding experiments carried out in our micromodels, we successfully visualized the dynamic of water-oil displacement with and without surfactant. These experiments supply important information on how pore geometry affects the displacement efficiency, and are especially useful for IOR/EOR studies targeting oil-wet, highly heterogeneous carbonate reservoirs. However, quantitatively, although our porous media analogs were designed to have the similar porosity and permeability of real cores, the water flooding recovery factor is higher than those in core flooding tests which usually ranges of 40% to 60%(Alamdari et al., 2012; Mohan, 2009), and certainly higher than real field cases. This is caused by the tiny scale of our microfluidic micromodel and relatively simplistic representation of the pore geometry (compared with real rock) using variations of 2D Voronoi diagrams.

Another limitation is that our micromodel is only operable at low pressure and room temperature, because the PDMS is soft, and the oxygen plasma bonding will fail when the pressure is higher than 30-50 psi (McDonald et al., 2000). What's more, the incompatibility of PDMS with certain organic solvents (dyes, light components in crude oil) limits the use of crude oil and makes confocal microscopic study difficult.

There are some polymers proved to be good substitute for PDMS, for example, Thermoset Polyester (TPE), Polyurethane Methacrylate (PUMA) and Norland Adhesive 81 (NOV81)(Sollier et al., 2011). Among them, the TPE has the best hardness, solvent compatibility and the relatively low cost (Sollier et al., 2011). Several researchers used TPE for microfluidic studies (Fiorini et al., 2004; Kim et al., 2011; Vickers et al., 2007). It is a good candidate for future micromodel studies and applications in oil and gas industry.

#### 6.4 Future Works and Recommendation

These points are suggested for future studies:

- Some other surfactants, which can lower IFT to 0.1 dynes/cm level, should be tested to achieve higher capillary numbers.
- New pore geometry should be designed with more complexity. For example, we may adding the pore and throat structure in Chip D.
- New materials with better pressure and temperature tolerance and compatibility with organic solvents should be tried in the future. TPE is a good option because it's rigid and relatively easy to make.
- The relative permeability of our microfluidic micromodel should be measured by time lapse interval photography. The relative permeability can be calculate by the relationship between saturation change, flow rate and pressure drop.
- Better characterization of wetting and non-wetting phase distributions should be done in the future using confocal microscope. Also fluorescence microscopy can be used to visualize nano-particle dispersion like gel or colloid in our micromodel.



## REFERENCES CITED

- C. Agbalaka, A. Dandekar, S. Patil, S. Khataniar, and J. Hemsath. The Effect of Wettability on Oil Recovery: A Review. *Proceedings of SPE Asia Pacific Oil and Gas Conference and Exhibition*, Oct. 2008. doi: 10.2118/114496-MS.
- B. B. Alamdari, M. Kiani, and H. Kazemi. Experimental and Numerical Simulation of Surfactant-Assisted Oil Recovery in Tight Fractured Carbonate Reservoir Cores. *SPE Improved Oil Recovery Symposium*, (2000):1–14, 2012. doi: 10.2118/153902-MS.
- A. J. Alshehri, U. Stanford, S. Aramco, E. Sagatov, and A. R. Kovscek. Pore-Level Mechanics of Forced and Spontaneous Imbibition of Aqueous Surfactant Solutions in Fractured Porous Media. In *SPE Annual Technical Conference and Exhibition*, number 2, New Orleans, Louisiana, USA, 2009. Society of Petroleum Engineers. doi: 10.2118/124946-MS.
- W. G. Anderson. Wettability Literature Survey-Part 6: The Effects of Wettability on Waterflooding. *Journal of Petroleum Technology*, Volume 39,(december):1605–1622, 1987.
- H. Asar, A. Satman, and S. Saner. Laboratory Miscible Displacement Study in Arabian Carbonate Cores. In *Middle East Oil Show*, Bahrain, 1987.
- T. Austad. A Review of Retention Mechanisms of Ethoxylated Sulfonates in Reservoir Cores. In *Proceedings of SPE International Symposium on Oilfield Chemistry*, New Orleans, Louisiana, Mar. 1993. Society of Petroleum Engineers. doi: 10.2523/25174-MS.
- M. Bataweel, H. Nasr-El-Din, and D. Schechter. Fluid Flow Characterization of Chemical EOR Flooding: A Computerized Tomography (CT) Scan Study. *SPE/DGS Saudi Arabia . . .*, (1990):1–15, 2011.
- J. Bruining, B.-L. Nguyen, and E. Slob. A New Method for Saturation Measurements in Core Flooding Experiments. In *Proceedings of SPE Annual Technical Conference and Exhibition*, New Orleans, Louisiana, Sept. 1998. Society of Petroleum Engineers. ISBN 9781555631567. doi: 10.2118/49299-MS.
- M. Buchgraber, T. Clemens, L. Castanier, and A. Kovscek. A Microvisual Study of the Displacement of Viscous Oil by Polymer Solutions. *SPE Reservoir Evaluation & Engineering*, Volume 14,(June):pp. 269–280, Mar. 2011. doi: 10.2118/25174-MS.

- A. Dehghan and R. Kharrat. Studying the Effects of Pore Geometry, Wettability and Co-Solvent Types on the Efficiency of Solvent Flooding to Heavy Oil in Five-Spot Models. In *SPE Asia Pacific Oil and Gas Conference and Exhibition*, Jakarta, Indonesia, 2009. Society of Petroleum Engineers.
- M. Enwere. NMR Imaging for Water/Oil Displacement in Cores Under Viscous-Capillary Force Control. In *SPE/DOE Enhanced Oil Recovery ...*, Tulsa, Oklahoma, 1992. Society of Petroleum Engineers.
- J. Farle and D. Redline. Evaluation of Flood Water Quality in the West Montalvo Field. *Journal of Petroleum Technology*, Volume 20,:683–687, 1968. doi: 10.2118/1985-PA.
- G. S. Fiorini, R. M. Lorenz, J. S. Kuo, and D. T. Chiu. Rapid Prototyping of Thermoset Polyester Microfluidic Devices. *Analytical Chemistry*, 76(16):4697–4704, Aug. 2004. ISSN 0003-2700. doi: 10.1021/ac0498922.
- D. George, O. Hayat, and A. Kovscek. A microvisual study of solution-gas-drive mechanisms in viscous oils. *Journal of Petroleum Science and Engineering*, 46 (1-2):101–119, Feb. 2005. ISSN 09204105. doi: 10.1016/j.petrol.2004.08.003.
- T. Gervais, J. El-Ali, A. Günther, and K. F. Jensen. Flow-induced deformation of shallow microfluidic channels. *Lab on a chip*, 6(4):500–7, Apr. 2006. ISSN 1473-0197. doi: 10.1039/b513524a.
- N. S. K. Gunda, B. Bera, N. K. Karadimitriou, S. K. Mitra, and S. M. Hassanzadeh. Reservoir-on-a-chip (ROC): a new paradigm in reservoir engineering. *Lab on a chip*, 11(22):3785–92, Nov. 2011. ISSN 1473-0189. doi: 10.1039/c1lc20556k.
- B. S. Hardy, K. Uechi, J. Zhen, and H. Pirouz Kavehpour. The deformation of flexible PDMS microchannels under a pressure driven flow. *Lab on a chip*, 9(7):935–8, Apr. 2009. ISSN 1473-0197. doi: 10.1039/b813061b.
- R. I. Hawes, R. A. Dawe, and R. N. Evans. The Release of Solution Gas from Waterflood Residual Oil. *SPE Journal*, Volume 2,:379–288, 1997.
- F. Javadpour and D. Fisher. Nanotechnology-Based Micromodels and New Image Analysis to Study Transport in Porous Media. *Journal of Canadian Petroleum Technology*, 47(2), Feb. 2008. ISSN 0021-9487. doi: 10.2118/08-02-30.
- J.-y. Kim, A. J. DeMello, S.-I. Chang, J. Hong, and D. O'Hare. Thermoset polyester droplet-based microfluidic devices for high frequency generation. *Lab on a chip*, 11 (23):4108–12, Dec. 2011. ISSN 1473-0189. doi: 10.1039/c1lc20603f.

- A. Kovscek, G.-Q. Tang, and C. Radke. Verification of Roof snap off as a foam-generation mechanism in porous media at steady state. *Colloids and Surfaces A: Physicochemical and Engineering Aspects*, 302(1-3):251–260, July 2007. ISSN 09277757. doi: 10.1016/j.colsurfa.2007.02.035.
- L. Lake. *Enhanced Oil Recovery*. Prentice Hall, Englewood Cliffs, New Jersey, 1989.
- R. Lenormand. Liquids in porous media. *Journal of Physics: Condensed Matter*, 79, 1990.
- R. Lenormand and C. Zarcone. Two-phase flow experiments in a two-dimensional permeable medium. *Pch Physicochemical Hydrodynamics*, 6(5-6):497–506, 1985.
- D. Levitt, A. Jackson, and C. Heinson. Identification and evaluation of high-performance EOR surfactants. In *SPE/DOE Symposium* . . ., Tulsa, Oklahoma, USA, 2006. Society of Petroleum Engineers.
- J. C. McDonald, D. C. Duffy, J. R. Anderson, D. T. Chiu, H. K. Wu, O. J. A. Schueller, and G. M. Whitesides. Fabrication of microfluidic systems in poly(dimethylsiloxane). *Electrophoresis*, 21(1):27–40, 2000. ISSN 01730835. doi: 10.1002/(SICI)1522-2683(20000101)21:1<27::AID-ELPS27>3.0.CO;2-C.
- K. Mohan. Alkaline Surfactant Flooding for Tight Carbonate Reservoirs. *Society*, (October):4–7, 2009.
- N. Mungan. Role of Wettability and Interfacial Tension in Water Flooding. *Old SPE Journal*, Volume 4,, 1964. doi: 10.2118/705-PA.
- P. Oren. Mobilization of waterflood residual oil by gas injection for water-wet conditions. *SPE Formation Evaluation*, Volume 7,, 1992.
- W. Owens and D. Archer. The Effect of Rock Wettability on Oil-Water Relative Pemwability Relationships. *Volume 251*, pages 873–878, 1971.
- J. Peden and M. Husain. Visual Investigation of Multiphase Flow and Phase Interactions Within Porous Media. In *Proceedings of SPE Annual Technical Conference and Exhibition*. Society of Petroleum Engineers, Sept. 1985. doi: 10.2523/14307-MS.
- S. H. Raza, L. E. Treiber, and D. L. Archer. Wettability of Reservoir Rocks and Its Evaluation. *Prod Monthly*, 32(4):2–7, 1968.

- M. Riazi and M. Sohrabi. Oil recovery improvement using CO<sub>2</sub>-enriched water injection. In *SPE EUROPEC/EAGE Annual Conference and Exhibition*, Amsterdam, The Netherlands, 2009. Society of Petroleum Engineers.
- S. M. Rivet, L. W. Lake, and G. A. Pope. A Coreflood Investigation of Low-Salinity Enhanced Oil Recovery. *Water*, (September):19–22, 2010.
- S. G. Sayegh and D. Fisher. Enhanced Oil Recovery by CO<sub>2</sub> Flooding in Homogeneous and Heterogeneous 2D Micromodels. In *Canadian International Petroleum Conference*, Calgary, Alberta, 2008.
- L. Schramm. *Surfactants Fundamentals and Applications in the Petroleum Industry*. Cambridge University Press, Cambridge, UK, 2000. ISBN 978-0521640671.
- E. Sollier, C. Murray, P. Maoddi, and D. Di Carlo. Rapid prototyping polymers for microfluidic devices and high pressure injections. *Lab on a chip*, 11(22):3752–65, Nov. 2011. ISSN 1473-0189. doi: 10.1039/c1lc20514e.
- R. Stalker and G. Graham. Radial Core Flood Placement Tests. In *SPE International Oilfield . . .*, number May, Aberdeen, UK, 2008. doi: 10.2118/114096-MS.
- J. a. Vickers, B. M. Dressen, M. C. Weston, K. Boonsong, O. Chailapakul, D. M. Cropek, and C. S. Henry. Thermoset polyester as an alternative material for microchip electrophoresis/electrochemistry. *Electrophoresis*, 28(7):1123–1129, Apr. 2007. ISSN 01730835. doi: 10.1002/elps.200600445.
- M. Wu, F. Xiao, R. M. Johnson-Paben, S. T. Retterer, X. Yin, and K. B. Neeves. Single- and two-phase flow in microfluidic porous media analogs based on Voronoi tessellation. *Lab on a Chip*, 12(2):253, 2012. ISSN 1473-0197. doi: 10.1039/c1lc20838a.
- Y. Wu, P. J. Shuler, M. Blanco, Y. Tang, and W. A. G. III. An Experimental Study of Wetting Behavior and Surfactant EOR in Carbonates With Model Compounds. *SPE Journal*, 13(March), 2008. ISSN 1086055X. doi: 10.2118/99612-PA.
- M. Yao and J. Fang. Hydrophilic PEO-PDMS for microfluidic applications. *Journal of Micromechanics and Microengineering*, 22(2):025012, Feb. 2012. ISSN 0960-1317. doi: 10.1088/0960-1317/22/2/025012.

## APPENDIX - IMAGE-FIJI AND MATLAB SCRIPTS

### A.1 Image Processing

This ImageJ macro was written for imaging processing. The flowchart is in Figure 2.19

```
// This Macro is for automatically thresholding microscope images
// Open a image file , input the parameter and run
// By Wei Xu

// Input Parameter
number = 63;           // Number of images in this case
position = 7;           // Microscope carema position number

// Create new folders
dir = getInfo("image.directory");
for (i=1; i<position+1; i++){
    myDir = dir+"Position "+i+File.separator;
    File.makeDirectory(myDir);
}
print(dir);

// Thresholding and SaveAs
for (n=1; n<number+1; n++){
    name = getInfo("image.filename");
    if (indexOf(name, "Position")>-1){
        run("Subtract Background...", "rolling=50 light");
        run("Enhance Contrast", "saturated=0.4");
        run("8-bit");
        setAutoThreshold("Default");
        run("Threshold...");
        setAutoThreshold();
        run("Convert to Mask");
    }
    if (indexOf(name, "Position 1")>-1)
        saveAs('Tiff', dir+"Position 1"+File.separator+
                name);
    else if (indexOf(name, "Position 2")>-1)
        saveAs('Tiff', dir+"Position 2"+File.separator+
                name);
    else if (indexOf(name, "Position 3")>-1)
        saveAs('Tiff', dir+"Position 3"+File.separator+
                name);
```

```

        else if (indexOf(name, "Position 4") >-1)
            saveAs('Tiff', dir+"Position 4"+File.separator+
                    name);
        else if (indexOf(name, "Position 5") >-1)
            saveAs('Tiff', dir+"Position 5"+File.separator+
                    name);
        else if (indexOf(name, "Position 6") >-1)
            saveAs('Tiff', dir+"Position 6"+File.separator+
                    name);
        else if (indexOf(name, "Position 7") >-1)
            saveAs('Tiff', dir+"Position 7"+File.separator+
                    name);
        else if (indexOf(name, "Position 8") >-1)
            saveAs('Tiff', dir+"Position 8"+File.separator+
                    name);
        run("Open Next");
    }
    print("Thresholding Done!");

```

## A.2 Pixel Analysis

This ImageJ macro was written for imaging processing. The flowchart is in Figure 2.20

```

// One key pixel analysis by Wei Xu
// Open the first image of one position
// Select the zone, or it will be all selected

// Input stage number
stage = 9;

// Analyzing
for (s=1; s<stage+1; s++){
    run("Measure");
    run("Open Next");
}
close()

```

## A.3 Recovery Calculation

This MATLAB script was written for recovery factor calculation. The flowchart is in Figure 2.21

```
\% Saturation Analysis
```

```

\% By Wei Xu
\% Raw data should be copied from ImageJ–Fiji and edited in Excel

\% Only keep the area\% column, saved as CSV

clc; clear;
\% Set Parameter
position = 7;
stage = 9;
Sw = zeros(position ,stage);
Sw(:,1) = 1;
RF = zeros(position ,stage -2);
RF_all = zeros(1,stage -2);

\% Flooding stage:
\% 1: Water Filled
\% 2: Oil Final
\% 3-stage: Different Pore Volume (PV) injected and BT

\% Read Area\% from CSV
Data = csvread('C:\Users\heidernljb\Desktop\Data.csv');

\% Read from CSV
for p = 1 : position
    Sw(p,2) = Data((p-1)*stage+2)/Data((p-1)*stage+1);

    for s = 3 : stage
        n = (p - 1) * stage + s;
        Sw(p,s) = Data(n) / Data((p-1)*stage+1);

        if Sw(p,s) > 1
            Sw(p,s) = 1;
        end

        RF(p,s-2) = (Sw(p,s) - Sw(p,2))/(1 - Sw(p,2));

        if RF(p,s-2) < 0
            RF(p,s-2) = 0;
        end
        if RF(p,s-2) > 1
            RF(p,s-2) = 1;
        end
    end
end
Sw
So = 1-Sw
RF

```

```
RF_all = mean(RF,1)
```